

Copyright

by

Abhinav Sultania

2010

The Thesis committee for Abhinav Sultania
certifies that this is the approved version of the following thesis:

**Reliability Analysis of a Spar Buoy-Supported
Floating Offshore Wind Turbine**

**APPROVED BY
SUPERVISING COMMITTEE:**

Supervisor:

Lance Manuel

Loukas F. Kallivokas

**Reliability Analysis of a Spar Buoy-Supported
Floating Offshore Wind Turbine**

by

Abhinav Sultania, B.Tech.

Thesis

Presented to the Faculty of the Graduate School
of the University of Texas at Austin
in Partial Fulfillment
of the Requirements
for the Degree of

Master of Science in Engineering

The University of Texas at Austin

August 2010

Dedicated to my parents, my brother
and my sister

Acknowledgements

I give my sincere thanks to my advisor, Dr. Lance Manuel, for providing me with the basis of knowledge necessary to undertake this project, and for the guidance necessary to finish it. His significant contribution of time and knowledge to this project is gratefully acknowledged.

I would also like to thank Ms. Erica Bush for helping me get started on this research. I thank member of my thesis committee, Dr. Loukas F. Kallivokas for serving on my committee and giving thoughtful advice. I thank Dr. Jason Jonkman of National Renewable Energy Laboratory for providing the simulation model of an offshore wind turbine, and for his assistance with the wind turbine simulation model and with the environmental data used in this study.

I want to acknowledge the financial support for this project from the National Science Foundation by way of two grants—Award Nos. CMMI-0049128 (CAREER) and CMMI-0727989. I also want to acknowledge the financial support for this project from Sandia National Laboratories by way of Contract No. 743358. Besides, I would like to acknowledge the financial support provided by the Department of Civil, Architectural, and Environmental Engineering during the two years of my masters program.

I want to thank my parents, my brother, my sister, and my friends for their unconditional love and support. Last but not the least, want to express gratitude to God, for giving me patience and energy in all my endeavors.

Abstract

Reliability Analysis of a Spar Buoy-Supported Floating Offshore Wind Turbine

by

Abhinav Sultania, M.S.E.

The University of Texas at Austin, 2010

SUPERVISOR: Lance Manuel

While wind energy has witnessed faster growth than any other renewable energy source in recent years, two issues—the decreasing availability of large land expanses for new wind farms and transmission difficulties arising from siting wind farms in remote regions far from load centers—have slowed down this growth considerably. Siting wind turbines offshore places the generating capacity closer to population and load centers; thus, reducing grid congestion. Also, at offshore sites, one can expect higher wind speeds, decreased turbulence, and reduced noise and visual impact constraints. Offshore wind turbines that have been built thus far have had foundations (such as monopiles or jacket structures) that have extended to the seabed. Such offshore wind turbines have thus been confined to shallow waters closer to the shore. Sites farther offshore provide better wind resources (i.e., less turbulence and smoother, stronger winds) while also reducing visual impact, noise, etc. However, deeper waters encountered at such sites make bottom-supported turbines less economical. Wind turbines mounted atop floating platforms are, thus, being considered for deeper water offshore sites. Various floating platform concepts are under consideration; the chief differences among them arise from the way they provide stability to counter the large mass of the rotor-nacelle assembly located high above the mean water level. Of these alternative concepts, the spar buoy platform is a deep draft structure with a low center of gravity, below the center of buoyancy.

Reliability analysis of a spar buoy-supported floating offshore 5MW wind turbine based on stochastic simulation is the subject of this study. Environmental data from a selected deepwater reference site are employed in the numerical studies. Using time-domain simulations, the dynamic behavior of the coupled platform-turbine system is studied; statistics of tower and rotor loads as well as platform motions are estimated and critical combinations of wind speed and wave height identified. Long-term loads associated with a 50-year return period are estimated using statistical extrapolation based on loads derived from the simulations. Inverse reliability procedures that seek appropriate fractile levels for the underlying random variables consistent with the target load return period are employed; these include use of: (i) the 2D Inverse First-Order Reliability Method (FORM) where extreme loads, conditional on wind speed and wave height random variables, are selected at their median level; and (ii) the 3D Inverse FORM where variability in the environmental and load random variables is fully represented.

Table of Contents

ACKNOWLEDGEMENTS	v
ABSTRACT	vi
LIST OF TABLES	x
LIST OF FIGURES	xi
CHAPTER 1: INTRODUCTION	1
1.1 Background	1
1.2 Research Motivation	2
1.3 Scope.....	3
1.4 Thesis Organization	4
CHAPTER 2: MODEL DEVELOPMENT FOR SIMULATION STUDIES WITH THE WIND TURBINE AND FLOATING PLATFORM	5
2.1 Introduction.....	5
2.2 Examples of Alternative Floating Wind Turbine Concepts.....	5
2.3 Review of Floating Wind Turbine Model Development	7
2.4 The Spar Buoy Platform Concept for Offshore Wind Turbines	9
2.5 Simulation Model.....	11
2.5.1 The Baseline Wind Turbine Model.....	11
2.5.2 The Spar Buoy Platform and Mooring Lines Model	13
2.5.3 Inflow Turbulence and Aerodynamic Forces on the Blades.....	13
2.5.4 Hydrodynamic Forces on the Floating Platform.....	14
2.5.5 Fast Simulation	14

2.6 System Transfer Functions	15
2.7 The Reference Site	22
2.8 Summary	25
CHAPTER 3: EXTREME LOADS ON A SPAR BUOY-SUPPORTED FLOATING OFFSHORE WIND TURBINE	26
3.1 Introduction.....	26
3.2 Simulation Model and Probabilistic Description of the Environment.....	26
3.2.1 The Baseline Wind Turbine Model.....	26
3.2.2 The Spar Buoy Platform and Mooring Lines Model	27
3.2.3 Inflow Turbulence and Aerodynamic Forces on the Blades.....	28
3.2.4 Hydrodynamic Forces on the Floating Platform.....	28
3.2.5 The Reference Site and Environmental Conditions.....	29
3.3 Stochastic Response Simulations.....	31
3.4 Numerical Studies	31
3.4.1 Time Series	31
3.4.2 Response Statistics.....	33
3.4.3 Short-Term Distributions for Turbine Loads and Platform Motions...	40
3.4.4 Power Spectra	41
3.4.5 Interpretation of Short-Term Response Statistics	45

3.5 Summary	50
CHAPTER 4: LONG-TERM LOADS FOR A SPAR BUOY-SUPPORTED FLOATING OFFSHORE WIND TURBINE	51
4.1 Introduction.....	51
4.2 Probabilistic Distributions for the Environmental Random Variables	54
4.3 Short-Term Response Extremes	55
4.4 Statistical Extrapolation of Response	59
4.5 Summary	65
CHAPTER 5: CONCLUSIONS	66
5.1 Overview of the Research Study.....	66
5.2 Conclusions.....	66
5.3 Concluding Comments and Suggestions for Future Research.....	67
REFERENCES	69
VITA	72

List of Tables

Table 2.1: Structural properties of the wind turbine tower.	12
Table 2.2: A description of the floating wind turbine system’s natural modes of vibration and corresponding natural frequencies.	24
Table 3.1: Sea states selected for the turbine response stochastic simulations.	31
Table 3.2: Ensemble statistics of the tower base fore-aft bending moment from fifteen ten-minute simulations for four selected critical sea states.	35
Table 3.3: Ensemble statistics of the blade root out-of-plane bending moment from fifteen ten-minute simulations for four selected critical sea states.	37
Table 3.4: Ensemble statistics of the platform surge from fifteen ten-minute simulations for the selected critical sea states.	39
Table 4.1: Extrapolated response (l_{p3}), largest simulated extreme (SimMax), and median extreme response ($l_{0.5}$) based on N simulations for a few critical sea states.	61
Table 4.2: Estimated 50-year response values for (a) fore-aft tower base bending moment, (b) out-of-plane blade root bending moment, and (c) platform surge motion using 3-D Inverse FORM.	62

List of Figures

Figure 2.1: Alternate Floating Wind Turbine Concepts (from Jonkman, 2007).....	6
Figure 2.2: The NREL 5 MW wind turbine supported on the OC3-Hywind spar platform.	10
Figure 2.3: Schematic diagram of the spar buoy-supported floating offshore wind turbine.....	12
Figure 2.4: Computational Framework for the FAST Turbine Response Simulations.....	15
Figure 2.5: Restoring characteristics for a spar platform achieved by way of ballasting and water plane area (adapted from Wayman et al, 2006).....	18
Figure 2.6: Transfer functions, T_{ii} , for the 6 rigid-body modes of the turbine system (surge, sway, heave, roll, pitch, and yaw) corresponding to the response of the i^{th} DOF due to unit harmonic load applied in the same direction (i.e., in the direction of the i^{th} DOF).	22
Figure 2.7: Transfer functions, T_{ij} , corresponding to the response of the i^{th} DOF due to unit harmonic load applied in the direction of the j^{th} DOF. Shown are transfer functions for the coupling action between the surge and pitch modes (T_{15} , T_{51}) and between the sway and roll modes (T_{24} , T_{42}).	23
Figure 2.8: The reference site chosen for the location of the offshore wind turbine in this study.....	24
Figure 3.1: Joint distributions (based on data from the former Stevenson Weather Station site) showing (a) hub-height ten-minute mean wind speed versus significant wave height; and (b) significant wave height versus peak spectral period.....	30
Figure 3.2: Representative sea states selected for analysis.	30
Figure 3.3: Time series of the hub-height longitudinal wind speed, the sea surface elevation, the platform pitch and surge motions, tower base fore-aft bending moment, and blade root out-of-plane bending moment for the floating offshore wind turbine for $V = 14.69$ m/s, $H_s = 8.5$ m, $T_p = 16.19$ s.....	32
Figure 3.4: Ensemble tower base fore-aft bending moment statistics from fifteen ten minutes simulations for all eighteen sea states.	34
Figure 3.5: Ensemble blade root out-of-plane bending moment statistics from fifteen ten minutes simulations for all eighteen sea states.....	36
Figure 3.6: Ensemble platform surge statistics from fifteen ten minutes simulations for all eighteen sea states.	38
Figure 3.7: Cumulative distribution functions of the hub-height longitudinal wind speed, the sea surface elevation, and various turbine response variables based on fifteen ten-minute simulated time series with input environmental variables, $V = 14.69$ m/s, $H_s = 8.5$ m, and $T_p = 16.19$ s.....	40

Figure 3.8: Power spectral density functions of the hub-height longitudinal wind speed, the sea surface elevation, and various turbine response variables for a single ten-minute simulated time series with input environmental variables, $V = 14.69$ m/s, $H_s = 8.5$ m, and $T_p = 16.19$ s. 42

Figure 3.9: Variation in power spectral density functions of the hub-height longitudinal wind speed, the sea surface elevation, and various turbine response variables as the significant wave height is changed for a fixed ten-minute average longitudinal hub-height mean wind speed of 11.89 m/s (blue: $H_s = 0.5$ m; green: $H_s = 3.5$ m; red: $H_s = 6.5$ m). 43

Figure 3.10: Variation in power spectral density functions of the hub-height longitudinal wind speed, the sea surface elevation, and various turbine response variables as the ten-minute average hub-height longitudinal wind speed is changed for a fixed significant wave height of 6.5 m (blue: $V = 6.30$ m/s; green: $V = 11.89$ m/s; red: $V = 21.69$ m/s). 44

Figure 3.11: Representative time series and power spectral density functions of the hub-height longitudinal wind speed, the sea surface elevation, the fore-aft tower base bending moment, the out-of-plane blade root bending moment, the platform surge motion, and the platform pitch motion for the floating offshore wind turbine for still water (no waves). Plots (a) and (b) are for a steady mean wind speed of $V = 9.1$ m/s while Plots (c) and (d) are for a steady mean wind speed of $V = 14.7$ m/s. 47

Figure 3.12: Representative time series and power spectral density functions of the hub-height longitudinal wind speed, the sea surface elevation, the fore-aft tower base bending moment, the out-of-plane blade root bending moment, the platform surge motion, and the platform pitch motion for the floating offshore wind turbine for steady wind (no turbulence). Plots (a) and (b) are for $V = 9.1$ m/s, $H_s = 7.5$ m, $T_p = 16.19$ s while Plots (c) and (d) are for $V = 14.7$ m/s, $H_s = 8.5$ m, $T_p = 16.19$ s. 48

Figure 3.13: Representative time series and power spectral density functions of the hub-height longitudinal wind speed, the sea surface elevation, the fore-aft tower base bending moment, the out-of-plane blade root bending moment, the platform surge motion, and the platform pitch motion for the floating offshore wind turbine for still water (no waves). Plots (a) and (b) are for a stochastic wind field with $V = 9.1$ m/s while Plots (c) and (d) are for a stochastic wind field with $V = 14.7$ m/s. 49

Figure 4.1: Sea states selected for the turbine response stochastic simulations indicated by dots shown along with the 2-D environmental contour for a 50-year return period. 56

Figure 4.2: Response exceedance fractiles, p_3 , for candidate sea state evaluated. Also shown in order moving inwards are contours of 0.5, 1e-1, 1e-2, 1e-3, 1e-4, 1e-5, and 1e-6 exceedance fractiles. 57

Figure 4.3: Median ten-minute extreme response surfaces based on 25 simulations for: (a) fore-aft tower base bending moment; (b) out-of-plane blade root bending moment; and (c) platform surge. 58

Figure 4.4: Contours of the ratio of the 84th percentile non-exceedance response extreme to the median response extreme based on 25 simulations for: (a) fore-aft tower base bending moment; (b) out-of-plane blade root bending moment; and (c) platform surge. Also shown is the 50-year return period environmental contour. 60

Figure 4.5: Two-parameter Weibull distribution fits to the largest 50% of simulated ten-minute response extremes in critical sea states for: (a) fore-aft tower base bending moment; (b) out-of-plane blade root bending moment; and (c) platform surge..... 63

Figure 4.6: Time series for a single simulation showing hub-height longitudinal wind speed, sea surface elevation, blade pitch, and fore-aft tower base bending moment for the sea state with $V = 21.7$ m/s and $H_s = 7.5$ m and where the largest fore-aft tower base bending moment (177.1 MN-m) was found..... 64

Figure 4.7: Time series for a single simulation showing hub-height longitudinal wind speed, sea surface elevation, blade pitch, and out-of-plane blade root bending moment for the sea state with $V = 16.1$ m/s and $H_s = 6.5$ m and where the largest out-of-plane blade root bending moment (15.0 MN-m) was found..... 64

Chapter 1: Introduction

1.1 Background

In the last two decades, there has been significant growth in wind energy development and wind turbine technologies both onshore as well as offshore. However, in recent years, this rate of growth has slowed considerably due to reduced availability of large land expanses for new wind farms and transmission difficulties arising from siting wind farms in remote regions far from load centers. Siting wind turbines offshore places the generating capacity closer to population and load centers; thus, reducing grid congestion. Also, offshore, one can expect higher wind speeds, decreased turbulence, and reduced noise and visual impact constraints. For continued development of wind energy, offshore locations provide viable alternatives or complements to developed and planned onshore sites. The potential for offshore wind energy development is great in many parts of the world. In the U.S. Department of Energy's planning, a stated goal is for wind energy to provide 20% of the nation's energy needs by 2030; of the 305 GW of energy required from wind then, offshore wind is expected to provide 54 GW (U.S. Department of Energy, 2008). Similarly, a recent study from the European Wind Energy Association predicts that Europe could get almost half its total electricity from deepwater offshore wind by the middle of the century (The European Wind Energy Association, 2009).

Offshore wind turbines that are in place thus far have foundations (such as monopiles or jacket structures) that extend down to the seabed. Such offshore wind turbines have, therefore, been confined to shallow waters closer to the shore. Sites farther offshore provide better wind resources (i.e., less turbulence and smoother, stronger winds) while also reducing visual impact, noise, etc. However, the deeper waters encountered at such sites make bottom-supported turbines less economical. Wind turbines mounted atop floating platforms are, thus, being considered for deeper water offshore sites. Various floating platform concepts are under consideration; the chief differences among them are in the way by which they provide stability to counter the large mass of the rotor-nacelle assembly located high above the mean water level. Of the various alternative deepwater offshore wind concepts, the spar buoy platform is a deep draft structure that achieves stability by means of a very low center of gravity that is below the center of buoyancy. By virtue of its slender and deep draft, the spar buoy can easily provide necessary gravity-based stability; wave loads, too, are moderate on these platforms. Indeed, several studies are underway to investigate their feasibility with regard to performance, economics, and construction. Recently, in Norway, Statoil began a two-year field testing campaign of the first proof of concept (PoC) 2.3 MW Siemens floating wind turbine mounted on a spar platform in 700 feet of water. The reliability analysis of a spar buoy-supported floating offshore 5MW wind turbine based on stochastic simulation is the subject of this study. Using environmental data for a reference site, the dynamic behavior and long-

term loads and motions of the coupled platform-turbine system are studied.

1.2 Research Motivation

The International Electrotechnical Commission has issued design guidelines for wind turbines for both onshore (IEC 61400-1) and offshore (IEC 61400-3) sites (International Electrotechnical Commission (2005, 2009)). These standards are based on load-and-resistance-factor-design (LRFD) principles, which require establishing that factored nominal or characteristic loads are smaller than factored resistances. Various ultimate and fatigue limit states are addressed in this manner in the various stipulated design load cases (DLCs).

Design load case (DLC) 1.1 in IEC 61400-3 applies during operating (power-production) conditions for an offshore wind turbine; it requires computation of turbine loads for wind conditions (i.e., specified mean wind field and turbulence conditions) associated with the Normal Turbulence Model (NTM) and waves described by Normal Sea State (NSS) conditions. DLC 1.1 applies to an ultimate limit state associated with extreme loads acting on the rotor-nacelle assembly (RNA) as well as the support structure. The LRFD checking equation requires estimation of a nominal load associated with a 50-year return period. In order to establish such 50-year loads, load time series need to be simulated. Then, extreme load statistics from a limited number of such simulations need to be used along with statistical extrapolation to derive the desired 50-year load. In principle, load probability distributions need to be derived for all possible wind speed and wave height combinations and then they need to appropriately be accounted for based on the likelihood of each combination; such distributions, conditional on wind-wave combinations, are termed “short-term” distributions. The weighted short-term distributions when integrated over all environmental conditions yield the “long-term” distributions which are then employed to establish the 50-year load. Short-term load distributions are derived in this study using time-domain turbine response simulations of ten-minute duration. By running multiple ten-minute simulations for each wind-wave combination, the short-term distributions are established using the load extremes.

Several methods for statistical loads extrapolation are in use. Direct integration is the usual method for extrapolation, in which one estimates the turbine load, l_T , associated with a target probability of exceedance, P_T , or, equivalently, with a target return period of T years, as follows:

$$P_T = P(L > l_T) = \int_{\mathbf{X}} P(L > l_T | \mathbf{X} = \mathbf{x}) f_{\mathbf{X}}(\mathbf{x}) d\mathbf{x} \quad (2.1)$$

where $f_{\mathbf{X}}(\mathbf{x})$ represents the joint probability density function of the environmental random variable vector, \mathbf{X} . The random variable, L represents the load of interest; for offshore wind turbines, the environmental

random variable vector, \mathbf{X} , may, at a minimum, include the ten-minute hub-height longitudinal wind speed, V , and the significant wave height, H_s , i.e., $\mathbf{X} = \{V, H_s\}$. For different trial values of the load, l_T , Eq. (1.1) enables one to compute the long-term probability of its exceedance by exhaustively integrating the short-term probability of exceedance conditional on \mathbf{X} , i.e., $P(L > l_T | \mathbf{X} = \mathbf{x})$, with the relative likelihood of different choices for \mathbf{X} . The load level at which the computed long-term probability integral matches the target probability, P_T , is the desired T -year return period load, l_T . The direct integration method, while exact, is computationally expensive as one is required to integrate over the entire domain of all the environmental random variables. In Eq. (1.1), $f_{\mathbf{X}}(\mathbf{x})$, describes the joint probability density function of the environmental random variables; for instance, for offshore wind turbines, one can represent this as the product of a marginal density function, $f_V(v)$ and a conditional density function, $f_{H_s|V}(h|v)$. Also, in Eq. (1.1), $P(L > l_T | \mathbf{X} = \mathbf{x})$ needs to be established by turbine response simulations for each choice of \mathbf{X} or, effectively, of V and H_s . Note that the formulation of Eq. (1.1) allows expansion of the vector, \mathbf{X} , to include other variables than V and H_s but this would, in general, require more detailed information on the environmental random variables in order to establish, $f_{\mathbf{X}}(\mathbf{x})$.

One generally needs statistics on turbine load extremes in order to establish the conditional probability distribution function, $P(L > l_T | \mathbf{X} = \mathbf{x})$ in Eq. (1.1). These extreme loads for a given sea state, defined by \mathbf{X} , can be obtained from simulations, typically of ten-minute duration, in different ways. From a single ten-minute simulated load time series, extremes can be described by (i) the single largest ten-minute maximum (i.e., using global maxima) (ii) local maxima occurring in non-overlapping blocks assuming statistical independence between these maxima (i.e., using block maxima); or (iii) peaks that occur above a selected threshold level—i.e., using the peak-over-threshold or POT method (Ragan, 2007). For offshore wind turbines, the integration implied by Eq. (1.2) suggests significant computational effort since the environmental random variable vector and, hence, the domain of integration is at least two-dimensional. Hence, other more efficient methods of statistical load extrapolation such as the use of Inverse First-Order Reliability Method (Inverse FORM) have been proposed as an alternative to direct integration. In these methods, for the “target” probability of load exceedance level of interest, one identifies “controlling” environmental conditions, \mathbf{X} , that cause large appropriately specified “short-term” load extreme fractiles. As note, such methods, albeit approximate, are more efficient than direct integration and they provide insight on critical environmental conditions that cause loads that influence design.

1.3 Scope

This study is focused on understanding the dynamic characteristics and long-term loads on an offshore turbine supported by a spar floating platform. We only address the ultimate limit state associated

with a single design load case (i.e., DLC 1.1). To understand extreme turbine loads and platform motions, we study a range of sea states and environmental conditions. These environmental conditions are for a reference site chosen for this study. This site and the selected offshore wind turbine and platform are employed in reliability analyses described here.

1.4 Thesis Organization

Chapter 2 describes offshore floating wind turbine concepts in general; the selected spar buoy support platform and offshore wind turbine for this study; model development for the turbine, platform, and mooring lines; and the reference site.

In Chapter 3, we discuss “short-term” response statistics based on stochastic simulation for a range of different environmental wind and wave conditions in order to identify critical environmental conditions for subsequent reliability analyses. Time series, power spectra, and statistics of turbine loads and platform motions are studied.

In Chapter 4, we focus on estimation of long-term blade and tower loads and long-term platform motions using inverse reliability procedures.

Chapter 5 summarizes the objectives, results, and conclusions of this research study.

Chapter 2: Model Development for Simulation Studies with the Wind Turbine and Floating Platform

2.1 Introduction

The offshore oil and gas industry has successfully demonstrated the long-term survivability of floating platforms over the last several decades. For wind energy applications at deepwater offshore sites, a challenge is that the floating platform must provide sufficient buoyancy to support the weight of the turbine and to restrain pitch, roll, and heave motions to acceptable limits.

In a coupled wind turbine and floating support platform system, stability is achieved through one of three general mechanisms: a weighted water-plane area that resists overturning moment; ballasting that creates vertical separation of the system's center of gravity below its center of buoyancy; or the use of a mooring system and tanks where mooring-line tension from excess buoyancy in the tank provides stability. These different mechanisms also serve as a means for classifying the different floating wind turbine concepts (Butterfield et al., 2007).

The behavior of a floating wind turbine is complex one. Different modes of motion can interact with each other to produce interesting effects. Due to the incident wind, the spinning inertia of the rotor leads to excitation of blade mode along with the gravitational pull of the blade (i.e., at the 1P or 1 per rev loading frequency and multiples of it). On other hand, tower response can be excited by low-frequency wave energy and resulting hydrodynamic loading that leads to pitching of the turbine system coupled with surge motion. Furthermore, as for any pitch-regulated wind turbine, additional variability in loads is introduced above the turbine's rated wind speed by the need for the controller to bring about pitching of the turbine blades to alleviate structure loads. Also, if both wind and waves are assumed aligned along the x axis (longitudinal direction), a small roll moment is exerted on the platform by the generator torque. This roll moment of the floater results in the nacelle moving off axis; this movement produces a moment arm along the y axis (lateral direction) that, in combination with the rotor thrust, produces a yaw moment. These various motion characteristics suggest the need for modeling of various coupling mechanisms between the structures; such dynamic coupling is crucial in the formulation and solution of the system equations of motion.

2.2 Examples of Alternative Floating Wind Turbine Concepts

Floating offshore wind turbines are generally considered for operation only in deep water. They will likely be the only economical solution for wind energy development at most deepwater sites. Only a very few floating wind turbines are being studied in research and development projects around the world. Essentially all of the efforts are based on the floating oil rig technology. As mentioned before,

classification of floating offshore wind turbine concepts depends on varying moorings, tanks, and ballast options. In general, this classification is primarily related to the means by which stability is achieved. The National Renewable Energy Laboratory (NREL) has classified these oil rig-based concepts into three types as shown in Figure 2.1. These three classifications are as follows:

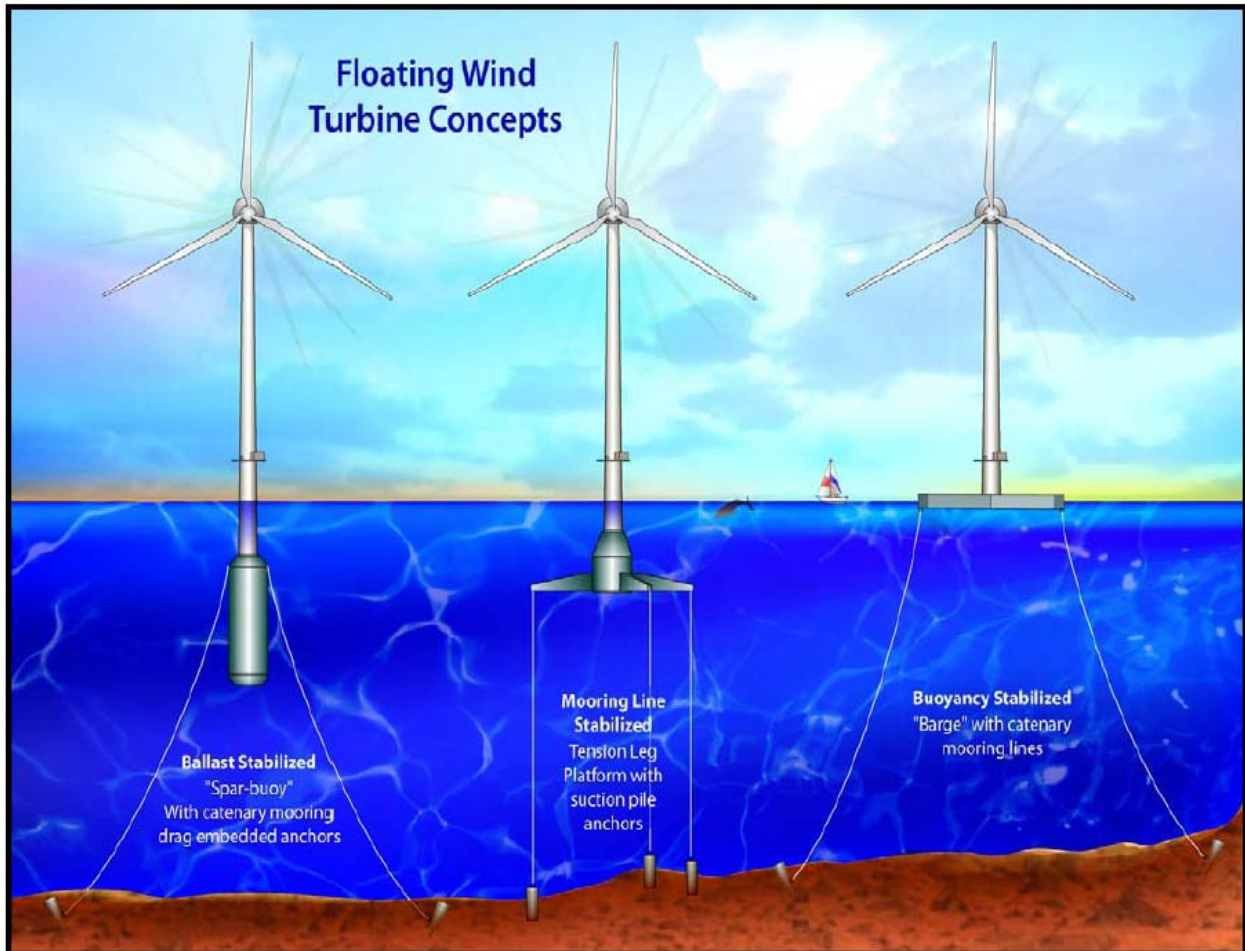


Figure 2.1: Alternate Floating Wind Turbine Concepts (from Jonkman, 2007).

1) Ballast-stabilized: These are platforms that achieve stability by using ballast weights hung below a central buoyancy tank (which creates a righting moment and high inertial resistance to pitch and roll) and usually have a sufficiently deep draft to offset heave motion. Spar buoys such as the one shown in Figure 2.1 apply this strategy to achieve stability.

2) **Mooring lines-stabilized:** These are platforms that achieve stability through the use of mooring line tension. The tension leg platform (TLP), such as the one shown in Figure 2.1, relies on mooring line tension for righting stability.

3) **Buoyancy-stabilized:** These are platforms that achieve stability through the use of distributed buoyancy, taking advantage of weighted water plane area for righting moment. This is the principle used in a barge shown in Figure 2.1.

An offshore wind turbine does not have the same design drivers as is the case for oil rigs. Oil rig technology requires the lifting of dense materials including oil from the sea floor; hence, oil rigs experience large vertical loading along with some lateral loading due to waves, currents, and wind. On the other hand, wind turbines experience large lateral wind thrust loads and gyroscopic loads from the rotor. These contrasting loadings make the design of floating platforms for the two technologies (oil rigs and wind turbines) quite different. New configurations for foundations, towers, and platforms are needed for use with floating wind turbines to make them commercially viable. Offshore wind turbines need to be able to withstand extreme wave (hydrodynamic) loads as well as large wind (aeroelastic) loading and associated motions of the tower and floating platform.

2.3 Review of Floating Wind Turbine Model Development

Very few studies have assessed the preliminary design and analysis of spar buoy-supported floating offshore wind turbines although some studies have been carried out for other types of floating wind turbines. These studies have generally employed frequency-domain analysis to investigate system response. Linear frequency-domain hydrodynamics has been assumed in deriving Response Amplitude Operators (RAOs) for the six rigid body modes of motion of the support platform for various wind turbines. Lee (2005) used this procedure to analyze a TLP and a taut-leg spar buoy design for a 1.5 MW wind turbine. Wayman et al. (2006) also used this same procedure to analyze a TLP and a shallow-drafted barge design for a 5 MW wind turbine. To analyze the support platform response together with the influence of the wind turbine placed on top of it, these studies augmented the platform's body mass matrix with the mass properties of the turbine; similarly, platform hydrodynamic damping and restoring matrices were augmented with damping and restoring contributions from rotor aerodynamic and gyroscopic effects. The effect of the platform mooring system in these studies was also assumed to be linear; linearized restoring matrices of the mooring system were derived about a mean offset displacement of the support platform caused by the aerodynamic thrust on the rotor. The entire system was designed in such a manner that the natural frequencies of the floating platform were outside of the range of dominant

wave energy, ensuring low dynamic response in the system. A limitation of these frequency-domain linear analyses is that they do not capture the nonlinear dynamic response of the system.

In order to incorporate the nonlinear dynamics for a TLP-supported floating offshore wind turbine, time-domain studies were performed by Withee (2004). To describe the hydrodynamic loading, that study used Morison's equation which ignores many effects that are important in the analysis of most floating platform configurations such as the influence of platform size on diffraction, wave radiation damping and free-surface memory, and the effect of added mass-induced coupling between modes of motion.

Studies by Nielsen et al (2006) and Skaare et al (2007) that employed a coupled aeroelastic, hydrodynamic, and mooring program to design a deep-drafted spar buoy platform (called "Hywind") to support a 5 MW wind turbine and to develop an associated control system showed that the platform motions had little effect on the power captured and on the rotor loads. Captured power was found to be dependent on the input wind and aerodynamics of the rotor. Platform motions had a significant effect on tower and nacelle loads, which are dominated by inertia; the suggestion was that tower would need to be strengthened if platform motions could not be reduced. This study also verified estimations of the response from the computer program simulations by comparisons with response measurements from a scaled-down model in a wave tank experiment.

The IEC 61400-3 design standard (International Electrotechnical Commission, 2009) provides design requirements for offshore wind turbines and requires that an integrated loads analysis be performed. Such integrated loads analyses are carried out using comprehensive time-domain simulation tools that employ sophisticated models of both turbulent and deterministic wind inflow; aerodynamic, gravitational, and inertial loading of the rotor, nacelle, and tower; and mechanical actuation and electrical response of the generator and control and protection systems. For offshore wind turbines, additional models are also needed for the hydrodynamic loading in regular and irregular seas, the dynamic coupling between the support platform and the wind turbine, and the dynamic characterization of mooring systems for compliant floating platforms. Jonkman and Sclavounas (2006) and Jonkman and Musial (2007) described the development and verification of a comprehensive simulation tool that can model the fully coupled aero-hydro-servo-elastic response of offshore floating wind turbines. Their offshore floating wind turbine response simulator was developed with sufficient rigor so as to overcome the limitations of earlier time- and frequency-domain studies; it possessed the features required to perform an integrated loads analysis for a variety of wind turbine, support platform, and mooring system configurations.

Recently a study was conducted by Matha et al. (2009) on the analysis of a 5 MW wind turbine supported on a tension leg platform (TLP) using the fully coupled time-domain aero-hydro-servo-elastic design code developed by Jonkman and Buhl (2005). A comparative analysis of three alternative floating

platform concepts for offshore wind turbines was also conducted that examined turbine load statistics in order to understand fundamental design trade-offs and differences between the three concepts.

2.4 The Spar Buoy Platform Concept for Offshore Wind Turbines

In the Offshore Code Comparison Collaboration (OC3) Phase IV study, a floating offshore wind turbine based on the spar-buoy concept developed by Statoil of Norway was analyzed. This spar concept was selected because of the simplicity of its design, ease of modeling, and expected quick commercialization. The OC3 spar buoy was only based on Statoil's "Hywind" spar; actual specifications employed are somewhat different from Statoil's original design. Data provided by Statoil on their platform and mooring system were modified so that the platform design was appropriate for supporting the NREL 5 MW baseline turbine, which in turn has properties that are different from that of the turbine used by Statoil in the development of their Hywind system. This new system is referred to as the "OC3-Hywind" system to distinguish it from Statoil's original "Hywind" system. The OC3-Hywind system features a deeply drafted, slender spar buoy with catenary mooring lines as illustrated in Figure 2.2.

The combined wind turbine and floating platform system is assumed to undergo the standard rigid body modes of motion that are typically considered in any wave-body interaction study. Modes 1 to 3 represent translational modes of surge, sway and heave motion and they describe translation along the x , y , and z axes, respectively. Similarly modes 4 to 6 represent rotational modes of roll, pitch, and heave motion and they describe rotation about the x , y , and z axes, respectively. To describe the platform and wind turbine, a coordinate system is defined whose origin in the x - y coordinates is defined at the floating platform's center; also, the $z = 0$ plane is defined to coincide with the still water level (SWL) as shown in Figure 2.2.

The modeling of wave action on the spar platform accounts for contributions from linear hydrostatics, linear excitation from incident waves, linear radiation from outgoing waves (generated by the platform motion), and other nonlinear effects. The hydrodynamic loads due to excitation from incident waves and radiation from outgoing waves due to platform motion depends on whether flow separation occurs or not. For the spar buoy platform, flow separation is expected to occur only during the most extreme wave conditions and, then, only along the upper portions of the platform. As such, for the hydrodynamic load analysis, linear potential flow theory is employed. The computer program, WAMIT (Lee and Newman, 2006) is used to solve the linearized potential flow hydrodynamic radiation and diffraction problems resulting from the interaction of surface waves with offshore platforms; it employs a three-dimensional numerical panel procedure in the frequency domain. Solution of the radiation problem considers oscillation of the platform in its various modes of motion (that can radiate outgoing waves); this yields oscillation frequency-dependent hydrodynamic added-mass and damping matrices, **A** and **B**,

respectively. Solution of the diffraction problem, which considers the hydrodynamic loads on the platform associated with excitation from incident waves, yields the wave frequency- and direction-dependent hydrodynamic wave-excitation vector, \mathbf{X} .

In order to obtain appropriate levels of hydrodynamic damping in severe sea conditions, the linear potential flow theory solution needs to be augmented with a nonlinear viscous drag term arising from the relative velocity term in Morison's equation. Also, during the OC3 study, it was suggested that the linear radiation damping and the nonlinear viscous drag did not capture all of the hydrodynamic damping in the motions of Statoil's "Hywind" platform. Hence, it was recommended that the above described hydrodynamics models for the OC3-Hywind system is augmented with additional linear damping.

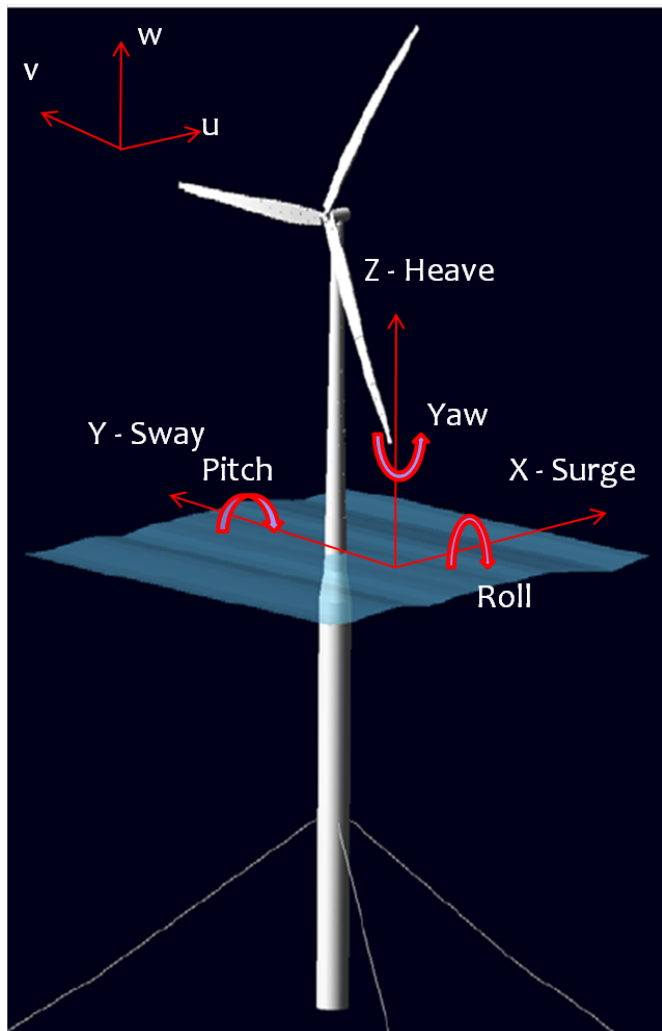


Figure 2.2: The NREL 5 MW wind turbine supported on the OC3-Hywind spar platform.

2.5 Simulation Model

All the wind turbine response simulations in this study were run using the program, FAST (Fatigue, Aerodynamics, Structures, and Turbulence), developed at the National Renewable Energy Laboratory (Jonkman and Buhl, 2005). In addition, TurbSim (Jonkman and Buhl, 2007) was employed in conjunction with FAST as the wind (inflow) turbulence simulator. Details regarding the selected wind turbine model, the support platform, and the mooring lines as well as the wind turbine response, aerodynamic loads, and hydrodynamic loads are provided in the following sections.

2.5.1 The Baseline Wind Turbine Model

The NREL 5 MW baseline wind turbine model (Jonkman et al, 2009), developed to represent a typical utility-scale multi-megawatt wind turbine for offshore applications, is considered in the present study. The turbine model is a conventional three-bladed variable-speed, collective pitch-controlled upwind machine. It was developed to support concept studies. Required structural properties and dimensions for the model were adapted from generic design information available in published documents of various turbine manufacturers, with greater emphasis on the REpower 5M machine. The selected turbine model is suitable for deployment in deep waters; it has a 126 m rotor diameter, a maximum rotor speed of 12.1 rpm, and a rated wind speed of 11.4 m/s. The turbine has a hub located 90 meters above the top of the support platform. The tower is modeled as a cantilever; its fixed base is coincident with the top of the supporting spar buoy platform. The tower base is at an elevation of 10 m above the SWL (still water level) where the tower's diameter is 6.5 m, which also matches the diameter of the top of the spar buoy platform. The cylindrical tower's base thickness is 0.027 m; the tower tapers linearly towards the top where its diameter reduces to 3.87 m and its thickness to 0.019 m. The resulting integrated tower mass is 249,718 kg with a center of mass (C.M.) located 43.4 m above the SWL. A damping ratio 1% of critical is specified for all the vibrational modes of the tower. Figure 2.3 shows a schematic diagram of the wind turbine and the supporting spar buoy platform.

Table 2.1 summarizes various structural properties of the turbine tower. The entries in the first column with designation, "Elevation w.r.t. SWL," indicate vertical locations along the tower centerline relative to the SWL. The distributed tower section mass per unit length values are documented under the column heading, "Mass Distribution." The fore-aft and side-to-side tower section flexural rigidity and moment of inertia values, "Flexural Rigidity, EI ," and "Moment of Inertia," are given about the principal structural axes of the tower cross section. "Torsional Rigidity, GJ " represents the value of the tower torsion rigidity. Tower extensional rigidity values are presented under the column, "Axial Rigidity, EA ."

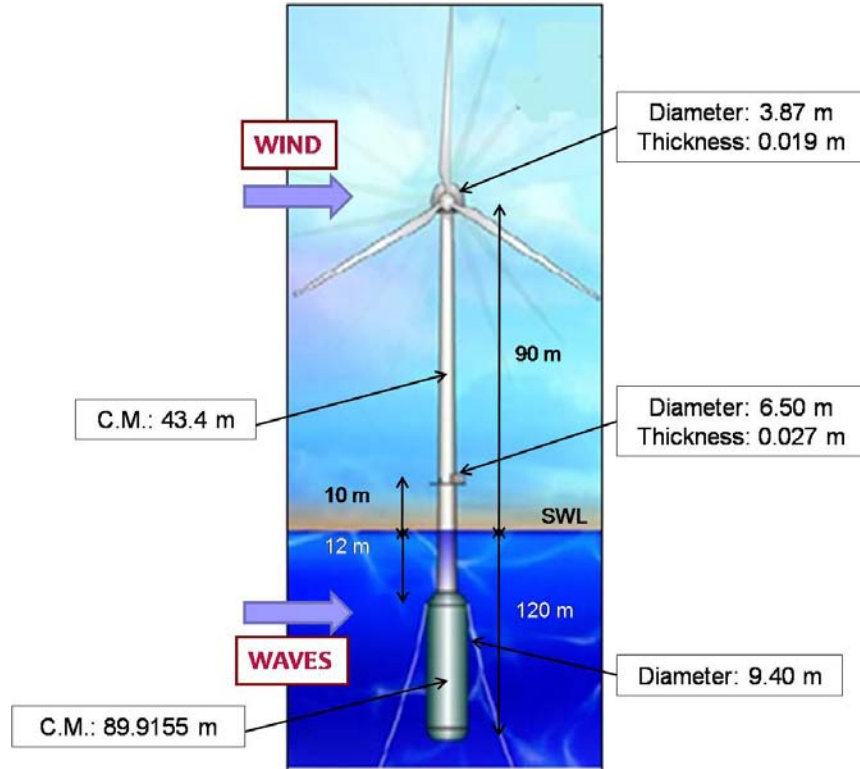


Figure 2.3: Schematic diagram of the spar buoy-supported floating offshore wind turbine.

Table 2.1: Structural properties of the wind turbine tower.

Elevation w.r.t. MSL (m)	Mass Distribution (kg/m)	Flexural Rigidity, EI^\dagger ($\text{N}\cdot\text{m}^2$)	Torsional Rigidity, GJ ($\text{N}\cdot\text{m}^2$)	Axial Rigidity, EA (N)	Moment of Inertia † ($\text{kg}\cdot\text{m}^2$)
10.00	4667.00	603.903E+9	464.718E+9	115.302E+9	24443.7
17.76	4345.28	517.644E+9	398.339E+9	107.354E+9	20952.2
25.52	4034.76	440.925E+9	339.303E+9	99.682E+9	17847.0
33.28	3735.44	373.022E+9	287.049E+9	92.287E+9	15098.5
41.04	3447.32	313.236E+9	241.043E+9	85.169E+9	12678.6
48.80	3170.40	260.897E+9	200.767E+9	78.328E+9	10560.1
56.56	2904.69	215.365E+9	165.729E+9	71.763E+9	8717.2
64.32	2650.18	176.028E+9	135.458E+9	65.475E+9	7124.9
72.08	2406.88	142.301E+9	109.504E+9	59.464E+9	5759.8
79.84	2174.77	113.630E+9	87.441E+9	53.730E+9	4599.3
87.60	1953.87	89.488E+9	68.863E+9	48.272E+9	3622.1

† These are for the fore-aft and side-to-side directions.

2.5.2 The Spar Buoy Platform and Mooring Lines Model

The floating platform model considered in our study is the same as the Offshore Code Comparison Collaboration (OC3) Phase IV spar buoy which is based on Statoil's "Hywind" spar platform (Jonkman et al, 2010). As mentioned before, the actual specifications of the selected spar for this study are somewhat different from that of Statoil's. The draft of the platform is 120 meters deep; the top and bottom portions of the spar buoy are made up of two cylinders of different diameter that are joined by a linearly tapered conical section. The top cylindrical section has a diameter of 6.5 m and extends down to 4 m below the SWL; the linearly tapered conical section extends from there to 12 m below the SWL, where the diameter increases to 9.4 m. The lower cylindrical portion of the spar buoy platform maintains this same diameter of 9.4 m. The resulting spar buoy platform has a center of mass located at a depth 89.9 m below the SWL. The water depth at the site selected for this study is taken to be 320 m.

The spar buoy platform achieves stability by the use of ballast weights. Due to the lower center of gravity (CG) relative to the center of buoyancy (CB) of the platform, whenever an overturning moment is produced due to wind or wave forces, a counteracting moment is generated between the center of gravity and the center of buoyancy which acts to return the spar buoy to its original position.

The selected spar buoy platform is connected to the sea floor by multi-component catenary mooring lines. These mooring lines are attached to the spar buoy at the fairleads. Mooring of the spar buoy platform prevents it from drifting. The three lines are modeled as homogeneous with properties derived as weighted average values of the line's mass and stiffness. The mooring system damping, including hydrodynamic drag and line-to-seabed drag, is neglected. Each of the three lines is assumed to have an unstretched length of 902.2 m and a diameter of 0.09 m. The lines are assumed to be at an angle of 120 degrees with respect to each other. The three mooring lines are anchored 320 m below the still water level. One of the lines is assumed to be directed along the positive X -axis (in the XZ plane). The lines are attached to the hull near its center of pitch for low dynamic loading such that when the platform deflects, the movement takes place in a plane of symmetry of the mooring system, the resultant horizontal force also occurs in this plane, and the behavior of the mooring system is two-dimensional. The mooring system is augmented with a yaw spring to achieve the proper overall yaw stiffness.

2.5.3 Inflow Turbulence and Aerodynamic Forces on the Blades

To simulate the 3-D inflow velocity fields, the computer program, TurbSim, is used (Jonkman and Buhl, 2007), which generates zero-mean u , v , and w (i.e., longitudinal, lateral, and vertical) components of turbulence over a 2-D grid covering the rotor plane. To the longitudinal direction, a non-zero mean velocity is added in each simulation. The expected value of the turbulence intensity (I_{ref}) at the turbine site is assumed to be 0.14 for a hub-height wind speed of 15 m/s consistent with medium

turbulence category B; the actual turbulence intensity varies with hub-height wind speed according to IEC 61400-1 (International Electrotechnical Commission, 2005).

A Kaimal power spectral density function is employed for the simulation of time series for each of the three turbulence components. Coherence for the longitudinal wind velocity component at different frequencies and for different spatial separations is described using an exponential coherence function. After the full 3-D random wind velocity field has been generated, aerodynamic forces on the blades are calculated using the program, AeroDyn, which is incorporated in FAST (see Figure 2.4).

2.5.4 Hydrodynamic Forces on the Floating Platform

Hydrodynamic loads on the floater result from the dynamic pressure of the water over the wetted surface of the support platform and account for the influence of added mass and damping. The added mass effect on hydrodynamic forces is important since the density of water is not insignificant relative to the density of the structural materials used for the support platform; this is in contrast to the aerodynamic loading on the rotor where effects of added mass may be neglected since the density of air is significantly lower than that of the materials used for the rotor.

The program, FAST, is used to simulate irregular long-crested waves describing a random sea surface elevation process; this is done using a JONSWAP spectrum defined in terms of two parameters, the significant wave height, H_s , and the peak spectral period, T_p (Det Norske Veritas, 2007). Wave kinematics employed are based on linear Airy wave theory with Wheeler stretching correction, and inertia and drag force components are computed using Morison's equation (see Figure 2.4).

2.5.5 Fast Simulation

The program, FAST, models a three-bladed horizontal-axis wind turbine as a multi-degree-of-freedom system comprised of nine rigid bodies and five flexible bodies. Overall, 24 degrees of freedom are represented in the turbine model; six of these describe the translational and rotational motions of the platform in three orthogonal directions. The tower is modeled as a flexible body and described by two vibratory modes each in the fore-aft and side-to-side directions. The tower is assumed to deflect, in general, as a linear combination of these mode shapes. The blades are also modeled as flexible systems using a modal representation; a total of nine mode shapes are represented which describe two flap-wise modes and one edge-wise mode per blade. The remaining five degrees of freedom describe nacelle yaw, generator azimuth angle, rotor furl, tail furl, and drive train rotational flexibility. In this study, we use only 22 degrees of freedom, leaving out the rotor furl and tail furl modes. The 5MW wind turbine model in this study has an active blade pitch controller which plays a key role in influencing loads on the machine; for instance, when the instantaneous hub-height wind speed exceeds the turbine's rated wind

speed, the blades pitch so as to alleviate aerodynamic loads while maintaining constant power production (Agarwal and Manuel, 2007; Agarwal, 2008).

The various forces on the spar buoy platform model include contributions from linear hydrostatic restoring; nonlinear viscous drag from incident wave kinematics, sea currents, and platform motion; frequency-dependent added-mass and damping arising from linear wave radiation, including free surface memory effects; and frequency- and direction-dependent wave excitation forces due to linear diffraction. FAST employs the frequency domain hydrodynamics of the spar buoy platform model in a time-domain computational module (HydroDyn) to derive hydrodynamic loads. The nonlinear restoring mooring loads from the time-domain hydrodynamic loads computation are included in the quasi-static mooring line solver (which accounts for the elastic stretching of an array of homogenous taut or slack catenary lines with seabed interaction); it is used to obtain the platform motions in each time step. As described, the time-domain hydrodynamic force computation module yields the hydrodynamic loads at each time step (see Figure 2.4).

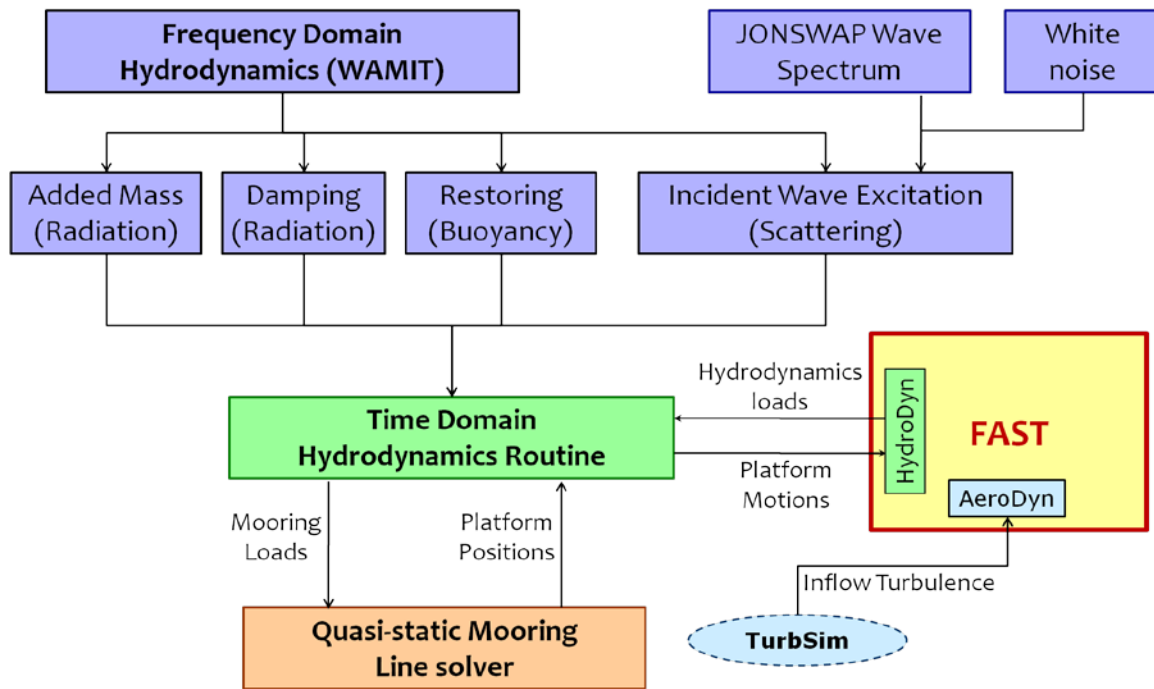


Figure 2.4: Computational Framework for the FAST Turbine Response Simulations.

2.6 System Transfer Functions

Detailed design stage analysis of wind turbines is generally carried out in the time domain in order to understand nonlinear dynamic characteristics of and transient events important to wind turbines.

In this study, time–marching integration of the nonlinear equations of motions is performed using a constant time step fourth-order Runge Kutta predictor-corrector scheme. Kane’s dynamics are used to derive the equations of motion. The equations of motion governing the six rigid body degrees of freedom of the floating platform may be summarized in matrix form as follows:

$$(\mathbf{M} + \mathbf{A})\ddot{\boldsymbol{\xi}}(t) + \mathbf{B}\dot{\boldsymbol{\xi}}(t) + \mathbf{C}\boldsymbol{\xi}(t) = a\mathbf{X}e^{i\omega t} \quad (2.1)$$

where

\mathbf{M} = 6×6 mass matrix;

\mathbf{A} = 6×6 added mass matrix;

\mathbf{B} = 6×6 damping matrix;

\mathbf{C} = 6×6 restoring matrix (stiffness);

\mathbf{X} = 6×1 vector of wave exciting forces and moments on the system;

a = wave amplitude;

ω = wave frequency;

$\boldsymbol{\xi}$ = 6×1 vector describing the system’s six modes of motion;

$\dot{\boldsymbol{\xi}}$ = 6×1 vector of system velocities;

$\ddot{\boldsymbol{\xi}}$ = 6×1 vector of system accelerations.

Expanding the mass, damping and stiffness matrices from Equation (2.1) into mass, damping and stiffness matrix contributions of the baseline wind turbine, the spar platform and the mooring lines model, we get:

$$\begin{aligned} & [\mathbf{M}_{\text{WT}} + \mathbf{M}_{\text{platform}} + \mathbf{A}(\omega)]\ddot{\boldsymbol{\xi}}(t) + [\mathbf{B}_{\text{WT}} + \mathbf{B}_{\text{Linear}} + \mathbf{B}_{\text{platform}}(\omega)]\dot{\boldsymbol{\xi}}(t) \\ & + [\mathbf{C}_{\text{WT}} + \mathbf{C}_{\text{platform}} + \mathbf{C}_{\text{Lines}}]\boldsymbol{\xi}(t) = a\mathbf{X}(\omega, \beta)e^{i\omega t} \end{aligned} \quad (2.2)$$

where $\mathbf{A}(\omega)$ and $\mathbf{B}_{\text{platform}}(\omega)$ are the added mass and damping matrices, respectively, for the spar platform that are obtained using the computer program, WAMIT. The program, FAST, is used to generate the mass, damping, and stiffness (restoring) matrices for the 5 MW baseline wind turbine (i.e., \mathbf{M}_{WT} , \mathbf{B}_{WT} , and \mathbf{C}_{WT}) at a steady-state operating point of static equilibrium. The process for evaluating these matrices for the baseline wind turbine model requires linearization of the dynamic coupled system about its initial equilibrium condition.

The mass matrix for the spar platform is given as follows:

$$\mathbf{M}_{\text{platform}} = \begin{bmatrix} m & 0 & 0 & 0 & mz_g & -my_g \\ 0 & m & 0 & -mz_g & 0 & mx_g \\ 0 & 0 & m & my_g & -mx_g & 0 \\ 0 & -mz_g & my_g & I_{11} & I_{12} & I_{13} \\ mz_g & 0 & -mx_g & I_{21} & I_{22} & I_{23} \\ -my_g & mx_g & 0 & I_{31} & I_{32} & I_{33} \end{bmatrix} \quad (2.3)$$

where, each matrix term, M_{ij} , describes inertia in DOF i produced by DOF j ; $m = \rho V$ is the body mass (ρ and V are the material unit weight and the volume of the body); x_g , y_g , and z_g are the coordinates of the center of gravity; I_{ij} are the moments of inertia defined in terms of radii of gyration r_{ij} , namely, $I_{ij} = \rho V r_{ij} |r_{ij}|$.

With the actual properties and dimensions for the spar platform, we have:

$$\mathbf{M}_{\text{platform}} = \begin{bmatrix} 7,466,330 \text{ kg} & 0 & 0 & 0 & -6.713 \times 10^8 \text{ kg} \cdot \text{m} & 0 \\ 0 & 7,466,330 \text{ kg} & 0 & 6.713 \times 10^8 \text{ kg} \cdot \text{m} & 0 & 0 \\ 0 & 0 & 7,466,330 \text{ kg} & 0 & 0 & 0 \\ 0 & 6.713 \times 10^8 \text{ kg} \cdot \text{m} & 0 & 4.229 \times 10^9 \text{ kg} \cdot \text{m}^2 & 0 & 0 \\ -6.713 \times 10^8 \text{ kg} \cdot \text{m} & 0 & 0 & 0 & 4.229 \times 10^9 \text{ kg} \cdot \text{m}^2 & 0 \\ 0 & 0 & 0 & 0 & 0 & 6.053 \times 10^{10} \text{ kg} \cdot \text{m}^2 \end{bmatrix}$$

Additional linear damping is added for the spar buoy hydrodynamics in FAST based on recommendations from the OC3 study. The damping matrix, $\mathbf{B}_{\text{Linear}}$, accounts for this additional damping and it is given as follows:

$$\mathbf{B}_{\text{Linear}} = \begin{bmatrix} 100,000 \text{ N/(m/s)} & 0 & 0 & 0 & 0 & 0 \\ 0 & 100,000 \text{ N/(m/s)} & 0 & 0 & 0 & 0 \\ 0 & 0 & 130,000 \text{ N/(m/s)} & 0 & 0 & 0 \\ 0 & 0 & 0 & 0 & 0 & 0 \\ 0 & 0 & 0 & 0 & 0 & 0 \\ 0 & 0 & 0 & 0 & 0 & 13,000,000 \text{ Nm/(rad/s)} \end{bmatrix}$$

The mass and aerodynamic damping matrices for the baseline wind turbine are obtained by linearization of the entire system about its initial equilibrium condition while setting the frequency-dependent hydrodynamic added-mass and damping matrices equal to zero in FAST (i.e., $A_{ij} = 0$, $B_{ij} = 0$). Thus, we have:

$$\mathbf{M}_{WT} = \begin{bmatrix} 603,670 \text{ kg} & 0 & 0 & 0 & 4.234 \times 10^7 \text{ kg} \cdot \text{m} & 0 \\ 0 & 603,670 \text{ kg} & 0 & -4.234 \times 10^7 \text{ kg} \cdot \text{m} & 0 & -145,000 \text{ kg} \cdot \text{m} \\ 0 & 0 & 603,670 \text{ kg} & 0 & 145,000 \text{ kg} \cdot \text{m} & 0 \\ 0 & -4.234 \times 10^7 \text{ kg} \cdot \text{m} & 0 & 6.377 \times 10^{10} \text{ kg} \cdot \text{m}^2 & 0 & 11,700,000 \text{ kg} \cdot \text{m}^2 \\ 4.234 \times 10^7 \text{ kg} \cdot \text{m} & 0 & 145,000 \text{ kg} \cdot \text{m} & 0 & 6.377 \times 10^{10} \text{ kg} \cdot \text{m}^2 & 0 \\ 0 & -145,000 \text{ kg} \cdot \text{m} & 0 & 11,700,000 \text{ kg} \cdot \text{m}^2 & 0 & -6.034 \times 10^8 \text{ kg} \cdot \text{m}^2 \end{bmatrix}$$

$$\mathbf{B}_{WT} = \begin{bmatrix} 118,600 \text{ N/(m/s)} & 0 & 0 & 0 & -58,110,000 \text{ N/(rad/s)} & 0 \\ 0 & 118,600 \text{ N/(m/s)} & 0 & 58,110,000 \text{ N/(rad/s)} & 0 & 0 \\ 0 & 0 & 0 & 0 & 0 & 0 \\ 0 & 7,254,000 \text{ Nm/(m/s)} & 0 & 5,230,000,000 \text{ Nm/(rad/s)} & 0 & 0 \\ -7,254,000 \text{ Nm/(m/s)} & 0 & 0 & 0 & 5,230,000,000 \text{ Nm/(rad/s)} & 0 \\ 0 & 0 & 0 & 0 & 0 & 0 \end{bmatrix}$$

The mooring lines are believed to not contribute much to the overall damping of the system and, hence, they are not included in the system damping. In order to derive the stiffness matrix for the spar platform, one needs to account for the restoring characteristics of the platform based on how it maintains stability. Figure 2.5 explains the restoring characteristics of the spar platform resulting from ballasting and water plane area.

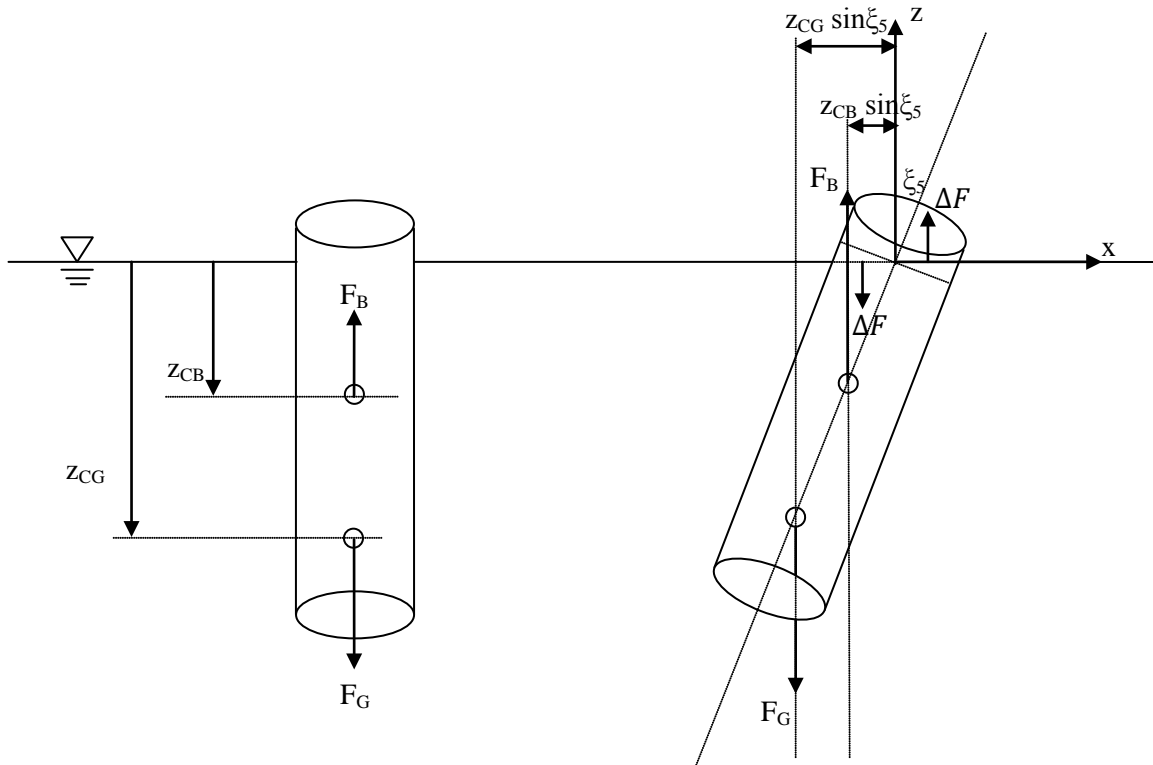


Figure 2.5: Restoring characteristics for a spar platform achieved by way of ballasting and water plane area (adapted from Wayman et al, 2006).

The restoring moment due to hydrostatic and inertial effects may be given as follows:

$$M_{Restoring} = M_B g z_{CB} \sin \xi_5 - M_G g z_{CG} \sin \xi_5 + \left(\rho g \iint x^2 dS \right) \sin \xi_5 \quad (2.4)$$

where M_B , M_G , z_{CB} , and z_{CG} are the gravitational mass, the buoyant masses, the vertical coordinate of the center of gravity, and the vertical coordinate of the center of buoyancy, respectively. Also, ξ_5 refers to the pitch motion of the platform and the last term in Equation (2.4) describes an integral over the water-plane area surface.

For small angles of platform pitch, the restoring moment may also be written as:

$$M_{Restoring} = \left(M_B g z_{CB} - M_G g z_{CG} + \rho g \iint x^2 dS \right) \xi_5 \quad (2.5)$$

Effectively, the restoring coefficient for an offset in pitch needed for the stiffness matrix in Equation (2.2) may be given as:

$$C_{55} = \left(M_B g z_{CB} - M_G g z_{CG} + \rho g \iint x^2 dS \right) \quad (2.6)$$

where, for a cylindrical spar buoy platform,

$$\iint x^2 dS = \frac{\pi R^4}{4} \quad (2.7)$$

Therefore, we have:

$$C_{55} = M_B g z_{CB} - M_G g z_{CG} + \rho g \frac{\pi R^4}{4} \quad (2.8)$$

where R is the radius of the cylinder representing the spar platform.

In a similar manner, the restoring coefficient corresponding to an offset in roll may be given as:

$$C_{44} = M_B g z_{CB} - M_G g z_{CG} + \rho g \frac{\pi R^4}{4} \quad (2.9)$$

Also, for restoring corresponding to an offset in yaw motion, we have:

$$C_{33} = \rho g \iint dS = \rho g \pi R^2 \quad (2.10)$$

Assuming small rotations and displacements,

$$\mathbf{C}_{\text{platform}} = \begin{bmatrix} 0 & 0 & 0 & 0 & 0 & 0 \\ 0 & 0 & 0 & 0 & 0 & 0 \\ 0 & 0 & \rho g \pi R^2 & 0 & -\rho g \iint x dS & 0 \\ 0 & 0 & 0 & \rho g \frac{\pi R^2}{4} + M_B g z_{CB} - M_G g z_{CG} & 0 & 0 \\ 0 & 0 & -\rho g \iint x dS & 0 & \rho g \frac{\pi R^2}{4} + M_B g z_{CB} - M_G g z_{CG} & 0 \\ 0 & 0 & 0 & 0 & 0 & 0 \end{bmatrix} \quad (2.11)$$

For the spar buoy platform of this study, we have:

$$\mathbf{C}_{\text{platform}} = \begin{bmatrix} 0 & 0 & 0 & 0 & 0 & 0 \\ 0 & 0 & 0 & 0 & 0 & 0 \\ 0 & 0 & 332,941 \text{ N/m} & 0 & 0 & 0 \\ 0 & 0 & 0 & -4,999,180,000 \text{ Nm/rad} & 0 & 0 \\ 0 & 0 & 0 & 0 & -4,999,180,000 \text{ Nm/rad} & 0 \\ 0 & 0 & 0 & 0 & 0 & 0 \end{bmatrix}$$

where the off-diagonal terms are zero due to symmetry of the spar buoy platform.

Additionally, the restoring (stiffness) coefficient matrices, $\mathbf{C}_{\text{Lines}}$ and \mathbf{C}_{WT} , for the mooring lines and wind turbine, respectively, in this study are:

$$\mathbf{C}_{\text{Lines}} = \begin{bmatrix} 41,180 \text{ N/m} & 0 & 0 & 0 & -2,821,000 \text{ N/rad} & 0 \\ 0 & 41,180 \text{ N/m} & 0 & 2821000 \text{ N/rad} & 0 & 0 \\ 0 & 0 & 11940 \text{ N/m} & 0 & 0 & 0 \\ 0 & 2,816,000 \text{ Nm/m} & 0 & 311,100,000 \text{ Nm/rad} & 0 & 0 \\ -2,816,000 \text{ Nm/m} & 0 & 0 & 0 & 311,100,000 \text{ Nm/rad} & 0 \\ 0 & 0 & 0 & 0 & 0 & 11,560,000 \text{ Nm/rad} \end{bmatrix}$$

$$\mathbf{C}_{WT} = \begin{bmatrix} 0 & 0 & 0 & 0 & 0 & 0 \\ 0 & 0 & 0 & 0 & 0 & 0 \\ 0 & 0 & 0 & 0 & 0 & 0 \\ 0 & 0 & 0 & 6,179,080,000 \text{ Nm/rad} & 0 & 0 \\ 0 & 0 & 0 & 0 & 6,179,080,000 \text{ Nm/rad} & 0 \\ 0 & 0 & 0 & 0 & 0 & 0 \end{bmatrix}$$

After defining the mass, damping and stiffness matrices for the entire system, the overall system transfer function, $\mathbf{T}(\omega)$, may be evaluated by using the following expression:

$$\mathbf{T}(\omega) = [-\omega^2(\mathbf{M} + \mathbf{A}(\omega)) + i\omega\mathbf{B}(\omega) + \mathbf{C}]^{-1} \quad (2.12)$$

Figure 2.6 shows transfer functions of the turbine system for each of the 6 rigid-body modes of motion response resulting from excitation by a unit harmonic load in the same direction. The surge and sway modes for the coupled system have peaks around 0.008 Hz, whereas the roll and pitch modes have peaks around 0.034 Hz. Similarly, transfer function peaks for heave and yaw motion occur around 0.032 Hz and 0.12 Hz, respectively. These transfer function peaks occur around the natural frequencies of the system for the corresponding mode of vibration; forcing at frequencies around these frequencies will be likely to cause the system to undergo large response. To reduce wave-induced motions, these natural frequencies of the spar buoy-supported floating offshore wind turbine system have been designed to be far from the peak frequency of the incident wave spectra. Additionally, the spar buoy support platform has such a deep draft that the surface wave action is offset by the counter-balance effect of the structure's weight.

Figure 2.7 shows coupled transfer functions between surge and pitch motions (T_{15} and T_{51}) and between sway and roll motions (T_{24} and T_{42}). When the system is excited by a pitching moment, significant coupling between pitch and surge results, leading to large surge motions. Similar significant coupling is seen between the roll and sway modes.

The loads that an offshore wind turbine experiences are strongly influenced by its various natural frequencies of vibration. The location of these natural frequency peaks relative to dominant peaks in the wave and wind power spectra directly influence turbine response and loads. The first nineteen natural frequencies of the wind turbine used in this study, along with brief descriptions of these vibration modes, are presented in Table 2.2.

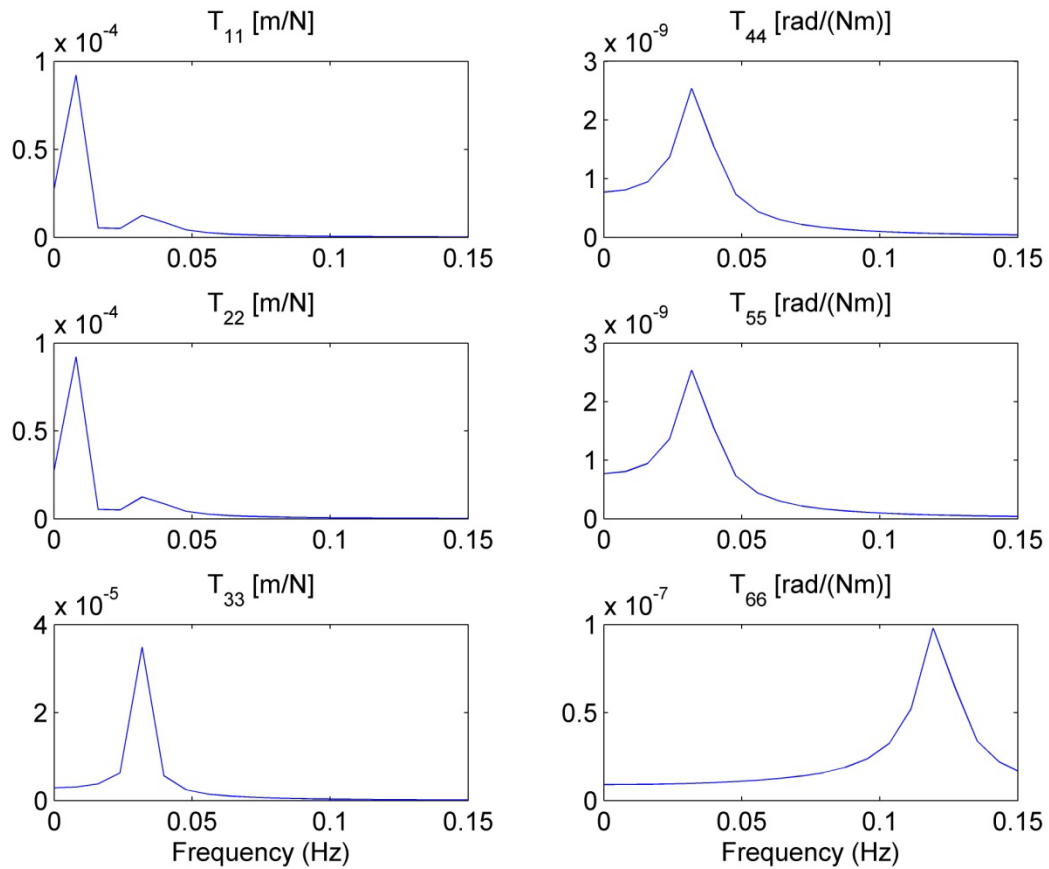


Figure 2.6: Transfer functions, T_{ii} , for the 6 rigid-body modes of the turbine system (surge, sway, heave, roll, pitch, and yaw) corresponding to the response of the i^{th} DOF due to unit harmonic load applied in the same direction (i.e., in the direction of the i^{th} DOF).

2.7 The Reference Site

In order to carry out loads analyses for the selected offshore floating wind turbine, we consider site-specific external conditions describing the wind and wave environment. The environmental data used here were obtained from the former Stevenson Weather Station site located on the Prime Meridian (i.e., at $61^{\circ}20'N$, $0^{\circ}0'E$), northeast of the Shetland Islands, which are in turn northeast of Scotland. Figure 2.8 shows the location of this site. This reference site was chosen for its fairly extreme wind and wave conditions expected to place significant environmental loading on the floating wind turbine system under consideration.

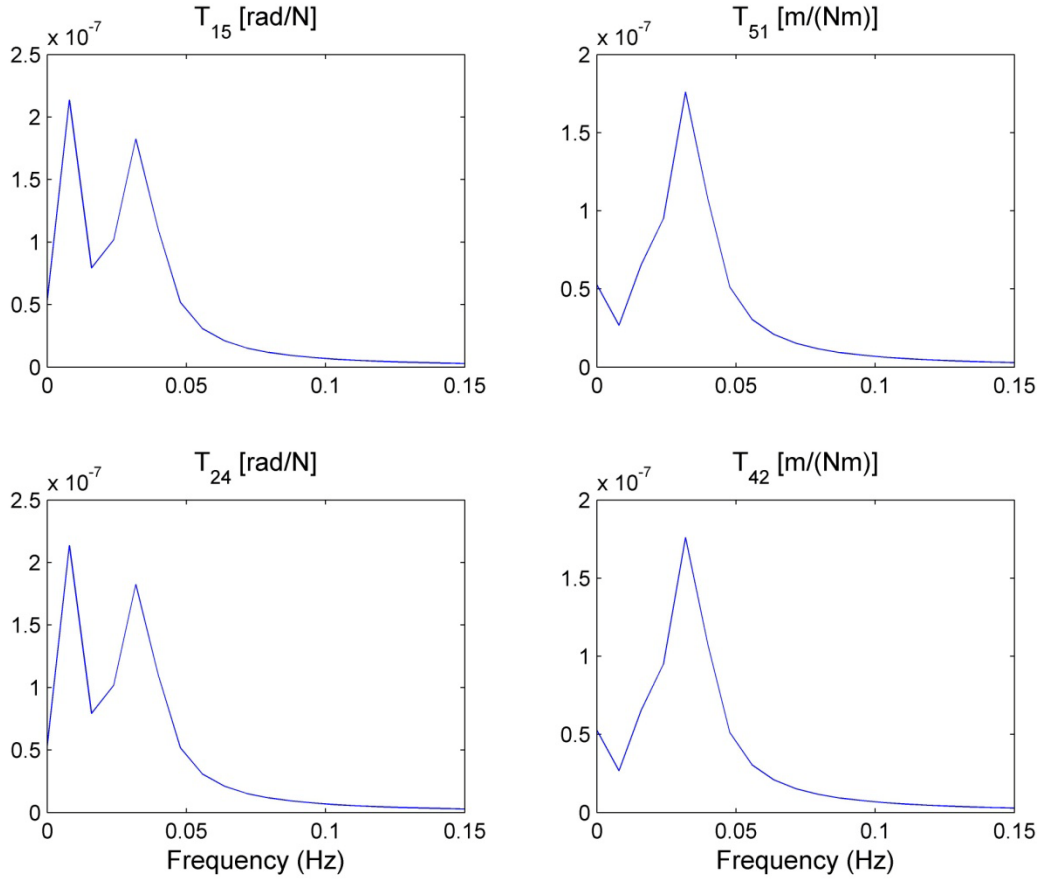


Figure 2.7: Transfer functions, T_{ij} , corresponding to the response of the i^{th} DOF due to unit harmonic load applied in the direction of the j^{th} DOF. Shown are transfer functions for the coupling action between the surge and pitch modes (T_{15} , T_{51}) and between the sway and roll modes (T_{24} , T_{42}).

Environmental wind and wave data for the selected site were provided in the form of joint probability histograms derived from 37,992 samples, each based on a 3-hour reference (averaging) period, representing a total of about 13 years of data. The joint distribution was grouped into bins with a mean wind speed bin width of 1.029 m/s, a significant wave height bin width of 1 m, and a peak spectral period bin width of 1.408 s. The reference elevation for the wind speed data was 10 m above the mean sea level; to represent the wind speed data at the turbine's hub height of 90 m, a vertical power-law shear exponent of 0.14 was assumed and all the wind speed bins were scaled by a factor, resulting in an altered bin width of 1.399 m/s for the hub-height wind speed, V_{hub} .

Table 2.2: A description of the floating wind turbine system's natural modes of vibration and corresponding natural frequencies.

Mode	Description	Natural Frequency (Hz)
1	Platform Surge	0.008
2	Platform Sway	0.008
3	Platform Heave	0.032
4	Platform Roll	0.034
5	Platform Pitch	0.034
6	Platform Yaw	0.121
7	1st Tower Fore-Aft	0.473
8	1st Tower Side-to-Side	0.457
9	1st Drivetrain Torsion	0.650
10	1st Blade Collective Flap	0.710
11	1st Blade Asymmetric Flapwise Pitch	0.678
12	1st Blade Asymmetric Flapwise Yaw	0.695
13	1st Blade Asymmetric Edgewise Pitch	1.081
14	1st Blade Asymmetric Edgewise Yaw	1.093
15	2nd Tower Fore-Aft	3.751
16	2nd Tower Side-to-Side	4.263
17	2nd Blade Collective Flap	2.023
18	2nd Blade Asymmetric Flapwise Pitch	1.933
19	2nd Blade Asymmetric Flapwise Yaw	1.957



Figure 2.8: The reference site chosen for the location of the offshore wind turbine in this study.

The water depth at the reference site is roughly 160 m; however, we performed our analyses for a water depth at the site of our turbine of 320 m assuming that the reference site conditions are reasonably representative of wind-wave conditions at a site with somewhat deeper waters. Standard values of 1.225 kg/m^3 for the air density and $1,025 \text{ kg/m}^3$ for the water density were assumed for the site. It was further assumed that the turbulence intensity at the study site conformed to IEC Turbulence Category B (International Electrotechnical Commission, 2005). In the sea surface elevation simulations, we used the JOint North Sea WAve Project (JONSWAP) spectrum (International Electrotechnical Commission, 2009).

2.8 Summary

This chapter presented a general background on offshore floating wind turbine technology. Offshore floating wind turbines are classified based primarily on alternative means by which they maintain stability. A spar buoy-supported offshore floating wind turbine achieves static stability based on the principle of ballast stabilization resulting from the restoring moment provided by the deep draft of the spar. Drifting of the spar-supported turbine system is prevented by a mooring system.

Model formulation for the baseline wind turbine, the spar platform, and the mooring system was presented. Next, we describe time-domain simulation studies on the selected spar buoy-supported offshore floating wind turbine where we focus primarily on short and long-term loads and motions.

Chapter 3: Extreme Loads on a Spar Buoy-Supported Floating Offshore Wind Turbine

3.1 Introduction

One of the challenges in the design of any floating offshore wind turbine system is the ability to predict the external forcing and the resulting dynamic loads and motions of the coupled wind turbine and platform system. In the offshore environment, additional load sources (to those experienced by land-based turbines) impart new and difficult challenges for wind turbine analysts. Our objective is to evaluate extreme loads for a spar buoy-supported floating offshore wind turbine at a site for which environmental data on wind and waves are available. Accurate load prediction depends on proper modeling of the stochastic processes describing the inflow wind velocity field and the waves as well as on realistic modeling of the turbine and the support structure.

To gain an understanding of the dynamic coupling between the support platform motion and the turbine loads, we first investigate short-term response statistics using stochastic simulation for a range of different environmental wind and wave conditions. From this study, we identify a few “controlling” environmental conditions for which long-term turbine load statistics and probability distributions are established.

To identify critical wind-wave conditions that can control long-term extreme loads, we study time histories, power spectra, response statistics, and probability distributions of loads. Extremes of platform motions as well as of tower and blade loads are studied. The present study only addresses “short-term” extreme load probability distributions (conditional on selected wind speed and wave height combinations). Findings from this study can be useful in addressing design load cases where such short-term load distributions are integrated with the likelihood of different environmental conditions to yield long-term loads associated with return periods on the order of 50 years.

In the following sections, we repeat some of the presentation related to the turbine and platform modeling, the loading, and the environment that was presented in Chapter 2 prior to discussing system short-term loads. This repetition is mainly to have, in one place, all the relevant system information while studying loads.

3.2 Simulation Model and Probabilistic Description of the Environment

3.2.1 The Baseline Wind Turbine Model

The NREL 5 MW baseline wind turbine model (Jonkman et al, 2009), developed to represent a typical utility-scale multi-megawatt wind turbine for offshore applications, is considered in the present

study. The turbine model is a conventional three-bladed variable-speed, collective pitch-controlled upwind machine. It was developed to support concept studies. Required structural properties and dimensions for the model were adapted from generic design information available in published documents of various turbine manufacturers, with greater emphasis on the REpower 5M machine. The selected turbine model is suitable for deployment in deep waters; it has a 126 m rotor diameter, a maximum rotor speed of 12.1 rpm, and a rated wind speed of 11.4 m/s. The turbine has a hub located 90 meters above the top of the support platform. The tower is modeled as a cantilever; its fixed base is coincident with the top of the supporting spar buoy platform. The tower base is at an elevation of 10 m above the SWL (still water level) where the tower's diameter is 6.5 m, which also matches the diameter of the top of the spar buoy platform. The cylindrical tower's base thickness is 0.027 m; the tower tapers linearly towards the top where its diameter reduces to 3.87 m and its thickness to 0.019 m. The resulting integrated tower mass is 249,718 kg with a center of mass (C.M.) located 43.4 m above the SWL. A damping ratio 1% of critical is specified for all the vibrational modes of the tower. Figure 2.3 shows a schematic diagram of the wind turbine and the supporting spar buoy platform.

3.2.2 The Spar Buoy Platform and Mooring Lines Model

The floating platform model considered in our study is the same as the Offshore Code Comparison Collaboration (OC3) Phase IV spar buoy which is based on Statoil's "Hywind" spar platform (Jonkman et al, 2010). As mentioned before, the actual specifications of the selected spar for this study are somewhat different from that of Statoil's. The draft of the platform is 120 meters deep; the top and bottom portions of the spar buoy are made up of two cylinders of different diameter that are joined by a linearly tapered conical section. The top cylindrical section has a diameter of 6.5 m and extends down to 4 m below the SWL; the linearly tapered conical section extends from there to 12 m below the SWL, where the diameter increases to 9.4 m. The lower cylindrical portion of the spar buoy platform maintains this same diameter of 9.4 m. The resulting spar buoy platform has a center of mass located at a depth 89.9 m below the SWL. The water depth at the site selected for this study is taken to be 320 m.

The spar buoy platform achieves stability by the use of ballast weights. Due to the lower center of gravity (CG) relative to the center of buoyancy (CB) of the platform, whenever an overturning moment is produced due to wind or wave forces, a counteracting moment is generated between the center of gravity and the center of buoyancy which acts to return the spar buoy to its original position.

The selected spar buoy platform is connected to the sea floor by multi-component catenary mooring lines. These mooring lines are attached to the spar buoy at the fairleads. Mooring of the spar buoy platform prevents it from drifting. The three lines are modeled as homogeneous with properties derived as weighted average values of the line's mass and stiffness. The mooring system damping, including

hydrodynamic drag and line-to-seabed drag, is neglected. Each of the three lines is assumed to have an unstretched length of 902.2 m and a diameter of 0.09 m. The lines are assumed to be at an angle of 120 degrees with respect to each other. The three mooring lines are anchored 320 m below the still water level. One of the lines is assumed to be directed along the positive X -axis (in the XZ plane). The lines are attached to the hull near its center of pitch for low dynamic loading such that when the platform deflects, the movement takes place in a plane of symmetry of the mooring system, the resultant horizontal force also occurs in this plane, and the behavior of the mooring system is two-dimensional. The mooring system is augmented with a yaw spring to achieve the proper overall yaw stiffness.

3.2.3 Inflow Turbulence and Aerodynamic Forces on the Blades

To simulate the 3-D inflow velocity fields, the computer program, TurbSim, is used (Jonkman and Buhl, 2007), which generates zero-mean u , v , and w (i.e., longitudinal, lateral, and vertical) components of turbulence over a 2-D grid covering the rotor plane. To the longitudinal direction, a non-zero mean velocity is added in each simulation. The expected value of the turbulence intensity (I_{ref}) at the turbine site is assumed to be 0.14 for a hub-height wind speed of 15 m/s consistent with medium turbulence category B; the actual turbulence intensity varies with hub-height wind speed according to IEC 61400-1 (International Electrotechnical Commission, 2005).

A Kaimal power spectral density function is employed for the simulation of time series for each of the three turbulence components. Coherence for the longitudinal wind velocity component at different frequencies and for different spatial separations is described using an exponential coherence function. After the full 3-D random wind velocity field has been generated, aerodynamic forces on the blades are calculated using the program, AeroDyn, which is incorporated in FAST (see Figure 2.4).

3.2.4 Hydrodynamic Forces on the Floating Platform

Hydrodynamic loads on the floater result from the dynamic pressure of the water over the wetted surface of the support platform and account for the influence of added mass and damping. The added mass effect on hydrodynamic forces is important since the density of water is not insignificant relative to the density of the structural materials used for the support platform; this is in contrast to the aerodynamic loading on the rotor where effects of added mass may be neglected since the density of air is significantly lower than that of the materials used for the rotor.

The program, FAST, is used to simulate irregular long-crested waves describing a random sea surface elevation process; this is done using a JONSWAP spectrum defined in terms of two parameters, the significant wave height, H_s , and the peak spectral period, T_p (Det Norske Veritas, 2007). Wave

kinematics employed are based on linear Airy wave theory with Wheeler stretching correction, and inertia and drag force components are computed using Morison's equation (see Figure 2.4).

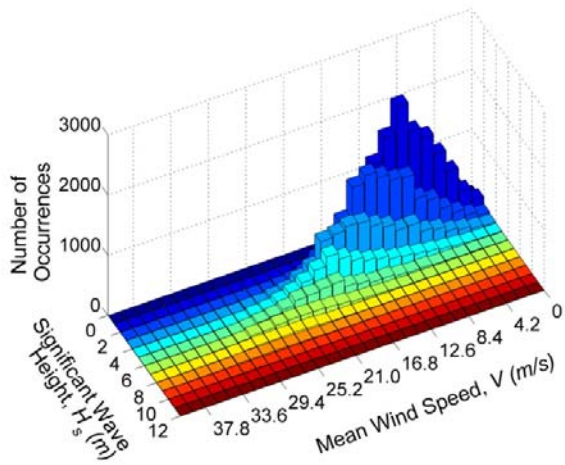
3.2.5 The Reference Site and Environmental Conditions

In order to carry out loads analyses for the selected offshore floating wind turbine, we consider site-specific external conditions describing the wind and wave environment. The environmental data used here were obtained from the former Stevenson Weather Station site located on the Prime Meridian (i.e., at 61°20'N, 0°0'E), northeast of the Shetland Islands, which are in turn northeast of Scotland. Figure 2.8 shows the location of this site. This reference site was chosen for its fairly extreme wind and wave conditions expected to place significant environmental loading on the floating wind turbine system under consideration.

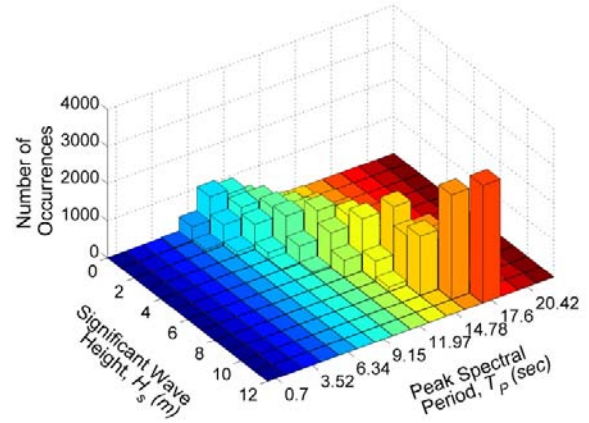
Environmental wind and wave data for the selected site were provided in the form of joint probability histograms derived from 37,992 samples, each based on a 3-hour reference (averaging) period, representing a total of about 13 years of data. The joint distribution was grouped into bins with a mean wind speed bin width of 1.029 m/s, a significant wave height bin width of 1 m, and a peak spectral period bin width of 1.408 s. The reference elevation for the wind speed data was 10 m above the mean sea level; to represent the wind speed data at the turbine's hub height of 90 m, a vertical power-law shear exponent of 0.14 was assumed and all the wind speed bins were scaled by a factor, resulting in an altered bin width of 1.399 m/s for the hub-height wind speed, V_{hub} .

The water depth at the reference site is roughly 160 m; however, we performed our analyses for a water depth at the site of our turbine of 320 m assuming that the reference site conditions are reasonably representative of wind-wave conditions at a site with somewhat deeper waters. Standard values of 1.225 kg/m³ for the air density and 1,025 kg/m³ for the water density were assumed for the site. It was further assumed that the turbulence intensity at the study site conformed to IEC Turbulence Category B (International Electrotechnical Commission, 2005). In the sea surface elevation simulations, we used the JOint North Sea WAve Project (JONSWAP) spectrum (International Electrotechnical Commission, 2009).

The joint statistics for the environmental random variables are assumed to be described by the ten-minute average mean wind speed, V , at the hub height, the significant wave height, H_s (four times the standard deviation of the sea surface elevation process), and the wave peak spectral period, T_p . The joint probability distribution for V , H_s , and T_p may be represented as shown in Figure 3.1 where only V - H_s and H_s - T_p bivariate distributions are presented, based on 13 years of data. The joint environmental distribution at the selected site is thought to be representative of deepwater sites that might be candidates for any floating offshore wind turbine such as the one analyzed in this study.



(a)



(b)

Figure 3.1: Joint distributions (based on data from the former Stevenson Weather Station site) showing (a) hub-height ten-minute mean wind speed versus significant wave height; and (b) significant wave height versus peak spectral period.

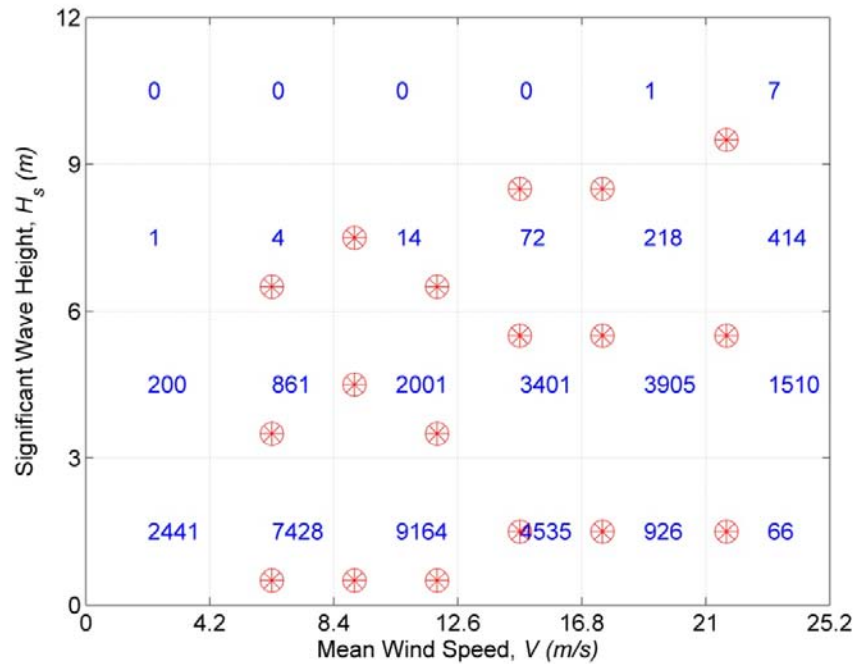


Figure 3.2: Representative sea states selected for analysis.

The various numbers shown on the V - H_s grid in Figure 3.2 indicate the number of 3-hour samples for each V - H_s bin. The circles indicate representative sea states selected based on probability mass for our

“short-term” loads study. These eighteen selected sea states cover the entire operating range of the wind turbine. The selection of triads of V , H_s and T_p values for detailed turbine loads analysis is made by first choosing six values of mean wind speed, V , over the entire operating range of the wind turbine from cut-in to cut-out winds ($V_{in} = 3 \text{ m/s} < V < V_{out} = 25 \text{ m/s}$). Then, for each wind speed, three different significant wave height values are chosen, corresponding to low, medium, and high values of H_s for the given V value, based on the joint V - H_s distribution. The selected wave peak spectral period, T_p , is that based on the conditional distribution of T_p on H_s and V ; the conditional expected value of T_p given H_s and V is used for each of the selected sets of environmental conditions used in subsequent analyses. A total of eighteen sea states are selected for the turbine stochastic response simulations; Table 3.1 summarizes the V , H_s and T_p values for these selected sea states.

Table 3.1: Sea states selected for the turbine response stochastic simulations.

$V \text{ (m/s)}$	<i>Low wave height</i>		<i>Medium wave</i>		<i>High wave height</i>	
	$H_s \text{ (m)}$	$T_p \text{ (s)}$	$H_s \text{ (m)}$	$T_p \text{ (s)}$	$H_s \text{ (m)}$	$T_p \text{ (s)}$
6.30	0.5	8.77	3.5	14.40	6.5	17.60
9.10	0.5	7.78	4.5	15.31	7.5	16.19
11.89	0.5	7.08	3.5	13.39	6.5	17.60
14.69	1.5	8.42	5.5	15.86	8.5	16.19
17.49	1.5	8.23	5.5	14.98	8.5	18.31
21.69	1.5	7.74	5.5	13.96	9.5	19.01

3.3 Stochastic Response Simulations

Fifteen ten-minute simulations of the turbine response were carried out for each of the selected eighteen sea states identified in Table 3.1; each ten-minute response series resulted from a separate wind velocity field simulation using TurbSim, followed by turbine response simulation using FAST. Data in the ten-minute time series were obtained with 20 Hz sampling; statistics including the maximum, mean, standard deviation, skewness, kurtosis, peak factor and mean upcrossing rate for each response process were studied. The load variables studied in some detail include the tower base fore-aft bending moment, the blade root out-of-plane bending moment, and the platform surge motion.

3.4 Numerical Studies

3.4.1 Time Series

Figure 3.3 shows various time series, normalized such that for any process, $y(t)$, what is plotted is $[(y(t)-E\{y\})/\max\{|y|\}]$ versus time, t . Time series presented are for the hub-height longitudinal wind speed (WindVxi), the sea surface elevation (WaveElev), the platform pitch (PtfmPitch) and surge (PtfmSurge)

motions that describe two of the rigid body motions of the platform, the tower base fore-aft bending moment ($TwrBsMyt$) and the blade root out-of-plane bending moment ($RootMyc1$). These various time series shown in Figure 3.3 correspond to the sea state where $V = 14.69$ m/s, $H_s = 8.5$ m, and $T_p = 16.19$ sec. From the time series, it may be noted that there is a dominant long period evident in the platform surge motion, exhibiting significant low-frequency content. The maximum platform surge motion is 27.7 m with a mean component of 15.9 m. There is some coupling or dynamic interaction between the surge and pitch modes; hence, the time series show considerable pitching of the system along with the large surge motions.

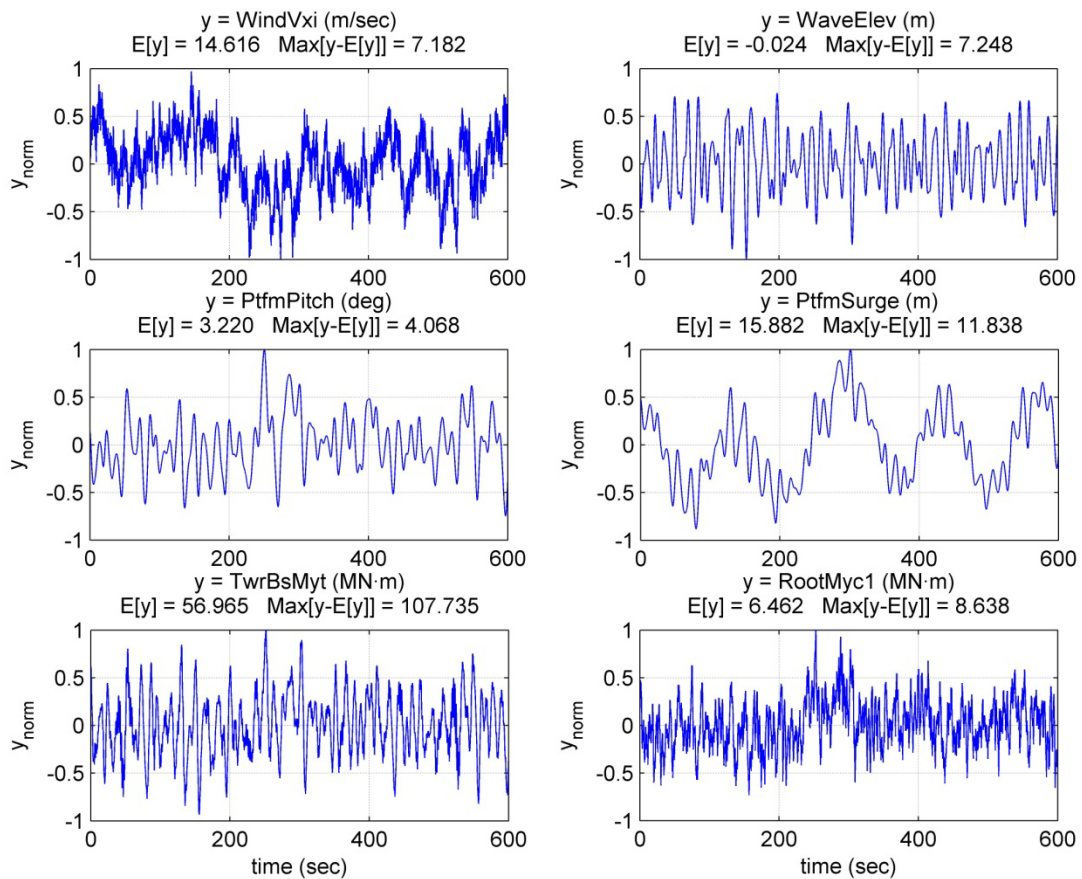


Figure 3.3: Time series of the hub-height longitudinal wind speed, the sea surface elevation, the platform pitch and surge motions, tower base fore-aft bending moment, and blade root out-of-plane bending moment for the floating offshore wind turbine for $V = 14.69$ m/s, $H_s = 8.5$ m, $T_p = 16.19$ s.

Time series for tower and blade loads are also presented in Figure 3.3 along with the hub-height longitudinal wind speed and the sea surface elevation. It is clear that the dynamic characteristics of the

tower base fore-aft bending moment (TwrBsMyt) are closely related to the sea surface elevation (WaveElev) process. The blade root out-of-plane bending moment (RootMyc1) shows more complex dynamic character due to contribution from both wind and waves; the direct influence of the turbulent wind along with the indirect influence from the sea surface elevation process, which is carried to the blade root via tower motion, are both evident. Time series of the blade-root out-of-plane bending moment (RootMyc1) and the tower base fore-aft bending moment (TwsBsMyt) exhibit comparatively greater high-frequency content compared to platform surge and pitch motions.

3.4.2 Response Statistics

To compare the relative importance of different wind speeds on loads, it is of interest to study load extreme statistics as a function of wind speed. From limited simulations, we can identify which wind speeds cause greater turbine loads on average and, equally important, which ones display greater load variability. Even if the loads realized for some wind speeds are not among the largest on average, if the variability in load extremes from simulations for some wind speeds is large, such winds can have a significant influence on load distribution tails and, hence, on large extrapolated loads (for those winds) that are associated with low probabilities of exceedance.

Extreme values are of great interest when estimating characteristic loads for design; the extreme value of interest here is the global maximum in a single ten-minute simulated load time series. This maximum value is related to other load statistics via the following equation:

$$Max = Mean + Std. Dev. \times PF \quad (3.1)$$

where the ten-minute extreme is defined as the ten-minute average (Mean) plus a peak factor (PF) times the standard deviation (Std. Dev.). Effectively, by definition, the ten-minute extreme occurs PF standard deviations above the mean. By studying each of the statistics that appear on the right-hand side of Equation (3.1), we can gain an understanding of the various turbine load processes and their extremes.

Figure 3.4 summarizes ensemble statistics of maximum, mean, and standard deviation from fifteen ten-minute simulations of the tower base fore-aft bending moment (TwrBsMyt) for all the eighteen selected sea states. The mean tower fore-aft bending moment increases as the mean wind speed increases from 6.30 m/s to 11.89 m/s; thereafter, it decreases monotonically with wind speed. This is as expected for this pitch-regulated wind turbine with a rated wind speed of 11.4 m/s. The largest ten-minute load extremes are seen to result near the mean wind speed bin of 14.69 m/s, and with the associated significant wave height of 8.5 m and wave spectral peak period of 16.19 sec. The mean value of the tower base fore-aft bending moment does not vary greatly for a given mean wind speed even with large changes in the

significant wave height. Second order statistics (i.e., estimates of the load standard deviation) are seen to increase with changes in significant wave height for a given mean wind speed. Ensemble maxima are largest at higher wind speeds than rated, despite low sensitivity of the ensemble standard deviation curve to wind speed. Ensemble maxima do not show the same trend in variation with wind speed as the ensemble mean. In order to better understand this behavior, a closer study of the load process peak factor (PF), which depends on higher-order load statistics such as skewness and kurtosis that influence the tail of the load distribution, needs to be undertaken.

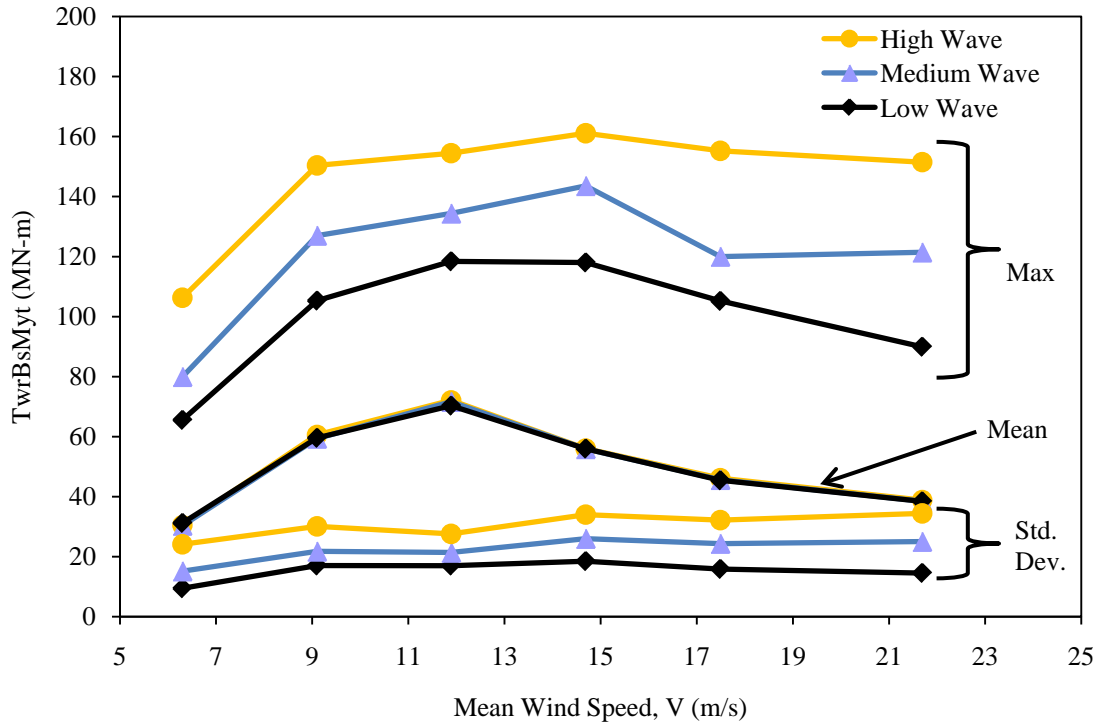


Figure 3.4: Ensemble tower base fore-aft bending moment statistics from fifteen ten minutes simulations for all eighteen sea states.

Table 3.2 summarizes ensemble statistics of maximum, mean, standard deviation, peak factor, skewness, kurtosis, and mean upcrossing rate from fifteen ten-minute simulations of the tower base fore-aft bending moment (TwrBsMyt) for four selected critical sea states out of the original eighteen sea states. For the four sea states considered, the mean fore-aft tower bending moment decreases by about 45% when we go from the smallest mean wind speed (11.89 m/s) with associated significant wave height (6.5 m) to the largest mean wind speed (21.69 m/s) with associated significant wave height (9.5 m). A decrease in mean load is expected based on the wind turbine's control characteristics. The turbine increases power output as the wind speed increases up to the rated wind speed (around 11.4 m/s); beyond

the rated wind speed, the turbine maintains constant power output. If the wind speed continues to increase to levels above the rated wind speed, the blades pitch to alleviate some of the structural load experienced. Constant power is maintained despite the blades pitching because the wind speed is higher. The standard deviation of the tower load is seen to increase significantly for sea states with higher V and H_s values. With increasing input energy from the wind and waves, the variance (and, thus, the standard deviation) of the load process is expected to increase—for instance, the tower bending moment standard deviation increases from 27.6 to 34.4 MN-m when going from the lower V - H_s sea state ($V = 11.89$ m/s, $H_s = 6.5$ m) to the higher one ($V = 21.69$ m/s, $H_s = 9.5$ m).

Table 3.2: Ensemble statistics of the tower base fore-aft bending moment from fifteen ten-minute simulations for four selected critical sea states.

V (m/s)	H_s (m)	T_p (sec)	Tower base fore-aft bending moment (TwrBsMyt) Statistics						
			Max (MN-m)	Mean(MN- m)	Std. Dev. (MN-m)	PF (on max)	Skewness	Kurtosis	Mean, Upcrossing Rate (s^{-1})
11.89	6.5	17.6	154.5	70.3	27.6	3.1	-0.07	2.86	0.15
14.69	8.5	16.2	161.1	56.0	34.0	3.1	0.04	2.91	0.13
17.49	8.5	18.3	155.3	45.4	32.2	3.4	0.06	3.03	0.15
21.69	9.5	19.0	151.5	38.4	34.4	3.3	0.05	2.96	0.14

The peak factor (PF) on the ten-minute extreme load is seen to increase slightly for sea states with higher V and H_s values. A random load process peak factor is directly related to the exposure time, to the asymmetry and tail behavior of the load distribution, and to the mean upcrossing rate of the process. The exposure time of ten minutes is the same for all four critical sea states. The asymmetry of the load distributions (represented by the coefficient of skewness values) is not significant here because these skewness coefficients are all very small (close to zero); likewise, kurtosis values which affect distribution tails and shape are not very different for the four sea states. The mean upcrossing rates of the load process are also almost the same for all the sea states. Overall, for three sea states ($V = 14.69$ m/s, $H_s = 8.5$ m; $V = 17.49$ m/s, $H_s = 8.5$ m; and $V = 21.69$ m/s, $H_s = 9.5$ m), the product of peak factor and standard deviation are comparable with each other and larger than that for the lowest sea state ($V = 11.89$ m/s, $H_s = 6.5$ m); for these three sea states, it is seen that the mean load decreases considerably with increase in wind speed. In summary, we see that the large decrease in the mean load, even though it is somewhat offset by an increase in standard deviation and an increase in peak factor (albeit only very slightly), leads to somewhat larger ten-minute maxima for $V = 14.69$ m/s, $H_s = 8.5$ m. Based on Eq. (3.1), we note that the maximum load is comparable for sea states with the higher wind speed and wave height because the

change in the mean load (a decrease) is offset by an opposite change (an increase) in the product of the standard deviation and the peak factor. For the tower base fore-aft bending moment, the controlling wind speeds lie in the range from 11.89 m/s to 21.69 m/s with perhaps the dominant winds being closest to mean wind speed of 14.69 m/s for this load.

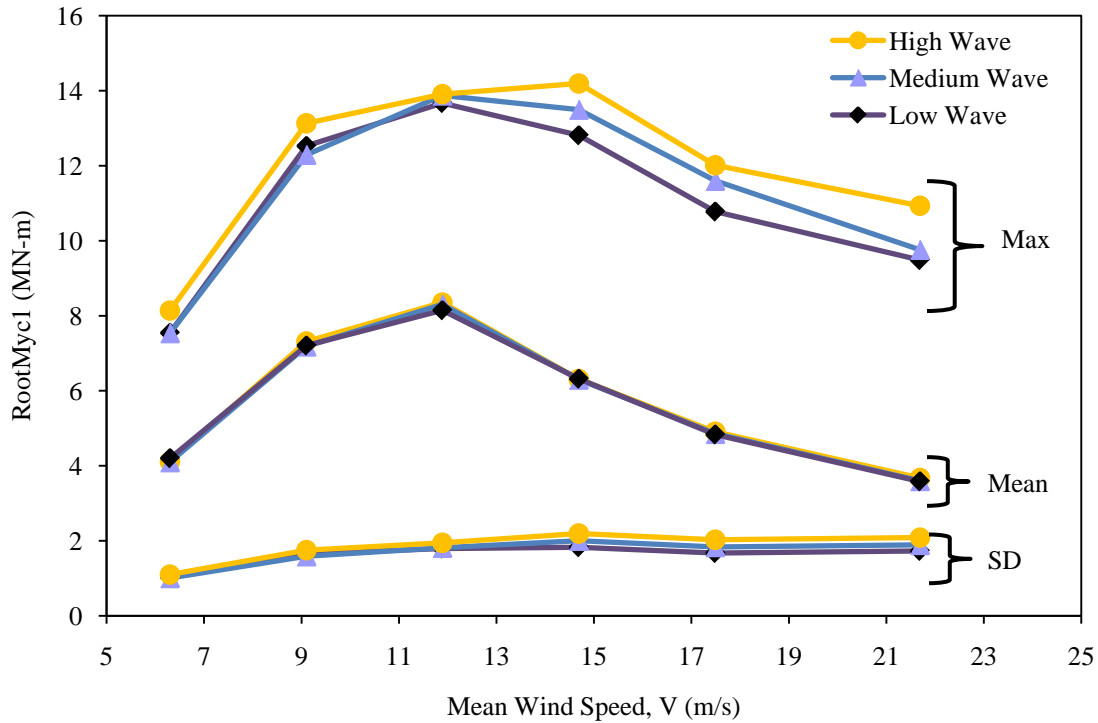


Figure 3.5: Ensemble blade root out-of-plane bending moment statistics from fifteen ten minutes simulations for all eighteen sea states.

Figure 3.5 summarizes ensemble statistics of maximum, mean, and standard deviation from fifteen ten-minute simulations of the blade root out-of-plane bending moment (RootMyc1) for all the eighteen selected sea states. The ensemble mean shows a decreasing trend beyond the rated wind speed due to the pitch control characteristics of the turbine. For a given mean wind speed, even with large changes in the significant wave height, the mean blade root out-of-plane bending moment does not vary greatly. Second order statistics (i.e., standard deviation estimates) also do not show much change with significant wave height for a given mean wind speed; there is a slight increase in standard deviation with increasing significant wave height for wind speeds above rated. Ensemble load maxima are largest near mean wind speeds somewhat above the rated wind speed despite the low sensitivity of the ensemble standard deviation curve to wind speed; ensemble load maxima do not follow the same trend as the mean load statistics near mean wind speeds $V = 11.89$ m/s and $V = 14.69$ m/s. The largest ten-minute load

extremes are seen to result near the mean wind speed bin of 14.69 m/s with the associated significant wave height of 8.5 m.

Table 3.3 summarizes ensemble statistics of the blade root out-of-plane bending moment (RootMyc1) for the four selected critical sea states. For the first three critical sea states, all with the same mean wind speed of $V = 11.89$ m/s, statistics of maximum, standard deviation, mean, PF, skewness, kurtosis, and mean upcrossing rates are very slightly different. The mean wind speed is close to the rated wind of $V = 11.4$ m/s for these sea states. Comparing statistics for one of these sea states (i.e., $V = 11.89$ m/s and $H_s = 6.5$ m) with those of the fourth critical sea state ($V = 14.69$ m/s and $H_s = 8.5$ m), we note that the mean out-of-plane blade root bending moment decreases by about 22% when we go from the mean wind speed (11.89 m/s) with associated significant wave height (6.5 m) to the mean wind speed (14.69 m/s) with associated significant wave height (8.5 m). Estimates of the standard deviation are higher for the $V = 14.69$ m/s and $H_s = 8.5$ m sea state by 16% as compared to the other sea state $V = 11.89$ m/s and $H_s = 6.5$ m. Even though the larger differences in the mean (for the two sea states) versus the opposite differences in standard deviation might suggest the lower wind speed case might experience the larger extreme, ensemble maxima are higher by 2% for the sea state with $V = 14.69$ m/s and $H_s = 8.5$ m as compared to the sea state with $V = 11.89$ m/s and $H_s = 6.5$ m. This is because the peak factor (PF) on the ten-minute extreme load is seen to increase by 20% when going from the sea state with $V = 11.89$ m/s and $H_s = 6.5$ m to that where $V = 14.69$ m/s and $H_s = 8.5$ m. The significantly larger skewness values which influence distribution tails lead to the larger PF values for the sea state with $V = 14.69$ m/s and $H_s = 8.50$ m. Kurtosis and mean upcrossing rates for the load process are almost the same for the two sea states. Overall, when going from the sea state with $V = 11.89$ m/s and $H_s = 6.5$ m to the sea state with $V = 14.69$ m/s and $H_s = 8.5$ m, the ten-minute extreme peak factor and the process standard deviation increased significantly so as to more than offset the decrease in mean load, resulting in higher maxima for the sea state where $V = 14.69$ m/s and $H_s = 8.5$ m.

Table 3.3: Ensemble statistics of the blade root out-of-plane bending moment from fifteen ten-minute simulations for four selected critical sea states.

V (m/s)	H_s (m)	T_p (sec)	Blade root out-of-plane bending moment (RootMyc1) Statistics						
			Max (MN-m)	Mean (MN-m)	Std. Dev. (MN-m)	PF (on max)	Skewness	Kurtosis	Mean, Upcrossing Rate (s^{-1})
11.89	0.5	7.1	13.7	8.4	1.8	3.0	-0.10	2.67	0.31
11.89	3.5	13.4	13.9	8.3	1.8	3.1	-0.11	2.76	0.31
11.89	6.5	17.6	13.9	8.1	1.9	3.0	-0.12	2.84	0.29
14.69	8.5	16.2	14.2	6.3	2.2	3.6	0.20	2.96	0.25

Figure 3.6 summarizes ensemble statistics of maximum, mean and standard deviation from fifteen ten-minute simulations of the platform surge (PtfmSurge) motion for all the eighteen selected sea states. The ensemble mean as well as extreme load show decreasing trends beyond the rated wind speed, due to pitch control characteristics of the turbine. All ensemble statistics for surge motion show only slight variation with wave height. The largest ten-minute surge extremes are seen to result near the mean wind speed bin of 11.89 m/s, for all the three associated significant wave heights of 0.5 m, 3.5 m and 6.5 m. The ensemble standard deviation also does not show much change with significant wave height for a given mean wind speed. In sum, surge motion maxima are largest near the mean wind speed, $V = 11.89$ m/s as is the case for the mean surge motion.

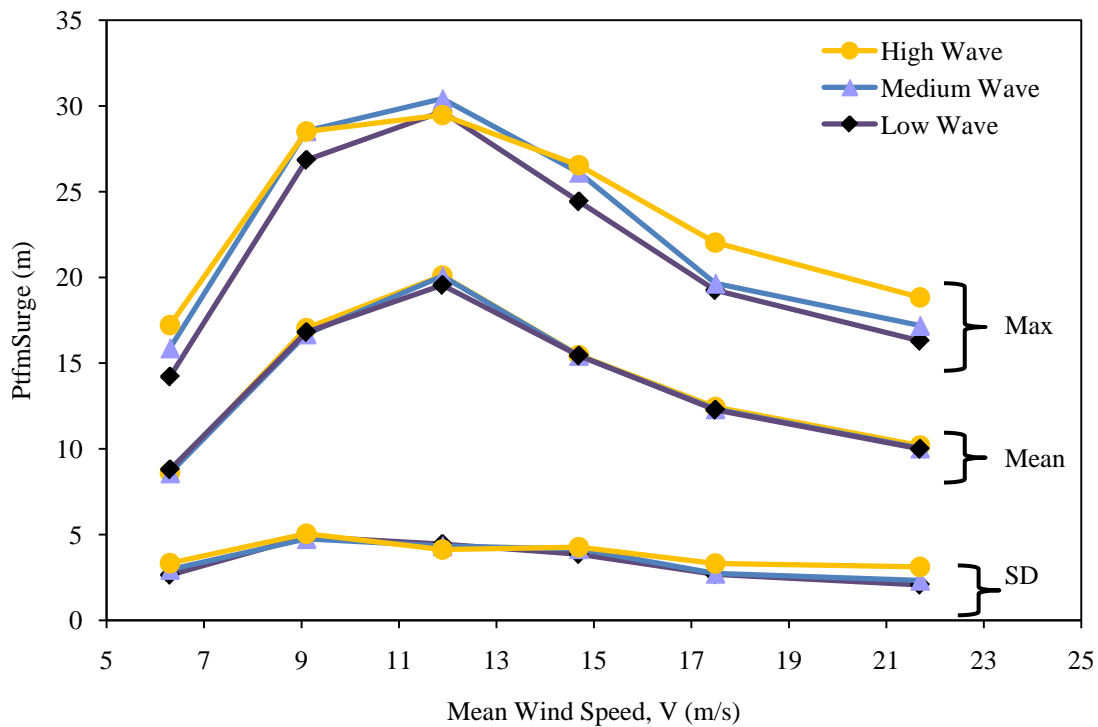


Figure 3.6: Ensemble platform surge statistics from fifteen ten minutes simulations for all eighteen sea states.

Table 3.4 summarizes ensemble statistics of the platform surge motion (PtfmSurge) for five selected critical sea states out of the eighteen sea states. The first two sea states have a mean wind speed of $V = 9.10$ m/s and the remaining three sea states have a mean wind of $V = 11.89$ m/s. For the first two sea states with the mean wind speed of $V = 9.10$ m/s, statistics of maximum, standard deviation, mean, and PF for the surge motion are only slightly different. Similarly, for the next three sea states with the

mean wind speed of $V = 11.89$ m/s, these statistics are again only slightly different. Comparing statistics on platform surge between the sea states with mean wind speeds of 9.10 m/s and 11.89 m/s, the mean platform surge motion shows an increment of about 20% as we go from the lower mean wind speed to the higher one. The standard deviation estimates, on the other hand, are somewhat lower for the higher mean wind speed. The net effect is that the ensemble maxima for surge motion are higher by approximately 4% for the sea state with $V = 11.89$ m/s. Note that higher-order statistics (skewness and kurtosis), peak factors, and upcrossing rates are almost the same for all the sea states. Overall, the ten-minute extreme platform surge motion is largely determined by the sea state that causes the larger mean surge motions with some offsetting effect resulting from the standard deviation.

Table 3.4: Ensemble statistics of the platform surge from fifteen ten-minute simulations for the selected critical sea states.

V (m/s)	H_s (m)	T_p (sec)	Platform Surge (PtfmSurge) Statistics						
			Max (m)	Mean (m)	Std. Dev. (m)	PF (on max)	Skewness	Kurtosis	Mean, Upcrossing Rate (s^{-1})
9.10	4.5	15.3	28.5	16.7	4.8	2.5	0.23	2.79	0.01
9.10	7.5	16.2	28.5	16.8	5.1	2.3	0.04	2.35	0.02
11.89	0.5	7.1	29.7	20.1	4.4	2.2	0.03	2.34	0.01
11.89	3.5	13.4	30.4	20.1	4.3	2.4	0.03	2.74	0.01
11.89	6.5	17.6	29.5	19.6	4.1	2.4	0.03	2.48	0.02

The wind speeds (and associated wave heights) where the largest turbine loads and/or largest platform motions occur are of obvious interest; these conditions tend to be associated with the rare loads that are of importance in design. Empirical short-term load distributions need to be accurately estimated for these important wind speed bins. From Tables 3.2, 3.3, and 3.4, it is clear that mean wind speeds bins below 11.89 m/s do not generally cause large tower and blade loads; they also do not exhibit large variability. These low mean wind speed bins are not generally important in statistical loads extrapolation for design and a minimal effort in terms of simulation may be justified for these mean wind speed bins. On the other hand, wind speeds at and above the rated wind speeds (with associated wave heights) are likely most important in long-term load prediction and greater effort in terms of simulation may be warranted in order to better understand rare loads/motions associated with distribution tails.

3.4.3 Short-Term Distributions for Turbine Loads and Platform Motions

Short-term distributions for various response variables based on fifteen ten-minute simulations for a mean wind speed of 14.69 m/s, a significant wave height of 8.5 m, and a wave peak spectral period of 16.19 sec are considered next. Cumulative distribution plots for the simulated hub-height longitudinal wind speed (WindVxi), the sea surface elevation (WaveElev), and various turbine response variables are presented in Figure 3.7.

From simulation to simulation, platform motions show greater variability than blade or tower loads (see, for example, surge motion), especially in the tails of the distributions. This is in part due to the slower process that defines platform surge which leads to fewer response cycles and process maxima in ten minutes.

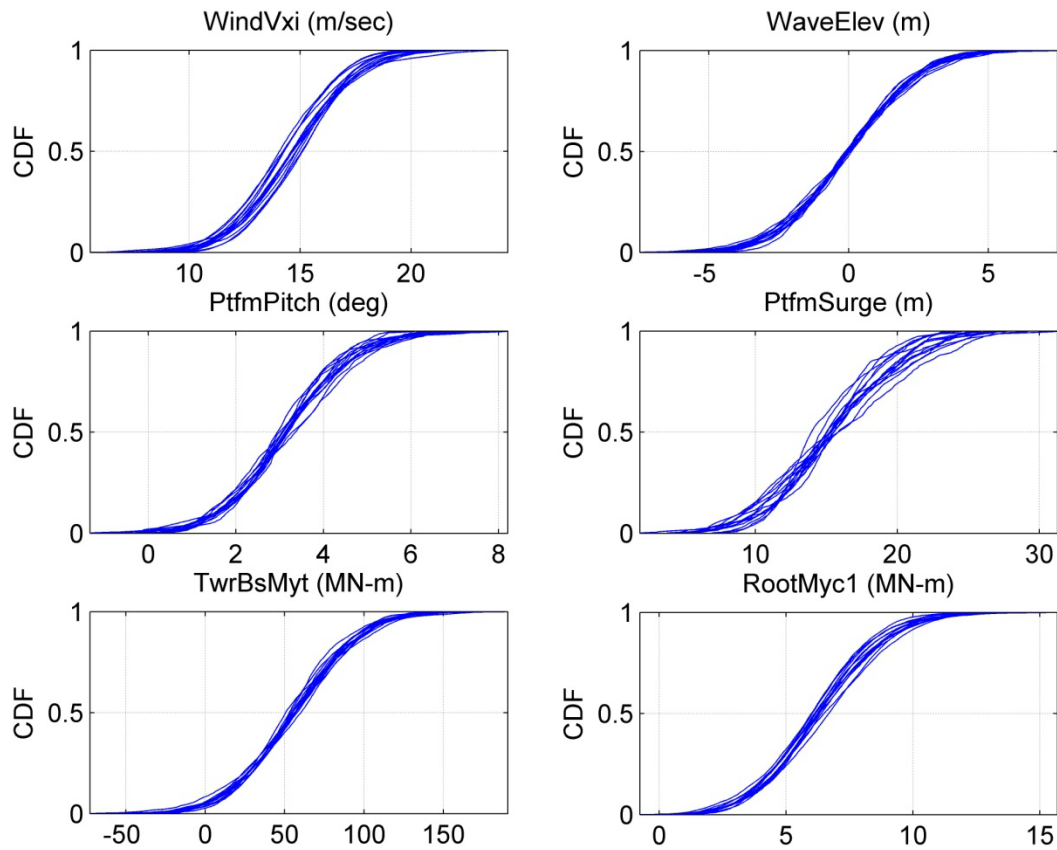


Figure 3.7: Cumulative distribution functions of the hub-height longitudinal wind speed, the sea surface elevation, and various turbine response variables based on fifteen ten-minute simulated time series with input environmental variables, $V = 14.69$ m/s, $H_s = 8.5$ m, and $T_p = 16.19$ s.

Platform surge motion (PtfmSurge) is seen to exhibit the greatest variability (among all response variables studied) for the selected environmental state. The turbine blade and tower response variables (RootMyc1 and TwrBsMyt) exhibit significantly lower variability compared to the platform motions. The tails of the various short-term distributions do indicate greater variability in the distribution tails than on the body for the tower- and blade-related response variables. This suggests that turbine tower and blade load extremes and long-term load prediction may not be established using only fifteen simulations. A greater number of simulations are needed for estimating such short-term load distributions for each important sea state. This issue is addressed later.

3.4.4 Power Spectra

Power spectral density function plots for the simulated hub-height longitudinal wind speed, the sea surface elevation, and various turbine response variables are presented in Figure 3.8 for a single ten-minute simulation with input environmental variables, $V = 14.69$ m/s, $H_s = 8.5$ m, and $T_p = 16.19$ s. It is evident that background (low-frequency) energy from the wind contributes differently to the various turbine response measures studied compared to relevant resonant components in each case. For the environmental conditions considered here, the wave energy is concentrated around 0.06 Hz—i.e., at frequencies higher than those of the slower platform motions associated, say, with surge (around 0.008 Hz). The effectiveness of the coupled dynamic system is evident from the energy concentrated at low natural system frequencies in contrast to the environmental wave conditions. For frequencies of excitation well above any system natural frequency, the mass cannot “follow” the excitation; consequently, the response levels are low and the response is almost in counter-phase with the excitation and the inertia of the system dominates the response. Greater low-frequency content is observed for the turbine platform motions, PtfmSurge and PtfmPitch, compared to that for the tower and blade bending moments, TwrBsMyt and RootMyc1, respectively.

The influence of waves on turbine response is studied by considering significant wave heights of 0.5 m, 3.5 m and 6.5 m, while the mean wind speed is held constant at 11.89 m/s. In Figure 3.9, power spectral density function plots for the simulated hub-height longitudinal wind speed, the sea surface elevation, and various turbine response variables are presented. Blade loads show relatively little sensitivity to change in wave height. Power spectra for tower loads, too, show no significant influence of change in wave height, except at low frequencies below 0.2 Hz where the wave energy is dominant; sea surface elevation power spectrum peak frequencies are at 0.14 Hz, 0.074 Hz, and 0.056 Hz, respectively, for significant wave heights of 0.5, 3.5 and 6.5 m.

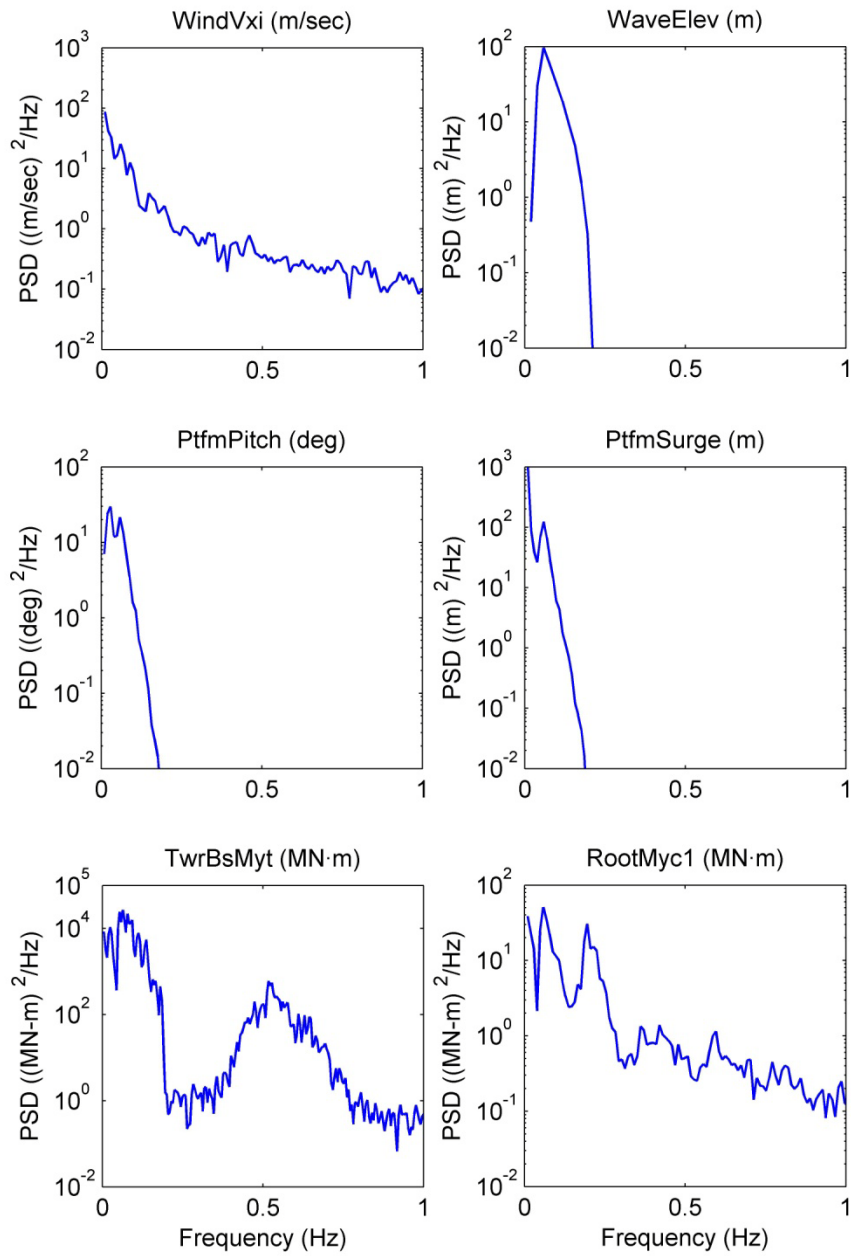


Figure 3.8: Power spectral density functions of the hub-height longitudinal wind speed, the sea surface elevation, and various turbine response variables for a single ten-minute simulated time series with input environmental variables, $V = 14.69$ m/s, $H_s = 8.5$ m, and $T_p = 16.19$ s.

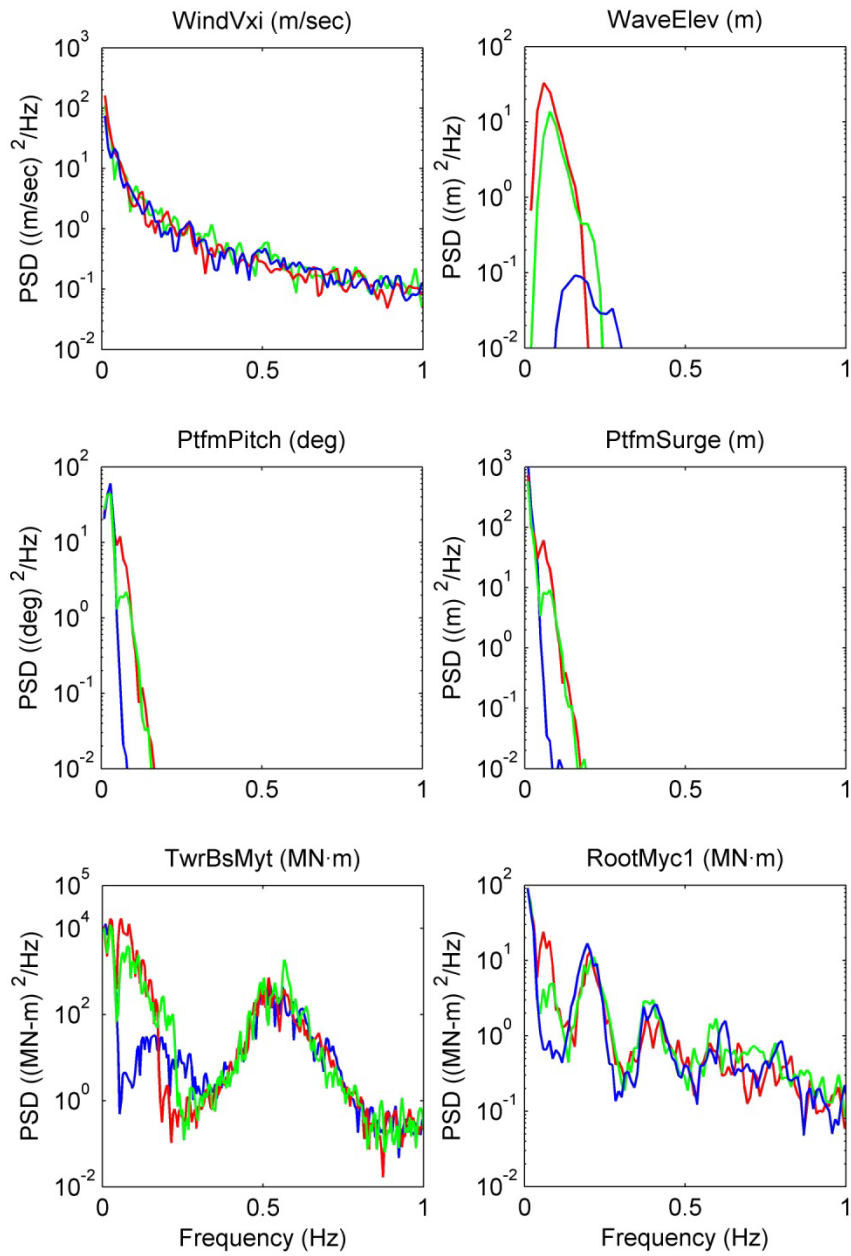


Figure 3.9: Variation in power spectral density functions of the hub-height longitudinal wind speed, the sea surface elevation, and various turbine response variables as the significant wave height is changed for a fixed ten-minute average longitudinal hub-height mean wind speed of 11.89 m/s (blue: $H_s = 0.5$ m; green: $H_s = 3.5$ m; red: $H_s = 6.5$ m).

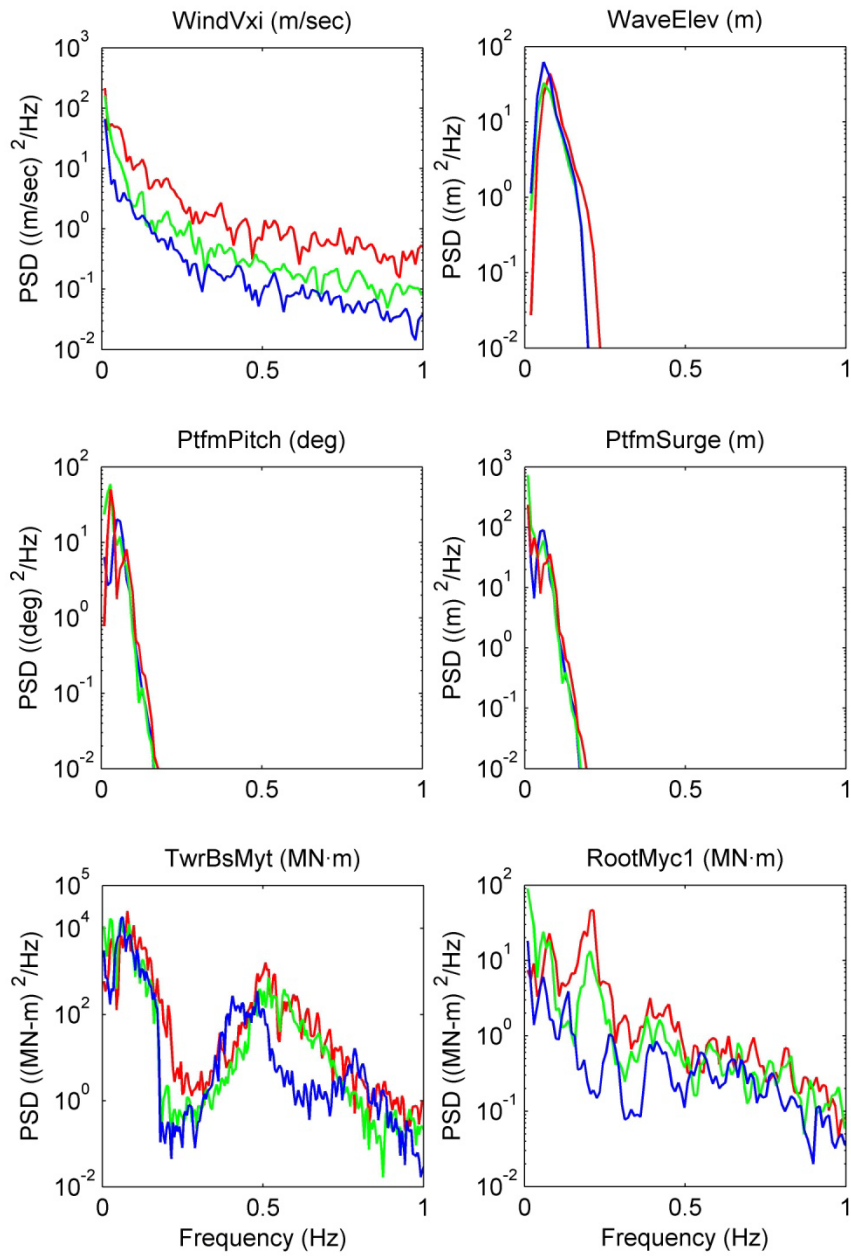


Figure 3.10: Variation in power spectral density functions of the hub-height longitudinal wind speed, the sea surface elevation, and various turbine response variables as the ten-minute average hub-height longitudinal wind speed is changed for a fixed significant wave height of 6.5 m (blue: $V = 6.30$ m/s; green: $V = 11.89$ m/s; red: $V = 21.69$ m/s).

The influence of change in wind speed on turbine response is studied by considering hub-height ten-minute average longitudinal wind speeds of 6.30 m/s, 11.89 m/s, and 21.69 m/s, while the significant wave height is held constant at 6.5 m. In Figure 3.10, power spectral density function plots for the simulated hub-height longitudinal wind speed, the sea surface elevation, and various turbine response variables are presented. It can be seen that, in general, blade and tower loads exhibit increased levels of energy (variance) with increase in wind speed. Even though the mean tower bending moment is higher for wind speeds around rated (Table 3.2), the variance (equal to the area under the power spectral density function plot versus frequency) is smaller at those wind speeds than at 21.69 m/s (Figure 3.10). Important peaks in the power spectra for the blade loads are seen at 1P (corresponding to the rotor rotation rate which is 0.2 Hz at and above the rated wind speed) and multiples. Peaks in the power spectra plots for the turbine response shift more noticeably with variation in wind speed (Figure 3.10) than they do with variation in wave height (Figure 3.9).

3.4.5 Interpretation of Short-Term Response Statistics

The coupled dynamics between the wind turbine and supporting spar buoy platform may be better understood by studying the response for different environmental input sea state triads of mean wind speed (V), significant wave height (H_s) and peak wave period (T_p). Choosing sea states (V, H_s, T_p) triads of— $V = 14.69$ m/s, $H_s = 8.50$ m, $T_p = 16.19$ s and $V = 9.10$ m/s, $H_s = 7.50$ m and $T_p = 16.19$ s—such that the wave period for both sea states is almost the same, we can assess the effect of the controller on the coupled dynamics of the spar buoy-supported offshore floating wind turbine. We study response time series and power spectra for these two sea states where one input triad represents wind speeds below the rated wind speed (11.4 m/s) and other represents wind speeds above the rated wind speed of the turbine system. The locations of the resonance peaks for the different vibration modes of the system relative to the dominant wave and wind energy power spectra directly influence turbine response and loads; hence, wave and wind influences are studied for different input conditions—steady mean wind (no turbulence) with still water (no waves), stochastic wind (inflow turbulence) with still water, steady mean wind with JONSWAP waves, and stochastic wind with JONSWAP waves. Such a study allows us to gain an understanding of various turbine vibration modes and their interaction with the wind and wave energy separately. This can help us gain a better understanding of the turbine behavior.

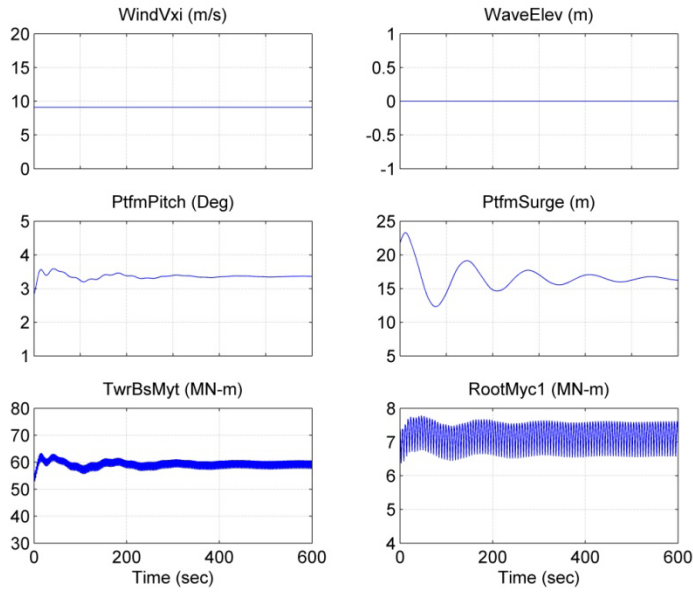
From Figure 3.11, we see in Plots (b) and (d) that the power spectra of the fore-aft tower base bending moment (TwrBsMyt) and out-of plane blade root bending moment (RootMyc1) for both sea states with different steady wind conditions and still water (no waves) are very similar. Most of the energy content in the out-of-plane blade root bending moment process is concentrated around the 1P frequency. This 1P frequency refers to the frequency at which the rotor makes a complete revolution. For

sea states with hub-height mean wind speed below the rated wind speed, the rotor rotates at a speed of 10.5 rpm (Jonkman et al, 2009) or approximately 0.175 Hz as can be confirmed from Figure 3.11 (b). For sea states with hub-height mean wind speed above the rated wind speed, the rotor rotates at a speed of 12.1 rpm or approximately 0.2 Hz as can be confirmed from Figure 3.11 (d). For the fore-aft tower base bending moment process, response energy is concentrated around the first fore-aft tower bending natural frequency of 0.473 Hz (see Table 2.2) with possible interaction from the 3P frequency and some low-frequency influence from the platform surge and pitch modes.

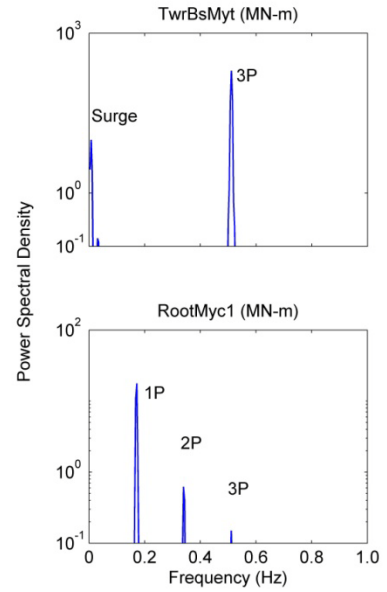
After the removal of the first minute of transients, the time series in Figures 3.11 (a) and (c) of the platform pitch and surge motion show damped oscillatory behavior during the first 200 seconds resulting from the presence of the aerodynamic damper placed along the surge axis of the turbine model. The thrust due to the steady wind at hub height generates the pitch motion in the turbine which has an influence on the surge motion (as can be explained by the coupling between the pitch and surge motions discussed earlier). High-frequency oscillatory behavior at 1P can be seen in the out-of-plane blade root bending moment time series and tower resonance frequency energy is evident in the fore-aft tower base bending moment time series.

Power spectra of the fore-aft tower bending moment process and the out-of-plane blade root bending moment process for the environmental input of steady wind with JONSWAP wave input for two sea states are presented in Figures 3.12 (b) and (d). The influence of the natural frequencies of the turbine system on the frequency content of the fore-aft tower base bending moment (TwrBsMyt) and the out-of-plane blade root bending moment (RootMyc1) for both sea states is evident. Figures 3.12 (b) and (d) show participation from a greater number of modes of vibration compared to the case (in Figures 3.11 (b) and (d)) with environmental input of steady wind and still water; also, the response energy (variance) is seen to increase dramatically with the introduction of waves relative to the still water case. Compared to the still water case, the energy content in the out-of-plane blade root bending moment process has increased and indicates some contribution from the waves. The fore-aft tower base bending moment process power spectra show even greater energy enhancement due to introduction of the wave energy. The first tower fore-aft bending vibration mode is evident in power spectra for both sea states; some higher frequency energy is also evident in the power spectra for the tower bending moment.

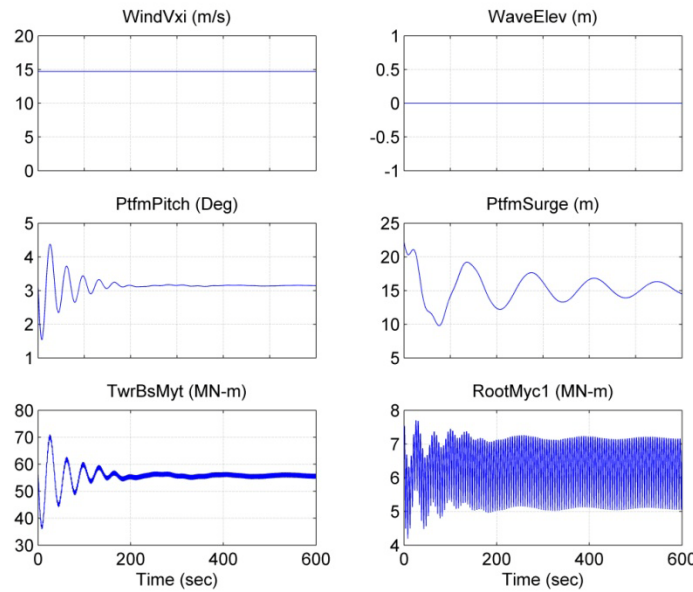
Time series for this case with steady wind in combination with waves for two sea states are presented in Figures 3.12 (a) and (c). The simulation time for the entire process is same as for the previous environmental wind-wave condition. The various turbine response processes—platform motions as well as tower and blade moments—clearly show a wider range of dynamic response characteristics compared to the characteristics of the response time series due to the environmental input consisting of steady wind with still water (no waves) that were studied in Figures 3.11 (a) and (c).



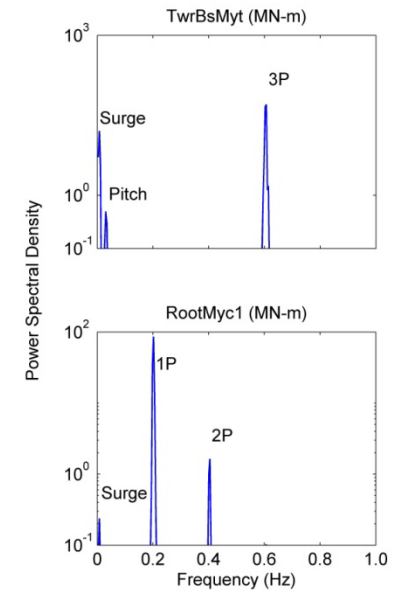
(a)



(b)



(c)



(d)

Figure 3.11: Representative time series and power spectral density functions of the hub-height longitudinal wind speed, the sea surface elevation, the fore-aft tower base bending moment, the out-of-plane blade root bending moment, the platform surge motion, and the platform pitch motion for the floating offshore wind turbine for still water (no waves). Plots (a) and (b) are for a steady mean wind speed of $V = 9.1$ m/s while Plots (c) and (d) are for a steady mean wind speed of $V = 14.7$ m/s.

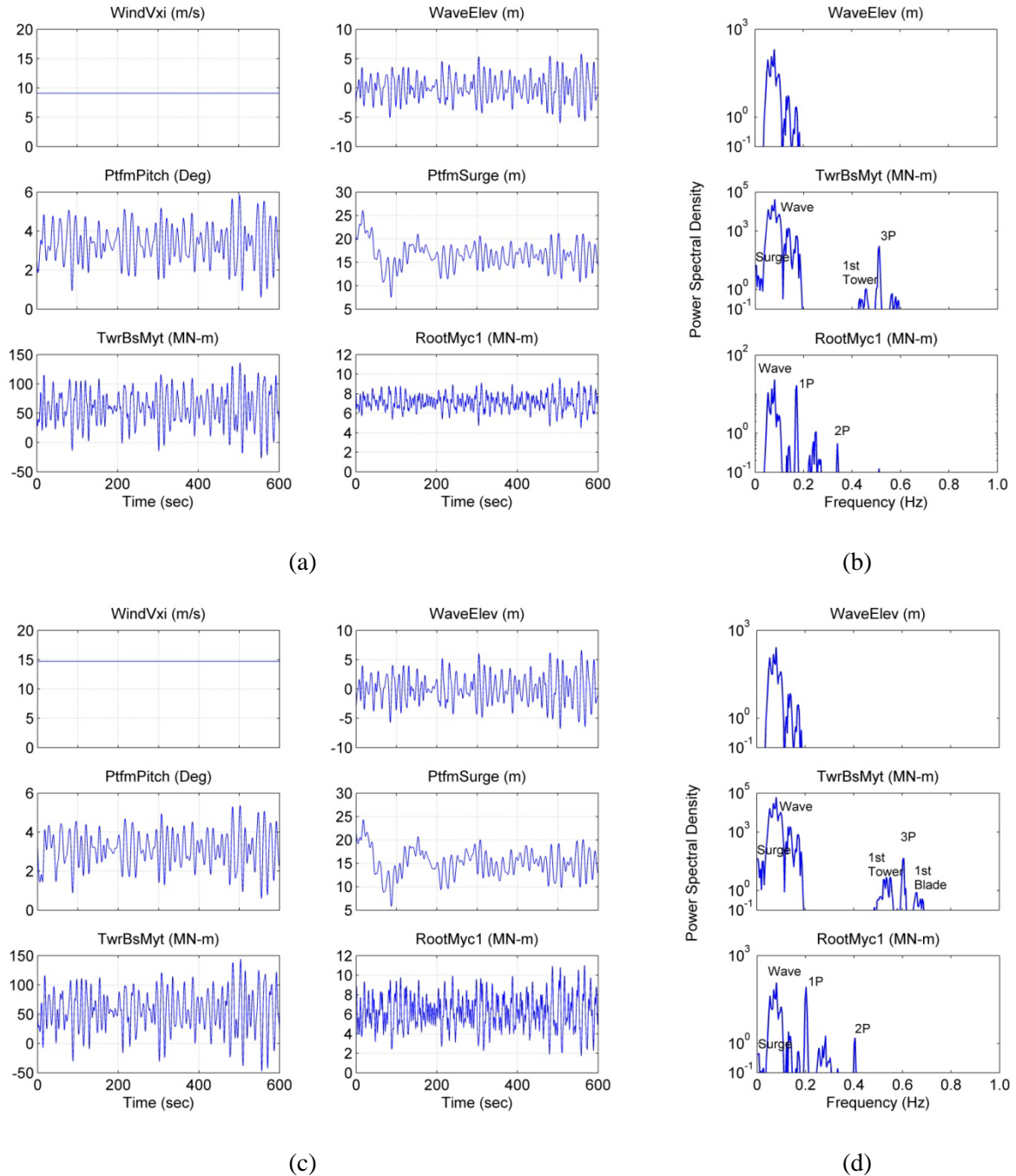


Figure 3.12: Representative time series and power spectral density functions of the hub-height longitudinal wind speed, the sea surface elevation, the fore-aft tower base bending moment, the out-of-plane blade root bending moment, the platform surge motion, and the platform pitch motion for the floating offshore wind turbine for steady wind (no turbulence). Plots (a) and (b) are for $V = 9.1$ m/s, $H_s = 7.5$ m, $T_p = 16.19$ s while Plots (c) and (d) are for $V = 14.7$ m/s, $H_s = 8.5$ m, $T_p = 16.19$ s.

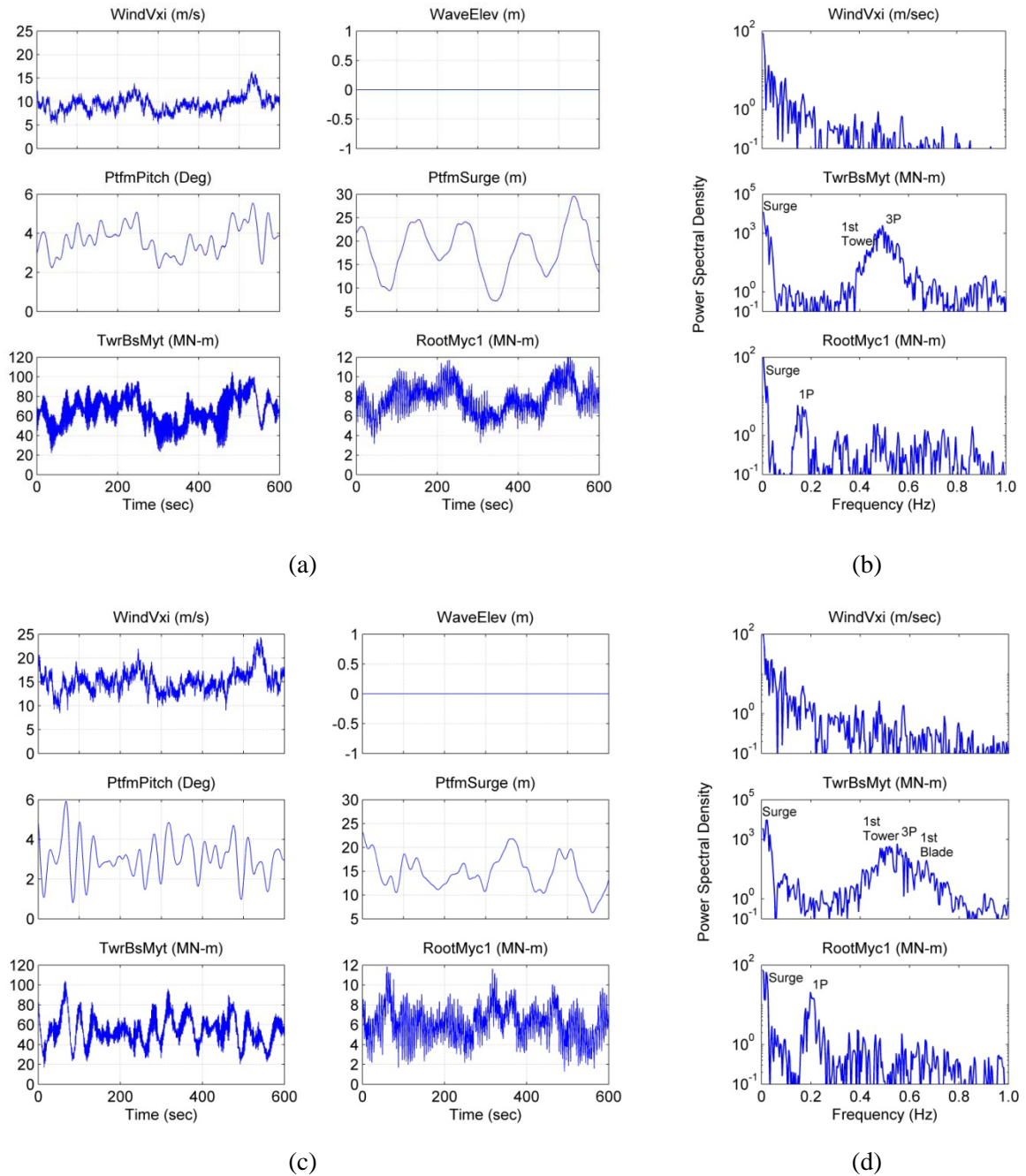


Figure 3.13: Representative time series and power spectral density functions of the hub-height longitudinal wind speed, the sea surface elevation, the fore-aft tower base bending moment, the out-of-plane blade root bending moment, the platform surge motion, and the platform pitch motion for the floating offshore wind turbine for still water (no waves). Plots (a) and (b) are for a stochastic wind field with $V = 9.1$ m/s while Plots (c) and (d) are for a stochastic wind field with $V = 14.7$ m/s.

Next, we consider power spectra of the fore-aft tower bending moment process and out-of-plane blade root bending moment process for the environmental input consisting of stochastic wind with still water (no waves) for two sea states. In Figures 3.13 (b) and (d), the influence of the low-frequency wind input on the frequency content of the fore-aft tower base bending moment (TwrBsMyt) and the out-of-plane blade root bending moment (RootMyc1) power spectra for both sea states is clearly significant; this background energy also drives the surge response as well. The power spectra for the out-of-plane blade root bending moment process also show significant energy due to the 1P frequency as was observed in power spectra plots in Figures 3.11 and 3.12 for other environmental inputs. The fore-aft tower base bending moment process power spectra show significant energy content at and around the first tower fore-aft bending natural frequency. Time series, shown in Figures 3.13 (a) and (c), show clear evidence of low-frequency cycles in the platform pitch and surge motion time series and somewhat higher frequency energy in the tower and blade bending moment process time series.

3.5 Summary

Extreme loads resulting from the coupled hydrodynamic and aeroelastic response of the selected spar buoy-supported offshore wind turbine were studied in time-domain stochastic simulations. Platform motions as well as tower and blade loads extremes were studied. It was found that the response and loads experienced by this offshore floating wind turbine were influenced to a great degree by input wind conditions associated with wind speeds close to and above the rated wind speed of the turbine. Due to the mean wind speed on the rotor, there is significant mean surge motion of the spar buoy platform supporting the floating offshore wind turbine. Platform surge motion was seen to exhibit greater variability compared to tower and blade loads. Fifteen ten-minute response simulations for eighteen different sea states were analyzed to help identify critical environmental conditions that could potentially cause large loads. Extreme tower loads were found to be higher for ten-minute hub-height longitudinal wind speeds between 11.89 m/s and 21.69 m/s with the accompanying highest possible wave height for that wind speed; extreme blade loads were found to be higher near a hub-height wind speed of 14.69 m/s; extreme platform surge motions were found to be higher for a hub-height wind speed of 11.89 m/s, closer to the rated wind speed for the turbine. Long-term load distributions and estimation of characteristic loads associated with return periods on the order of 50 years need to focus on wind conditions near these noted mean wind speeds and on associated wave conditions.

Chapter 4: Long-Term Loads for a Spar Buoy-Supported Floating Offshore Wind Turbine

4.1 Introduction

In Chapter 3, we saw that loads and platform motions for the 5 MW spar buoy-supported floating offshore wind turbine vary as wind speed and wave height vary. From a limited number of simulations, we identified a few critical sea states (or environmental conditions) that brought about larger levels of response. In design, one is interested in making sure that sufficient resistance (or capacity) is available to withstand all such loads. Indeed, IEC 61400-3 (International Electrotechnical Commission, 2009) defines an important design load case (DLC) which requires a comprehensive probabilistic analysis of turbine response so as to be able to derive a nominal load, L_{nom} , that is associated with a return period of 50 years. This load, L_{nom} , is used in DLC 1.1 with a load factor of 1.25 and then compared against a factored resistance in a conventional Load-and-Resistance-Factor-Design checking equation. It is important that the computation for L_{nom} is both accurate as well as efficient. For offshore wind turbines such as our spar-supported 5 MW turbine, derivation of L_{nom} requires understanding the environment—namely, the joint probability distribution of the important environmental parameters such as the hub-height ten-minute mean wind speed, V , and the significant wave height, H_s (in general, other environmental parameters such as the wave period may also be represented probabilistically). In addition, derivation of L_{nom} requires that one assess the variability of turbine response (loads and platform motions) for various combinations of environmental parameters—for instance, in our case, we are interested in carrying out a sufficient number of time-domain stochastic simulations of the offshore turbine from which we derive short-term probability distributions of any response measure, L , conditional on environmental parameters. Finally, what is required is that one estimate L_{nom} which will be that level of response whose mean frequency of exceedance is one in 50 years. Effectively, L_{nom} , the desired nominal response (or load) is the same as l_{50} , the 50-year response. In the following, we are interested in deriving l_{50} corresponding to different response measures, L , including (i) the fore-aft tower base bending moment; (ii) the out-of-plane blade root bending moment; and (iii) platform surge motion.

Since we will perform simulations of ten-minute duration, the random variable, L , is best described with that duration as reference. Accordingly, we define L as the ten-minute extreme (or the single largest peak or “global” maximum) from a single simulation. Other definitions may be employed such as the use of (i) all occurring peaks or “local” maxima in each response time series; (ii) peaks above a defined threshold response level; or (iii) “block” maxima representing largest response values occurring in smaller non-overlapping segments of shorter duration shorter than ten minutes. Regardless of how the

random variable, L , is defined, the desired response, l_{50} , must be the response with a 50-year return period. The probability of exceeding l_{50} in 10 minutes is a very small number if l_{50} is to be the 50-year response. Indeed, assuming independence of ten-minute extremes, we must have the following:

$$P(L > l_{50}) = \frac{1}{50 * 365.25 * 24 * 6} = 3.8 \times 10^{-7} \quad (4.1)$$

Equation (4.1) serves to define l_{50} , the desired response, but what is required is the distribution of the random variable representing the ten-minute extreme response, L . The real difficulty in such problems lies in obtaining this distribution—given that L depends on the environmental conditions; one generally establishes the probability distribution for L by applying the total probability theorem as follows:

$$P(L > l) = \iint_{all(V, H_s)} P(L > l | V, H_s) f_{V, H_s}(v, h) dv dh \quad (4.2)$$

In Equation (4.2), the joint probability density function, $f_{V, H_s}(v, h)$, needs to be established using information about the environment while $P(L > l | V, H_s)$, the complementary cumulative distribution of the response, L , given V and H_s , needs to be established from multiple simulations for each environmental parameter set, (V, H_s) . Equation (4.2) implies that simulations are needed for all possible (V, H_s) pairs and that a sufficient number of such simulations are run to ensure accurate estimation of $P(L > l | V, H_s)$. This is a computationally intensive exercise. Hence, an alternative procedure may be adopted that relies on structural reliability principles.

It is possible to restate our problem involving the three random variables, V , H_s , and L , if we define a limit state function, $g(V, H_s, L; l_{50})$ as follows:

$$g(V, H_s, L; l_{50}) = l_{50} - L = l_{50} - L(V, H_s) \quad (4.3)$$

The classical reliability “analysis” problem is where one evaluates the probability that the limit state function, $g(\cdot)$, is less than zero; then, $P(g(\cdot) < 0)$ is the probability of “failure.” Here, however, we note that the probability of failure is known—it is the target probability of response exceedance (synonymous with “failure”); it is l_{50} that we are interested in. Estimation of l_{50} is the reliability “design” problem. This could, of course, be solved using the tried and tested “forward” reliability analysis approach by assuming different values of l_{50} and then adjusting them until analysis shows that $P(g(\cdot) < 0)$ matches the target value. Alternatively, one can define the “inverse” reliability problem which directly

gets at estimation of l_{50} by searching a subset of the 3-D space of the random variables, (V, H_s, L) , that is consistent in a reliability sense with the target probability. We note that the target probability of failure, $P(g(\cdot) < 0)$, with $g(\cdot)$ defined in Equation (4.3) is 3.8×10^{-7} according to Equation (4.1).

In the Inverse First Order Reliability Method (Inverse FORM), one maps the physical random variables—here, V , H_s , and L —to standard normal random variables, U_1 , U_2 , and U_3 . The target probability of “failure” is the target probability of exceedance of the unknown l_{50} here. In Inverse FORM (Winterstein et al, 2003; Saranyasontorn, 2006), a target reliability index, β , is defined such that $\Phi(-\beta)$ matches that probability, where $\Phi(\cdot)$ is the cumulative distribution function for a standard normal random variable. Here, for our 50-year response, β is equal to 4.95. In Inverse FORM, one is required to evaluate all combinations of (U_1, U_2, U_3) values that lie on a sphere of radius β as follows:

$$u_1^2 + u_2^2 + u_3^2 = \beta^2 \quad (4.4)$$

The mapping of the independent standard normal random variables to the jointly distributed physical random variables is often carried out sequentially in terms of an equi-probable transformation of cumulative probabilities or exceedance fractiles, p_1, p_2, p_3 , as follows:

$$1 - p_1 = \Phi(u_1) = F_V(v) \quad (4.5)$$

$$1 - p_2 = \Phi(u_2) = F_{H_s|V}(h_s|v) \quad (4.6)$$

$$1 - p_3 = \Phi(u_3) = F_{L|V,H_s}(l|v, h) = 1 - G_{L|V,H_s}(l|v, h) \quad (4.7)$$

where $F_V(v)$ and $F_{H_s|V}(h|v)$ are cumulative distribution functions for V and for H_s given V . These are established from environmental data at the site of interest. Also, $F_{L|V,H_s}(l|v, h)$ and $G_{L|V,H_s}(l|v, h)$ are cumulative and complementary cumulative distribution functions, respectively, of the response variable, L , given V and H_s . These latter distributions are not known *a priori* but need to be established from multiple time-domain simulations for each (V, H_s) pair.

Depending on one’s point of view, Inverse FORM requires evaluation of (u_1, u_2, u_3) triads, (p_1, p_2, p_3) triads, or (V, H_s, L) triads that satisfy Equation (4.4). Consistent with the shortest distance to the failure surface in the reliability “analysis” problem that is related to the reliability index and, hence, to the probability of failure, in the reliability “design” or Inverse FORM problem, one searches all valid triads of physical or standard normal random variables or fractiles of them that satisfy Equation (4.4) and the

desired response, l_{50} , that matches the target probability of “failure” is that value of L at its appropriate p_3 fractile (per Equation (4.7)) that is larger than that resulting from any other triad combination that satisfies Equation (4.4). Equations (4.5) to (4.7) imply that candidate l_{50} values could result from rare harsh environmental conditions (i.e., small values of p_1 and p_2) in combination with commonly occurring response values as well as common environmental conditions in combination with rare large load values (i.e., small values of p_3).

Note that if $p_3 = 0.5$, then $u_3 = 0$, and what results with Inverse FORM is a search over a 2-D circle in the U_1 - U_2 space for the largest value of the *median* response of L given V and H_s . This is referred to as the “environmental contour” method. In general, this method will yield non-conservative estimates of quantities such as 50-year return period response values, l_{50} , because variability in the response given the environment is not fully accounted for. Such an approach assumes that physical quantities for design should be determined by searching over only the more demanding environmental conditions and performing a few response simulations for those conditions merely to establish what levels of response occur on average—neither are rare large response levels evaluated for these demanding conditions nor are any environmental conditions evaluated that might occur more often or might have associated response that is highly variable. The use of 3-D Inverse FORM attempts to remedy this shortcoming. As such, in our present study, different (V, H_s) pairs are considered and associate response fractiles, p_3 , for each case are compared before l_{50} is established.

4.2 Probabilistic Distributions for the Environmental Random Variables

For the site selected in this study (and discussed in Chapter 3), the hub-height wind speed, V , and the significant wave height, H_s , are represented probabilistically by establishing first the marginal distribution for V and then the conditional distribution for H_s given V . Because we are only interested in the operating range of wind speed (i.e., from the cut-in wind speed, v_{in} , equal to 3 m/s to the cut-out wind speed, v_{out} , equal to 25 m/s), we employ a truncated Weibull distribution for V . Thus, we have:

$$F_V(v) = \frac{G(v_{in}) - G(v)}{G(v_{in}) - G(v_{out})} \quad (4.8)$$

where, $G(v) = \exp\left(-\left(\frac{v}{s}\right)^k\right)$, $k = 2.19$, $s = 13.56$ m/s, $v_{in} = 3$ m/s, $v_{out} = 25$ m/s. Because the data available from the site were aggregated in the form of histogram bin counts and the raw data were unavailable, the distribution shape and scale parameters, k and s , are estimated using the method of moments.

The wave height data conditional on wind speed were also available only in the form of histogram bin counts; hence, the method of moments is again employed to estimate shape and scale parameters for a Weibull distribution of H_s given V . Thus, we have:

$$F_{H_s|V}(h|v) = 1 - \exp\left(-\left(\frac{h}{s(v)}\right)^{k(v)}\right), \quad k(v) > 0 \quad (4.9)$$

where the Weibull scale and shape parameters are functions of the wind speed—thus, we have $k(v) = 0.037v^{1.43} + 1.52$ and $s(v) = 0.010v^{1.90} + 1.65$.

In the turbine response simulations, the sea surface elevation process is simulated and the JONSWAP spectrum needed there is a function of the significant wave height, H_s , and the spectral peak period, T_p . In this study, we use the expected value of T_p given H_s and V ; thus, in the simulations, each short-term ten-minute simulation has as environmental inputs, values for V , H_s , and $E[T_p|H_s, V]$. The conditional expected value, $E[T_p|H_s, V]$, is estimated from the site data.

4.3 Short-Term Response Extremes

For 2-D Inverse FORM, one can construct an environmental contour where $u_3 = 0$ and $u_1^2 + u_2^2 = \beta^2$ where $\beta = 4.95$. Equations (4.5), (4.6), (4.8), and (4.9) may then be used to represent this environmental contour in the space of the physical random variables, V and H_s , as is done in Figure 4.1. In 3-D Inverse FORM, other candidate V and H_s values need also to be evaluated that are associated with points within the 2-D contour where $u_1^2 + u_2^2 < \beta^2$ and $u_3 > 0$. The dots within the 2-D environmental contour in Figure 4.1 represent such sea states that need to be evaluated in 3-D Inverse FORM. A total of 116 sea states are identified by dots reflecting a gridded pattern at a wind speed interval of 1.4 m/s and a significant wave height interval of 1.0 m. For all of these 116 sea states, appropriate exceedance fractiles, p_3 , of the response variable, L , need be evaluated. The p_3 fractiles for L at all (V, H_s) pairs on the 2-D contour as well as at the 116 points identified are estimated; the largest of these is the desired 50-year load, l_{50} . For a specified choice (v, h) of the random variables (V, H_s) , p_3 may be expressed as follows:

$$p_3 = 1 - \Phi\left(\sqrt{\beta^2 - [\Phi^{-1}(F_V(v))]^2 - [\Phi^{-1}(F_{H_s|V}(h|v))]^2}\right) \quad (4.10)$$

Figure 4.2 shows the response exceedance fractiles, p_3 , for all of the candidate sea states that are evaluated in the 3-D Inverse FORM. Also shown in the figure are contours of constant values of these same fractiles. It is evident from this figure that to evaluate some sea states, the response at very small

values of exceedance, p_3 , needs to be estimated. To achieve accurate estimates of response at such rare probability levels requires extrapolation of short-term simulation ten-minute extremes data from a limited number of simulations. While all the 116 candidate sea states should be analyzed and the maximum p_3 -response fractile of these is the 50-year load of interest, it is instructive to study response characteristics of the study turbine system for various (V, H_s) pairs to help focus simulation resources where there is great potential for large response levels. Alternatively, it may become obvious that some (V, H_s) pairs are unlikely to lead to large response levels even for very small response exceedance fractiles; limited simulation effort may be warranted for those sea states. If, for any (V, H_s) pair, either response levels are found to be large even when only a small number of simulations are run or the variability in the response (e.g., in ten-minute extreme values) is great, there is possibility that at the desired extrapolated p_3 fractile level, response levels may be important and could potentially yield the design level, l_{50} .

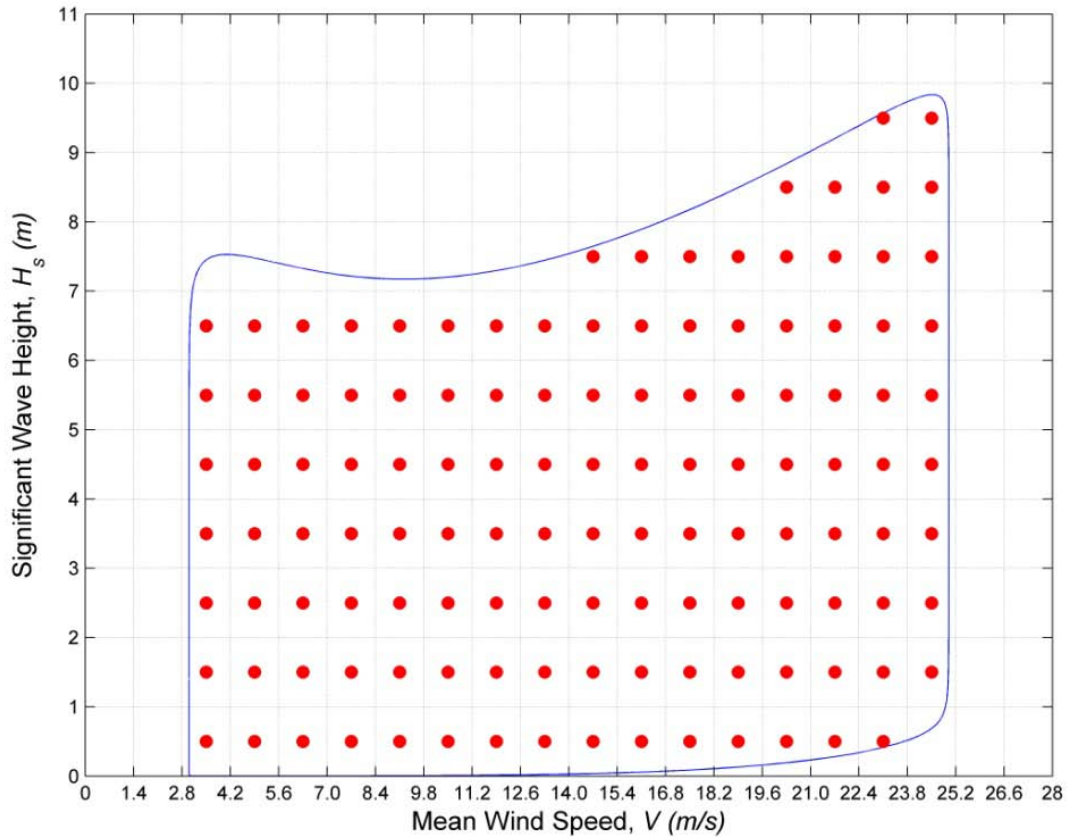


Figure 4.1: Sea states selected for the turbine response stochastic simulations indicated by dots shown along with the 2-D environmental contour for a 50-year return period.

For all the 116 candidate sea states identified in Figure 4.1, 25 ten-minute simulations are carried out and ten-minute extremes of the fore-aft tower base bending moment, the out-of-plane blade root

bending moment, and the platform surge motion are found. Based on these response extremes, median response surfaces are constructed; these are presented in Figures 4.3 (a), (b), and (c). It is clear that the turbine's pitch control system tends to cause larger loads around the rated wind speed of 11.4 seconds and that all the response quantities see lower extremes at wind speeds both below and above the rated wind speed. An exception is the tower base bending moment which does experience larger values for some higher wind speeds although this could be explained by the accompanying larger wave heights with those high wind speeds. In general, variation of response extremes with wave height does not show an obvious trend except in the case of the tower base bending moment whose extreme values clearly increase with increasing significant wave height. The median response surfaces suggest that wind speeds around and higher than the rated wind speed with accompanying wave heights bring about large levels of response. At lower exceedance fractiles, it is expected that this trend will continue and the candidate sea states for these identified wind speed and wave height ranges will likely produce the 50-year response, l_{50} .

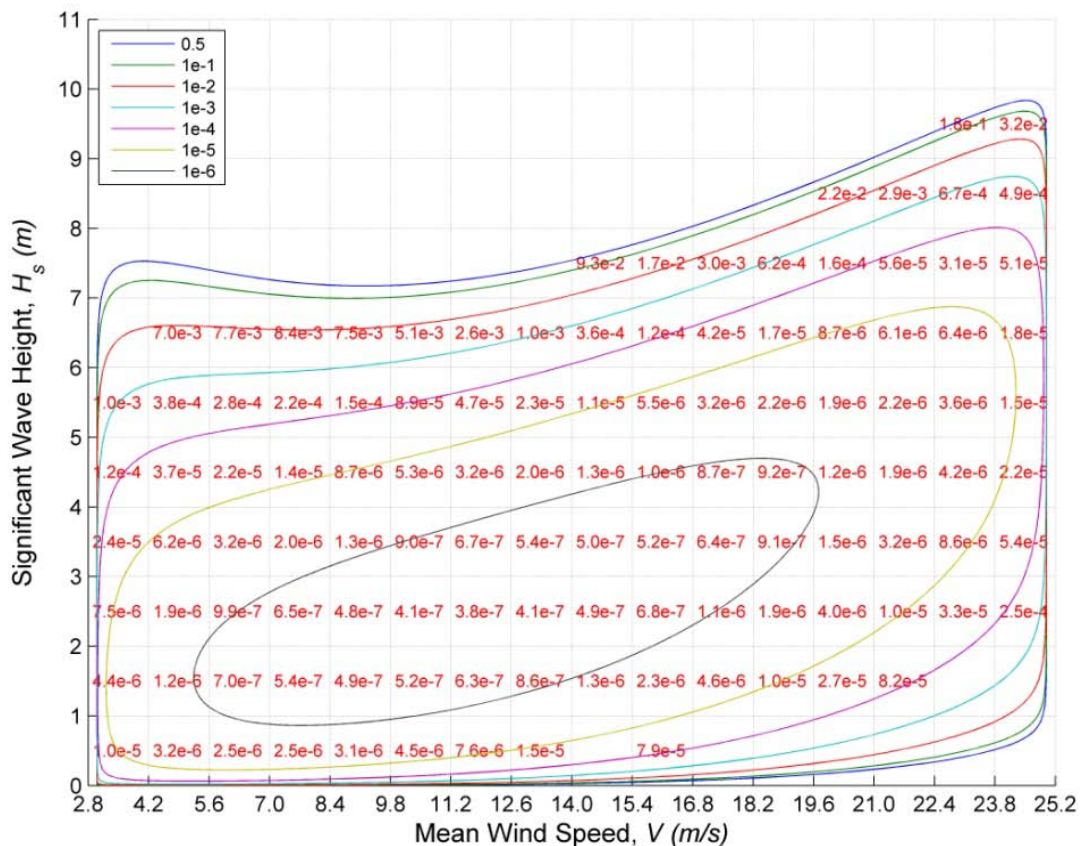


Figure 4.2: Response exceedance fractiles, p_3 , for candidate sea state evaluated. Also shown in order moving inwards are contours of 0.5, 1e-1, 1e-2, 1e-3, 1e-4, 1e-5, and 1e-6 exceedance fractiles.

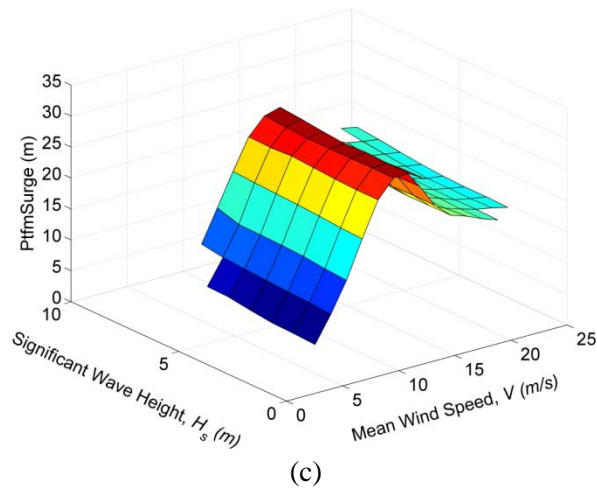
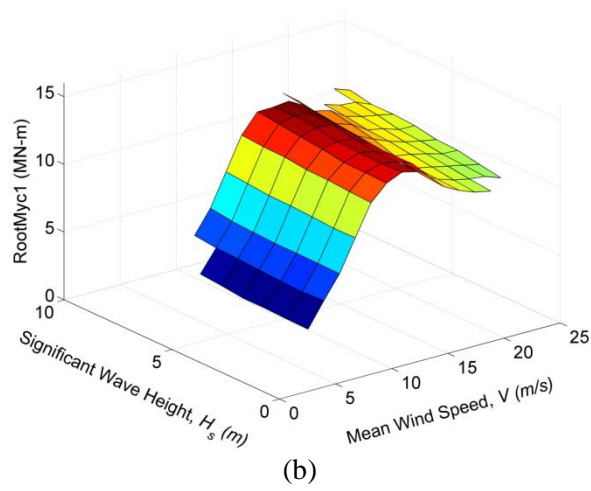
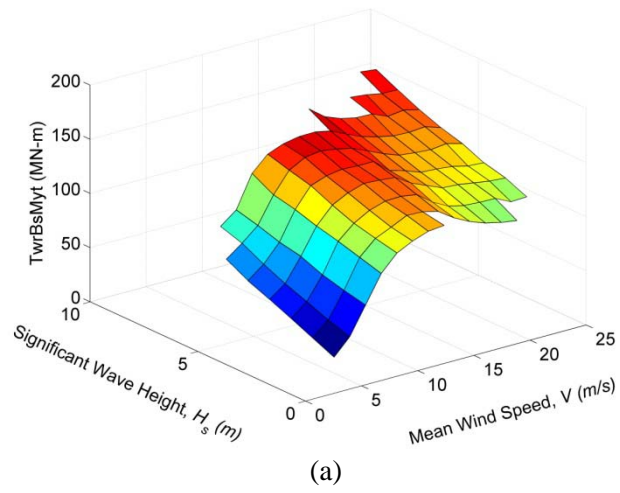
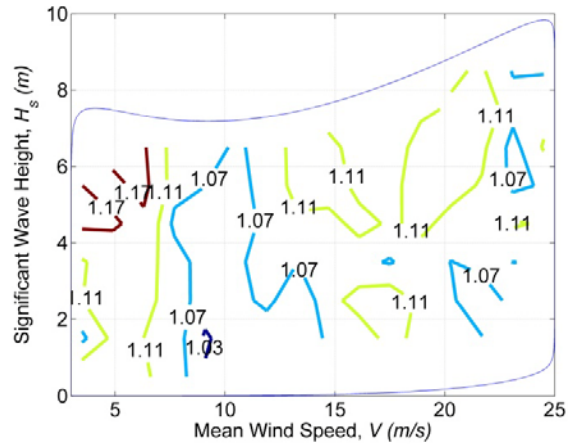


Figure 4.3: Median ten-minute extreme response surfaces based on 25 simulations for: (a) fore-aft tower base bending moment; (b) out-of-plane blade root bending moment; and (c) platform surge.

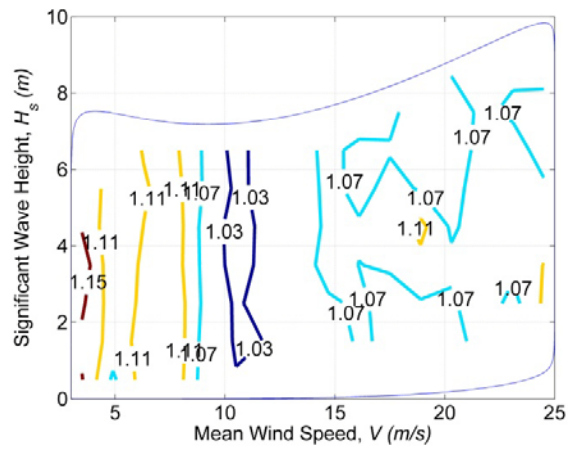
While a study of the median extreme response helps in identifying potentially interesting sea states for 3-D Inverse FORM by virtue of the larger levels of response seen for some (V, H_s) pairs, another consideration in deriving rarer response exceedance fractiles, p_3 , relates to the extent of variability seen in a limited number of simulated extremes. Greater variation among the simulated ten-minute extremes for some (V, H_s) pairs might suggest that the distribution tails (where the p_3 response fractiles will need to be obtained after extrapolation) might be more variable for them and larger response levels might then become more likely for those sea states. Figures 4.4 (a), (b), and (c) summarize contour plots of the ratio of the 84th percentile non-exceedance response extreme to the median response extreme based on 25 ten-minute simulations—the figures are for fore-aft tower base bending moment, out-of-plane blade root bending moment, and platform surge, respectively. These ratio contours are shown together with the 50-year return period environmental contour. Ratios close to unity imply low variability in response ten-minute extremes; the larger the ratio, the more variable is the response extreme. From the figures, it is noted that the fore-aft tower base bending moment is most variable at low wind speeds but these conditions are likely not important since we saw in Figure 4.3 (a) that response extremes are low there. Tower bending moments above rated winds also show some variability; since the median extreme response there is also large. Sea states with wind speeds at and above rated wind with accompanying wave heights are likely to be important in the 3-D Inverse FORM study. The out-of-plane blade root bending moment is seen to be less variable than the tower bending moment and, among the different (V, H_s) pairs, it is found that around rated winds where the median response extremes were largest, variability in response extremes is actually quite low. Surge motions are seen to be the most variable of the three response measures studied here. Particularly, for wind speeds around 16 m/s, extreme surge motion variability is great. This suggests the possibility of interesting sea states in that region of above-rated winds with accompanying waves.

4.4 Statistical Extrapolation of Response

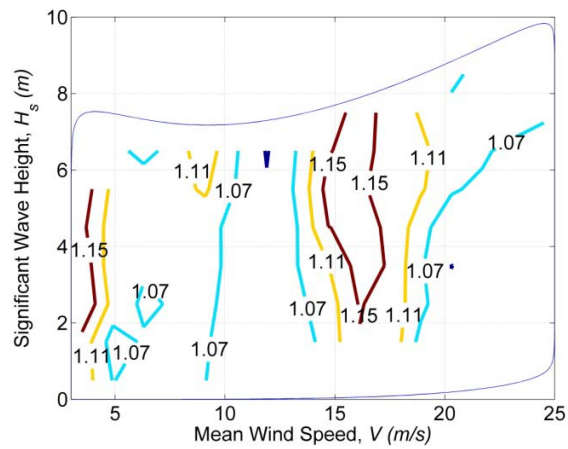
We now address the issue of extrapolation of response extremes to desired exceedance fractiles, p_3 , defined by Equation (4.10). We saw from Figure 4.2 that these desired sea state-dependent fractiles can be extremely small. From a limited number of simulations, extrapolation from collected extremes data to the fractile level of interest is unavoidable. Accordingly, we discuss here the procedure employed for this extrapolation. We carry out N ten-minute simulations and rank-order the available N extremes of each response type. Then, for each sea state, (v, h) , we estimate Weibull distribution parameters for $F_{L|V,H_s}(l|v, h)$ (see Equation (4.7)) using the largest 50% of all the extremes since we are interested in the tails of the distributions. After the distribution parameters have been estimated, the response level corresponding to the exceedance fractile, p_3 , is computed as l_{p_3} where p_3 is given by Equation (4.10).



(a)



(b)



(c)

Figure 4.4: Contours of the ratio of the 84th percentile non-exceedance response extreme to the median response extreme based on 25 simulations for: (a) fore-aft tower base bending moment; (b) out-of-plane blade root bending moment; and (c) platform surge. Also shown is the 50-year return period environmental contour.

Table 4.1: Extrapolated response (l_{p3}), largest simulated extreme (SimMax), and median extreme response ($l_{0.5}$) based on N simulations for a few critical sea states.

(a) Fore-aft tower base bending moment

V (m/s)	H_s (m)	N	l_{p3} (MN-m)	SimMax (MN-m)	$l_{0.5}$ (MN-m)
13.3	6.5	25	200.4	180.9	151.6
	5.5	25	201.1	175.9	144.9
	4.5	30	195.9	172.3	139.0
14.7	5.5	70	195.7	171.1	138.8
	4.5	65	190.5	166.5	133.7
20.3	7.5	25	195.9	175.4	139.3
21.7	8.5	25	198.1	188.9	144.0
	7.5	25	202.4	177.1	133.1
23.1	8.5	25	193.6	179.7	141.1
	7.5	25	199.8	175.2	134.9

(b) Out-of-plane blade root bending moment

V (m/s)	H_s (m)	N	l_{p3} (MN-m)	SimMax (MN-m)	$l_{0.5}$ (MN-m)
14.7	6.5	25	16.7	15.5	13.6
	5.5	25	16.9	15.2	13.4
	4.5	25	16.9	14.9	13.2
16.1	6.5	25	17.0	15.0	12.6
	5.5	55	17.0	14.9	12.5
	4.5	65	16.5	14.4	12.2

(c) Platform surge motion

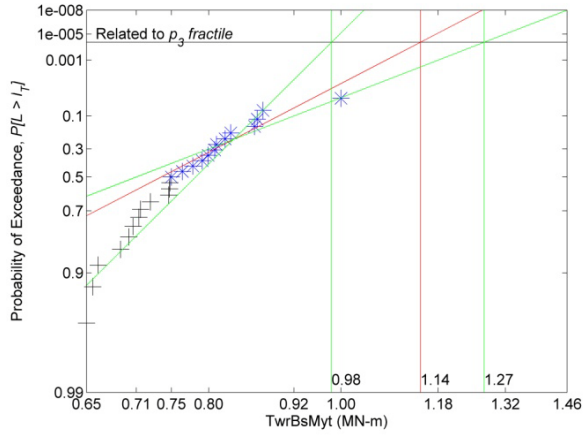
V (m/s)	H_s (m)	N	l_{p3} (m)	SimMax (m)	$l_{0.5}$ (m)
9.1	5.5	25	37.2	33.6	27.7
	4.5	25	37.1	32.9	27.9
13.3	6.5	25	37.7	33.7	28.7
	5.5	30	38.3	33.6	28.2
	4.5	30	38.2	33.4	28.0
	3.5	25	38.0	33.3	28.2
	2.5	25	37.1	33.0	28.2
14.7	5.5	60	34.6	30.3	25.2

To avoid excessive extrapolation of response to levels far beyond values actually simulated, we impose a restriction that the extrapolated load, l_{p3} , for any sea state may not exceed the largest simulated extreme response from N simulations by greater than 25%. Accordingly, we begin by carrying out 25 simulations (i.e., choosing $N = 25$); we estimate l_{p3} and compare l_{p3} with SimMax, the largest simulated

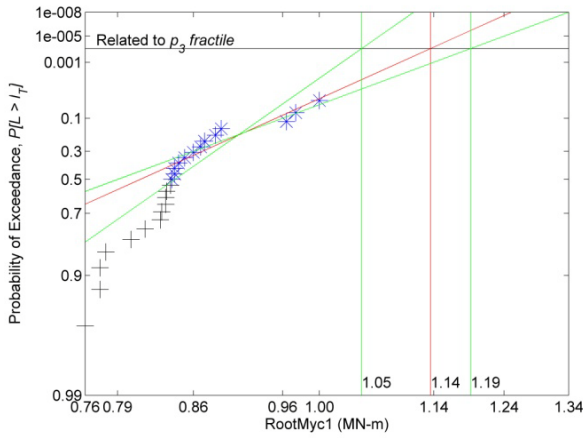
response from the N simulations. If l_{p3}/SimMax is greater than 1.25, we assume that the amount of extrapolation is unreasonably large and unjustified; we then increase the number of simulations by 5. This is repeated until l_{p3}/SimMax falls below 1.25. After all the sea states are evaluated in this manner, the various l_{p3} values can then be checked and the largest chosen as the design response, l_{50} . Table 4.1 summarizes l_{p3} , SimMax, and median extreme response ($l_{0.5}$) values for the fore-aft tower base bending moment, the out-of-plane blade bending moment, and the surge motion for several of the more critical sea states. As can be seen from the table, sometimes the number, N , of simulations required to ensure that extrapolated l_{p3} is not greater than SimMax by more than 25% needed to be increased considerably from the original 25 simulations. After this exercise was completed, the largest l_{p3} values were selected as the 50-year response values, l_{50} . Table 4.2 summarizes the l_{50} values together with the accompanying sea state parameters, V and H_s . The important sea state conditions that are associated with these rare 50-year response values appear in the areas thought to be of interest based on our interpretation of results summarized in Figures 4.3 and 4.4. To ensure that the l_{p3} values for the various sea states are reliable, it is worth computing confidence intervals on predicted l_{p3} . This can be achieved by bootstrapping (see, for example, Fogle et al, 2008) the extreme response data. The 90%-confidence interval normalized by the l_{50} value for each state was computed. The width of this normalized interval should generally be small if the predicted l_{p3} values are to be considered accurate estimates. Figure 4.5 summarizes predicted l_{p3} values obtained by Weibull distribution fits to the largest 50% of the simulated response extremes for three separate critical sea states for each of the three response measures studied. By bootstrapping the response extremes data, 90%-confidence intervals on estimates of l_{p3} were also computed and are summarized in Figure 4.5. With the exception of the fore-aft tower base bending moment, the other response parameters produce l_{50} values with reasonably small normalized confidence intervals.

Table 4.2: Estimated 50-year response values for (a) fore-aft tower base bending moment, (b) out-of-plane blade root bending moment, and (c) platform surge motion using 3-D Inverse FORM.

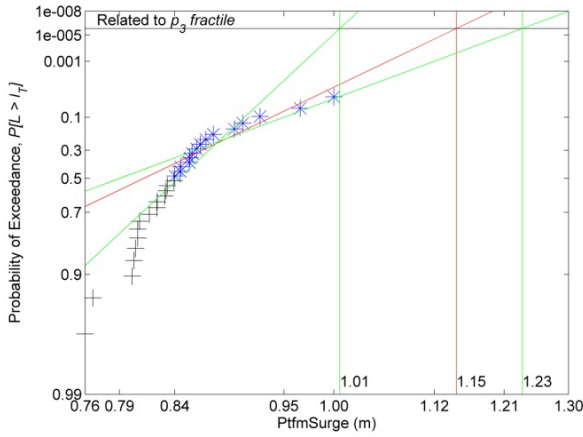
Response	V (m/s)	H_s (m)	l_{50}
Fore-aft tower base bending moment	21.7	7.5	202.4 MN-m
Out-of-plane blade root bending moment	16.1	6.5	17.0 MN-m
Platform surge motion	13.3	5.5	38.3 m



(a)



(b)



(c)

Figure 4.5: Two-parameter Weibull distribution fits to the largest 50% of simulated ten-minute response extremes in critical sea states for: (a) fore-aft tower base bending moment; (b) out-of-plane blade root bending moment; and (c) platform surge.

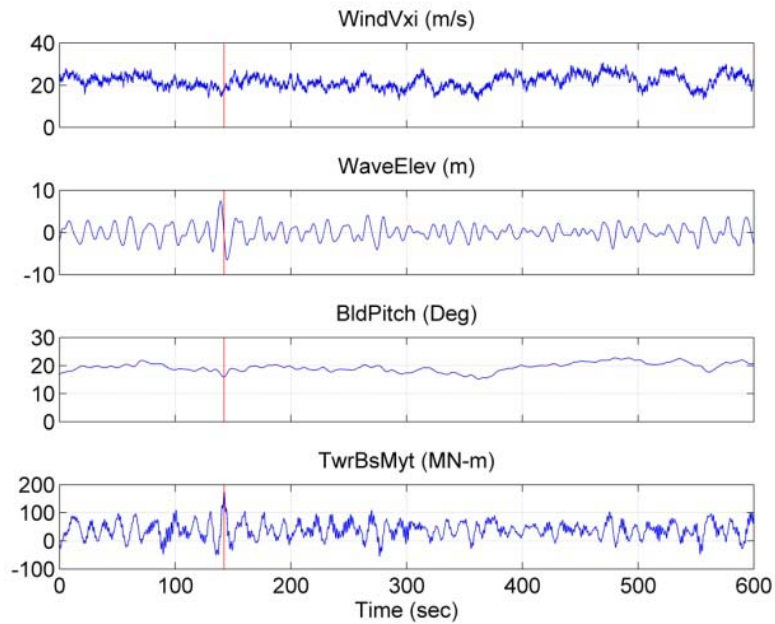


Figure 4.6: Time series for a single simulation showing hub-height longitudinal wind speed, sea surface elevation, blade pitch, and fore-aft tower base bending moment for the sea state with $V = 21.7$ m/s and $H_s = 7.5$ m and where the largest fore-aft tower base bending moment (177.1 MN-m) was found.

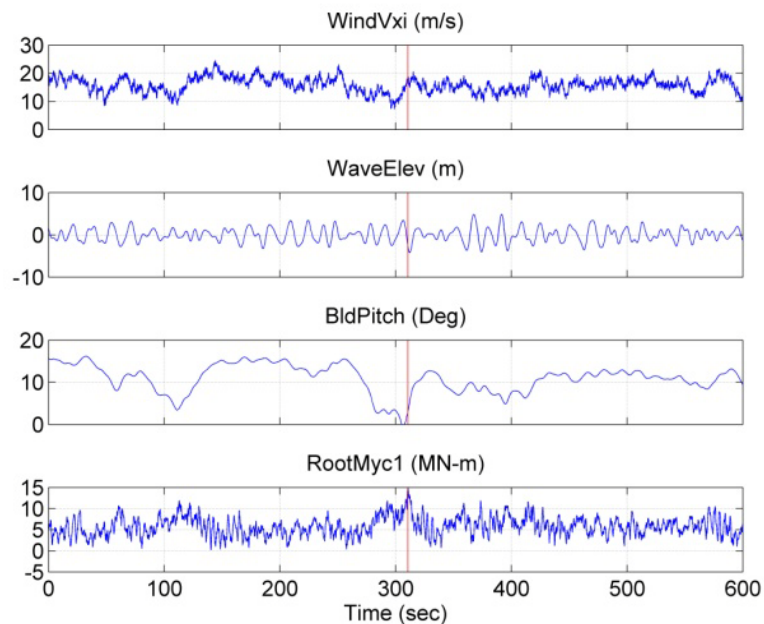


Figure 4.7: Time series for a single simulation showing hub-height longitudinal wind speed, sea surface elevation, blade pitch, and out-of-plane blade root bending moment for the sea state with $V = 16.1$ m/s and $H_s = 6.5$ m and where the largest out-of-plane blade root bending moment (15.0 MN-m) was found.

In Table 4.2, the critical sea states for each response type that yield the 50-year response are identified. For the surge motion, the 50-year surge offset displacement of the platform is 38.3 meters. It should be noted that for the sea state where this is expected to occur (a maximum offset of 33.6 meters was recorded in the simulations performed), the mean offset due to the non-zero wind forces alone is around 18 meters; this suggests that the 50-year surge response is roughly 20 meters displaced from the mean platform position in surge. It is useful to study the two load measures—fore-aft tower base bending moment and out-of-plane blade root bending moment—by examining time series where the largest simulated values of these loads were recorded in critical sea states (identified in Table 4.2) that are used to arrive at 50-year values for these loads. Figure 4.6 shows a single ten-minute time series where the largest fore-aft tower base bending moment of 177.1 MN-m occurred. This was for the sea state with $V = 21.7$ m/s and $H_s = 7.5$ m. Shown in the figure are the time series for hub-height longitudinal wind speed, sea surface elevation, blade pitch, and fore-aft tower base bending moment. It may be noted that the largest tower bending moment occurs around 140 seconds into the record and is preceded by a very large wave. Note that a very slight pitching back of the blades is also evident around the time of the largest load; however, the large wave is most likely the primary driver of the large tower bending moment. Figure 4.7 shows a single ten-minute time series where the largest out-of-plane blade root bending moment of 15.0 MN-m occurred. This was for the sea state with $V = 16.1$ m/s and $H_s = 6.5$ m. Shown in the figure are the time series for hub-height longitudinal wind speed, sea surface elevation, blade pitch, and out-of-plane blade root bending moment. It may be noted that the largest out-of-plane blade root bending moment occurs around 310 seconds into the record and is preceded by a control action that brings about a zero blade pitch angle. There is moderate-sized wave preceding the largest load but the primary driver of the large blade bending moment is most likely the action of the blades pitching back to zero degrees that increased the aerodynamic loading and, hence, the bending moment at the blade root.

4.5 Summary

In this chapter, we focused on the prediction of 50-year response values for the selected 5 MW spar buoy-supported floating offshore wind turbine. For the selected site, the environmental conditions describing wind speed and wave height statistics were employed together with time-domain simulations of the turbine response for a range of sea states identified as part of the 3-D Inverse First-Order Reliability Method. By carrying out multiple simulations, fractiles of the response (consistent with the desired return period of 50 years) were estimated for the sea states. Then, 50-year response levels of tower loads, blade loads, and platform surge motion were estimated and associated critical sea states were identified. Using bootstrapping, we evaluated the accuracy of the derived 50-year response values. By studying time series, some conclusions were made regarding the drivers of the large tower and blade loads.

Chapter 5: Conclusions

5.1 Overview of the Research Study

To date, offshore wind turbines have been confined to shallow waters closer to the shore. Sites farther offshore provide better wind resources—i.e., the winds are both stronger as well as less turbulent; however, the deeper waters encountered at such sites make bottom-supported turbines less economical. Wind turbines mounted atop floating platforms are, thus, being considered for such deeper water offshore sites. Of various alternative floating wind turbine concepts, the spar buoy platform with a deep draft structure and a low center of gravity below the center of buoyancy uses ballasting to achieve stability. The reliability analysis of a spar buoy-supported floating offshore 5MW wind turbine based on stochastic simulation is the subject of this study. Environmental data from a selected deepwater reference site were employed in the numerical studies. Using time-domain simulations, the dynamic behavior of the coupled platform-turbine system was studied; statistics of tower and rotor loads as well as platform motions were estimated and critical combinations of wind speed and wave height identified. Long-term loads associated with a 50-year return period were estimated using statistical extrapolation based on loads derived from the simulations and with the help of different alternative inverse reliability procedures.

5.2 Conclusions

We analyzed the extreme loads for a 5 MW spar buoy supported offshore wind turbine over the entire range of operating wind speeds from cut-in to cut-out and for a range of associated significant wave heights. The study focused on understanding statistics and probability distributions for the fore-aft tower base bending moment, out-of-plane blade root bending moment, and platform surge motion. Based on our study, we drew the following conclusions:

- The platform mean motions and blade loads experienced by the spar buoy-supported offshore floating wind turbine were influenced to a greater degree by input wind conditions close to and above the turbine's rated wind speed than by other conditions.
- Due to the mean wind speed on the rotor, there is significant mean surge motion of the spar buoy platform supporting the floating offshore wind turbine.
- Platform surge motion was found to exhibit greater variability compared to the tower and blade loads.
- Extreme tower loads were found to be higher for ten-minute hub-height longitudinal wind speeds between 11.89 m/s and 21.69 m/s with the accompanying highest possible wave height for that wind speed; extreme blade loads were found to be higher near a hub-height wind speed of 14.69 m/s; extreme platform surge motions were found to be higher for a hub-height wind speed of 11.89 m/s, closer to the rated wind speed of the turbine.

We also analyzed long-term loads for the spar-supported wind turbine using inverse reliability procedures. The following conclusions were drawn:

- The median fractile of the ten-minute extreme fore-aft tower base bending moment (TwrBsMyt) was found to be highest for wind speeds between the rated wind speed and cut-out wind speed and for close to the highest associated significant wave height.
- The median fractile of the ten-minute out-of-plane blade root bending moment (RootMyc1) and of the platform surge motion (PtfmSurge) were highest for wind speeds above the rated wind speed and for close to the highest associated significant wave height.
- Contours of the ratio of the 84th percentile ten-minute extreme to the median ten-minute extreme for various response variables showed that tower load variability (in the region of large loads) was high for wind speeds above the rated wind speed and for all associated wave heights; extremes of out-of-plane blade root bending moment and platform surge motion showed higher variability for wind speeds around the rated wind speed.
- The variability in platform motion extremes was found to be almost independent of wave height.
- The long-term fore-aft tower base bending moment was found to be largest for a mean wind speed of 21.7 m/s with an associated significant wave height of 7.5 m. This sea state had high wave energy and was associated with significant variability in the load distribution tail.
- The long-term out-of-plane blade root bending moment was found to be largest for a mean wind speed of 16.1 m/s with an associated significant wave height of 6.5 m. For this sea state, the distribution tail for this blade load was highly variable.
- Long-term platform surge motions were found to be largest for a mean wind speed of 13.3 m/s (close to the rated wind speed) and for an associated significant wave height of 5.5 m.
- The long-term loads were generally not the largest for the rarest sea state (i.e., those with the highest associated non-exceedance fractile). Short-term response variability and the likelihood of different environmental conditions act together so that the critical environmental conditions are generally found to be somewhat different than what is inferred from use of the 50-year environmental contour.

5.3 Concluding Comments and Suggestions for Future Research

The conclusions reached from this study are based on various assumptions regarding the modeling of the baseline wind turbine model, representation of the hydrodynamic loading on the support structure, etc. These conclusions need to be viewed in light of the many simplifying assumptions regarding structural models and loading. Also, we have considered only a single wind turbine model (i.e., the NREL offshore 5 MW baseline wind turbine); additional studies with different turbines and support

platforms would be necessary in order to generalize the conclusions made from this study.

Refinement in the definition of the identified critical sea states and the associated long-term loads may be done in a number of ways. By carrying out additional focused studies near the identified critical sea states using a large number of simulations for the different load types, we can improve estimates of long-term loads.

In this study, we only employed “global” maxima, i.e., ten-minute extremes to derive long-term loads. Alternative extreme statistics such as the use of block maxima, the use of process models, or the use of the peak-over-threshold method might be suggested as alternative approaches for deriving long-term loads as well as for validation of the results presented here.

References

1. Agarwal, P. and L. Manuel. "Simulation of Offshore Wind Turbine Response for Extreme Limit States." *Proceedings of the 26th International Conference on Offshore Mechanics and Arctic Engineering (OMAE)*. Paper No. OMAE-2007-29326, San Diego, California, 10-15 June 2007.
2. Agarwal, P. *Structural Reliability of Offshore Wind Turbines*. Ph. D. Dissertation. The University of Texas at Austin, 2008.
3. Det Norske Veritas, "Design of Offshore Wind Turbine Structures," Offshore Standard, DNV-OS-J101, 2007.
4. Fogle, J., P. Agarwal, and L. Manuel. "Towards an Improved Understanding of Statistical Extrapolation for Wind Turbine Extreme Loads." *Wind Energy*, Vol. 11, No. 6, pp. 613– 635, November/December 2008.
5. International Electrotechnical Commission, "Wind Turbines - Part 1: Design Requirements," IEC 61400-1 Ed. 3.0, 2005.
6. International Electrotechnical Commission, "Wind Turbines - Part 3: Safety Requirements for Offshore Wind Turbines," IEC 61400-3 Ed. 1.0, 2009.
7. Jonkman, J. M., and Buhl Jr., M. L., 2005. "FAST User's Guide," Tech. Rep. NREL/EL-500-38230, National Renewable Energy Laboratory, Golden, CO.
8. Jonkman, J. M. and Sclavounos, P. D., "Development of Fully Coupled Aeroelastic and Hydrodynamic Models for Offshore Wind Turbines," *44th AIAA Aerospace Sciences Meeting and Exhibit, 9–12 January 2006, Reno, NV, AIAA Meeting Papers on Disc* [CD-ROM], Reston, VA: American Institute of Aeronautics and Astronautics, January 2006, AIAA-2006-995, NREL/CP-500-39066, Golden, CO: National Renewable Energy Laboratory.
9. Jonkman, J. M. and Buhl, M. L., Jr., "Development and Verification of a Fully Coupled Simulator for Offshore Wind Turbines," *45th AIAA Aerospace Sciences Meeting and Exhibit, 8–11 January 2007, Reno, NV, AIAA Meeting Papers on Disc* [CD-ROM], Reston, VA: American Institute of Aeronautics and Astronautics, January 2007, AIAA-2007-212, NREL/CP-500- 40979, Golden, CO: National Renewable Energy Laboratory.
10. Jonkman, J. M. *Dynamics Modeling and Loads Analysis of an Offshore Floating Wind Turbine*. Ph.D. Dissertation, University of Colorado at Boulder, 2007.

11. Jonkman, B. J., and Buhl Jr., M. L., 2007. "TurbSim User's Guide," Tech. Rep. NREL/TP-500-41136, National Renewable Energy Laboratory, Golden, CO.
12. Jonkman, J. M., Butterfield, S., Musial, W., and Scott, G., 2009. Definition of a 5-MW Reference Wind Turbine for Offshore System Development. Tech. Rep. NREL/TP-500-38060, National Renewable Energy Laboratory, Golden, CO.
13. Jonkman J, Larsen T, Hansen A, Nygaard T, Maus K, Karimirad M, Gao Z, Moan T, Fylling I, Nichols J, Kohlmeier M, Pascual J V, Merino D, Shi W, and Park H, "Offshore Code Comparison Collaboration within IEA Wind Task 23: Phase IV Results Regarding Floating Wind Turbine Modeling," *To be presented at European Wind Energy Conference (EWEC) Warsaw, Poland April 20-23, 2010*; NREL/CP-500-47534, Golden, CO: National Renewable Energy Laboratory.
14. Lee, K. H., "Responses of Floating Wind Turbines to Wind and Wave Excitation," M.S. Thesis, Department of Ocean Engineering, Massachusetts Institute of Technology, Cambridge, MA, USA, January 2005.
15. Lee, C. H. and Newman, J. N., "WAMIT® User Manual, Versions 6.3, 6.3PC, 6.3S, 6.3SPC," Chestnut Hill, MA: WAMIT, Inc., 2006.
16. Matha D, *Model Development and Loads Analysis of an Offshore Wind Turbine on a Tension Leg Platform, with a Comparison to Other Floating Turbine Concepts*, M.S. Thesis, SWE, University of Stuttgart, Germany, 2009; NREL/TP-500-45891, Golden, CO: NREL.
17. Nielsen, F. G., Hanson, T. D., and Skaare, B., "Integrated Dynamic Analysis of Floating Offshore Wind Turbines," *Proceedings of OMAE2006 25th International Conference on Offshore Mechanics and Arctic Engineering, 4-9 June 2006, Hamburg, Germany* [CD-ROM], Houston, TX: The American Society of Mechanical Engineers (ASME International) Ocean, Offshore and Arctic Engineering (OOAE) Division, June 2006, OMAE2006-92291.
18. P. Ragan. *Estimation of Long-Term Structural Loads on a Wind Turbine*. M.S. Thesis, University of Texas at Austin, 2007.
19. Saranyasontorn, K. *A Simulation-Based Procedure for Reliability Analysis of Wind Turbines*. Ph.D. Dissertation. The University of Texas at Austin, 2006.
20. Skaare, B., Hanson, T. D., and Nielsen, F. G., "Importance of Control Strategies on Fatigue Life of

Floating Wind Turbines,” *Proceedings of OMAE2007 26th International Conference on Offshore Mechanics and Arctic Engineering, 10–15 June 2007, San Diego, CA* [CD-ROM], Houston, TX: The American Society of Mechanical Engineers (ASME International) Ocean, Offshore and Arctic Engineering (OOAE) Division, June 2007, OMAE2007-29277.

21. S. Butterfield, W. Musial, J. Jonkman, and Sclavounos, P., “Engineering Challenges for Floating Offshore Wind Turbines,” Conference Paper, NREL/CP-500-38776, National Renewable Energy Laboratory, Golden, CO, September 2007.
22. The European Wind Energy Association, “Oceans of Opportunity: Harnessing Europe’s Largest Domestic Energy Resource,” September 2009.
23. U.S. Department of Energy, “20% Wind Energy by 2030: Increasing Wind Energy’s Contribution to U.S. Electricity Supply,” July 2008.
24. Winterstein S. R., T. C. Ude, C. A. Cornell, P. Bjerager, and S. Haver. “Environmental Parameters for Extreme Response: Inverse FORM with Omission Factors.” *Proceedings of ICOSSAR ’93*. Innsbruck, Austria, 9-13 August 1993.
25. Withee, J. E., “Fully Coupled Dynamic Analysis of a Floating Wind Turbine System,” Ph.D. Dissertation, Department of Ocean Engineering, Massachusetts Institute of Technology, Cambridge, MA, USA, 2004.
26. Wayman, E. N.; Sclavounos, P. D.; Butterfield, S.; Jonkman, J.; and Musial, W., “Coupled Dynamic Modeling of Floating Wind Turbine Systems,” *2006 Offshore Technology Conference, 1–4 May 2006, Houston, TX* [CD-ROM], Richardson, TX: Offshore Technology Conference, May 2006, OTC 18287, NREL/CP-500-39481.

Vita

Abhinav Sultania was born in Siswa Bazar, District Maharajganj, U.P., India on 10 November 1985, the son of Mr. Satyanarain Kumar Sultania and Mrs. Prem Lata Sultania. He received the Bachelor of Technology degree in Civil Engineering from the Sardar Vallabhbhai National Institute of Technology in May, 2007. He worked as an executive officer for Bharat Petroleum Corporation Limited for a year before he applied to the University of Texas at Austin for enrollment in their Civil Engineering program. He was accepted and started graduate studies in the Department of Civil, Architectural and Environmental Engineering at the University of Texas at Austin in 2008.

Permanent Address: 8/148 IndiraNagar
 Lucknow, UttarPradesh 226016
 India

This thesis was typed by the author.